ENGINEERING ORDERED BICONTINUOUS NETWORKS FORMED BY BLOCK COPOLYMERS WITH ADDITIVES USING MOLECULAR MODELING

A Dissertation

Presented to the Faculty of the Graduate School

of Cornell University

in Partial Fulfillment of the Requirements for the Degree of

Doctor of Philosophy

by

Poornima Padmanabhan

February 2016

ENGINEERING ORDERED BICONTINUOUS NETWORKS FORMED BY BLOCK COPOLYMERS WITH ADDITIVES USING MOLECULAR MODELING

Poornima Padmanabhan, Ph.D.

Cornell University 2016

Unlike other simpler morphologies that AB diblock copolymers (DBCs) can form, ordered bicontinuous phases are made of two interweaving network structures of the minority phase A in a matrix of the majority phase B. These network structures are attractive for applications involving ordered nanoscale porous materials including solar cell active membranes, filters, catalysts, and nanolithographic templates. Key challenges in obtaining these structures successfully are: (i) the need for very precise chemistries due to their very limited region of stability in pure block copolymer melts, (ii) the limited tunability of the morphology feature size for specific applications, and (iii) their proclivity for defect formation. The use of additives could provide more handles to tailor feature size and to enhance the stability of bicontinuous phases (e.g., by alleviating the packing frustration of the short A-blocks which creates an entropic penalty that hampers the stability of such phases). We used molecular modeling to delineate phase diagrams, provide design guidelines for lithographic applications, and to explore the nucleation behavior of one of these phases from a disordered melt. We have used different strategies to modify the stability of bicontinuous phases by exploring the effect of distinct additives: (i) A cosurfactant (short DBC) that straddles the interface and alleviates packing frustration in both A and B-domains, (ii) two solvents selective to each phase that swells both domains unevenly (for potential nanolithographic applica-

tions), and (iii) an A-selective homopolymer that swells only one of the domains but provides additional configurational entropy to access bicontinuous phases beyond those found in pure DBC melts.

A combination of theory and molecular simulations is used to study these systems. Self-consistent field theory is fast and used to calculate free energies of prespecified morphologies but fails to include molecular fluctuations. Coarse-grained molecular simulations are slower and require more sophisticated techniques for calculating free energies but can capture molecular fluctuations and more realistically describe defects and kinetically trapped phases. Bicontinuous phases in the DBC + homopolymer system (namely the Gyroid, Double diamond and Plumbers Nightmare) are particularly challenging because they possess large unit cells with hundreds of molecules (and thousands of monomers) per unit cell, and the observed morphology depends strongly on simulation box size, which is unknown a priori. Accurate free energy estimates are required to ascertain the stable phase, particularly when multiple competing phases spontaneously form at the conditions of interest. A variant of thermodynamic integration was implemented to obtain free energies and hence identify the stable phases and their optimal box sizes. Clear evidence was found of phase coexistence between bicontinuos phases, consistent with previous predictions for the same blend using Self-consistent field theory. Our simulations also allowed us to examine the microscopic details of these coexisting bicontinuous phases and detect key differences between the microstructure of their nodes and struts.

BIOGRAPHICAL SKETCH

Poornima was born in Chennai, India in 1987. She got her Bachelor of Technology degree in Chemical Engineering from Indian Institute of Technologys Madras in 2009. It was there she was introduced to statistical mechanics and polymer physics which led her to join Cornell University in Fall 2009 for graduate studies. She joined Prof. Escobedo's research group and has been working on problems related to polymer self-assembly. She was a teaching assistant for graduate level Thermodynamics and Kinetics. Besides research and teaching, she is passionate about classical dance and music, and Scrabble.

This document is dedicated to all unprivileged students around the world who have a sense of curiosity and wonder about the world around them but do not have access to the resources to pursue an education program with peers, mentors and teachers.

ACKNOWLEDGEMENTS

I would like to thank several people who have made my journey possible and from whom I've learned invaluable lessons. Prof. Escobedo has been a great captain of the ship and has steered and shaped all of my projects. He has tirelessly edited several of my drafts and is always willing to discuss any and all details, no matter how tiny. Dr. Juan Carlos Araque showed me the ropes to solve my research problem, and taught me the skill to make attractive pictures when I first joined the group. Dr. Francisco Martinez-Veracoechea has shared his subtle observations which have led me to think deeper about my research. Prof. Clancy has been a wonderful mentor and has been very supportive and encouraging through all disappointments. Prof. Ober has been a great collaborator and motivated me to make my work applicable to experimental work. I'm also grateful to other professors in the department who have motivated me in the hallways, especially Dr. Zia who always encouraged me to dream big.

My family has had to put me back on the saddle several times; my father, *Appa* with his "there is no such thing as failure" pep talk, my mother, *Amma* with her optimism, and my brother, *Anna* who always reminds me of the big picture. My friends and colleagues in Ithaca have also been the best group of cheerleaders possible. Pooja and Jonathan have been sounding boards for not only my research ideas but also their humorous take on all things research. Priyamvada and Nidhi have given invaluable advice on thinking about my career. Folks at the Scrabble Club, Anjali, Asha and SPICMACAY and my board/card game buddies have all kept the creative (and competitive) side of my brain engaged. Within the department, CHEGSA and CBEWomen have been an incredible resource and support. Thank you everyone.

TABLE OF CONTENTS

LIST OF TABLES

LIST OF FIGURES

CHAPTER 1

INTRODUCTION

At the right conditions, diblock copolymers (DBCs) have a propensity to self-assemble into microstructures due to the balance between repulsive forces between unlike monomers and the connectedness of the monomers within a chain. Conventional structures such as lamellae, cylinders and ordered micelles have been thoroughly studied for about 25 years and thin films of these phases are currently being used for directed self-assembly (DSA) [106, 94, 20, 40, 12] in nanolithographic applications to build a variety of devices. Besides these structures, DBCs can also form bicontinuous network structures[100] where one of the monomers form two distinct interweaving networks within a matrix containing the other monomer. The topology of the network distinguishes between the various bicontinuous phases. Some of them such as the double gyroid (hereafter called gyroid or the G phase), the double diamond (hereafter called the diamond, or D phase) and plumber's nightmare (hereafter called the P phase) have been synthesized successfully in amphiphilic water-oil-surfactant emulsions[108]. These network structures are attractive for applications involving ordered nanoscale porous materials including solar cell active membranes, filters, catalysts, and nanolithographic templates[121, 126, 32, 90, 85, 46, 92, 96].

However, bicontinuous phases in self-assembled DBC systems are poorly understood despite decades of research due to several reasons. First, the G phase is the only stable bicontinuous phase in pure DBC melts; that too only within a very narrow region of the phase diagram[76, 119]. Phase diagrams of DBCs with additives have been predicted to stabilize D and P phases; again, in narrow regions. This requires precise synthesis of the building blocks (DBC molecules). Second, for

specific applications the targeted structures have to possess certain feature sizes (correlated to relative volume fractions of A-type monomer), which is in turn limited by the phase diagram. A second key issue is that their self-assembly is dogged by kinetic issues and the appearance of defects is common in these systems. Long anneal times often do not resolve these issues entirely. As far as we know, approaches similar to those used in DSA (successful in lamellae and cylinders) have not been applied to bicontinuous structures which are three dimensional. Third, kinetic factors become more important near phase transitions where free energies of competing phases are comparable and the propensity to nucleate defective or distorted phases is higher.

The narrow regions of stability of these phases have implications in experimental work. Several instances of misidentified phases abound in the experimental literature. Early during the discovery of the bicontinuous phases, the gyroid was mistaken to be a diamond phase (then called ordered bicontinuous double-diamond OBDD)[114]; and the OBDD was later reassigned to be the gyroid phase. Other experiments of DBCs with cosurfactants had inconclusive assignment of a bicontinuous phase between the region of stability of the lamellar and cylinder phases. Among the more complex bicontinuous phases, the D phase has only recently been discovered in a DBC blended with homopolymer[112]. The P phase remains elusive till date. Despite claims of a P phase discovered in a complex material with inorganic particles and block copolymers, it was later reassigned to a distorted G phase.

The small region of stability of bicontinuous phases has been attributed to two related ideas: One, packing frustration[53] and two, interfacial curvature[75]. In short, the packing of chains required to optimize entropy does not optimize the

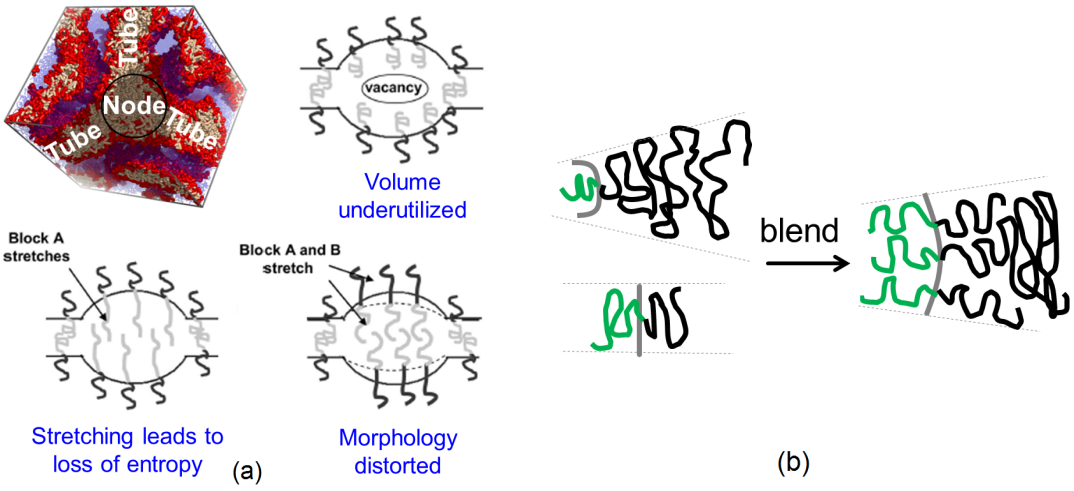

Figure 1.1: Illustrations of (a) Packing frustration showing cross-section of a G phase showing nodes and interconnecting tubes, and (b) Curvature modification using a cosurfactant. Gray lines mark the interface.

enthalpic energy and vice versa. This frustration in packing is worst for bicontinuous phases. As illustrated in Figure 1.1a, each of the bicontinuous networks is composed of tubes (struts) that are connected by nodes. The gyroid is the simplest bicontinuous phase with three tubes meeting at every node while the D and P phases have four and six tubes respectively meeting at every node. In order to accommodate meeting of multiple tubes, the nodes are bulkier than the tubes and thus the center of a node is farthest from the interface. If the DBC stretches to the same degree in the nodes and tubes, regions with low density or vacancies would arise within the node. To compensate for this, the minority blocks have to stretch which would lead to a loss of conformational entropy. If both blocks stretch, then the topology of the nodes is sacrificed and the morphology is distorted. Thus, only a delicate balance between chain stretching, local density fluctuations and interfacial distortions stabilizes the bicontinuous phases. Leveraging entropy thusly has been a hot topic for soft matter self-assembly in recent years; in particular for DBCs, entropy-stabilized corners have been developed in lamellar nanolithography

using appropriate homopolymers[107].

The second issue is related to minimizing enthalpic contacts between the two blocks and therefore, optimizing the interfacial curvature. Higher the volume disparities between the two blocks, higher the curvature. For example, Figure 1.1b shows a blend of two DBCs, which in their melt forms would form interfaces possessing different curvature, but when blended would form an interface of intermediate curvature. Bicontinuous phases have non-zero local curvature but zero mean curvature. So, as the volume disparity of the two domains increases, the lamellar phase often gives way to bicontinuous phases before leading to high curvature cylinders and micelles. As a result of these interactions, the G phase is the only stable bicontinuous phase found in pure melts of DBCs, and theoretical predictions show that the region .

The use of carefully chosen additives can circumvent all of these issues. By expanding the phase diagram with additional design parameters (e.g., size of the additive, strengths of interaction, relative volume fraction), we have new dimensions and handles with which to tune the morphology. Additives can increase the region of stability of the phase of interest, and in doing so, they could also decrease the propensity to possess defects where they are farthest from a coexistence region, or phase boundary. That being said, an inappropriate choice of additive (with unfavorable interactions) can also lead to macrophase separation. Therefore, a good understanding of the macroscopic *and* microscopic behavior of the additive of interest is required. this can be challenging in experiments due to the large number of variables involved in the phase diagram. Sweeping through all of them is impractical. Thus, modeling is useful in relatively quickly pinpointing regions of the phase diagram where the phase of interest is stable. We use coarse-grained

modeling that captures behavior at the length scale of the domain sizes. We use a combination of methods - self-consistent field theory (SCFT) which is fast and calculates equilibrium quantities but does not capture molecular fluctuations, and particle-based simulations (MD) which is slower but captures fluctuations, and allows us to study defects, transient features and non-equilibrium behavior of the phases.

In this dissertation, we have studied DBCs with three additives, each uniquely modifying the phase diagram and providing a route to access a bicontinuous phase. Apart from the strategy in choosing the chemistry and architecture of the chemical molecule, a secondary differentiating feature is the size of the additive relative to the DBC (α) and the selectivity of the additive to each block in the DBC. In Chapter 2[87], we study solvents where $\alpha \ll 1$. Addition of a solvent imparts enhanced chain mobility for the polymers (indirect temperature control), and the solvent selectivity causes it to swell non-uniformly into the two microdomains (indirect volume fraction control). We study two phase-selective solvents so that we can independently control the degree of temperature and volume control. Solvent annealing is extremely useful when morphology control is impossible via temperature changes that would degrade the DBC itself. In our blend, We start from a lamellae-forming DBC and obtain a stable G phase by adding solvents. Due to the disparate length scales of the solvent and DBC, we can only use SCFT to study this blend. In chapter 3[88], we use an intermediate value of $\alpha < 1$. We use a cosurfactant (shorter DBC) that straddles the interface and directly affects the interfacial curvature, and thus modifies the stability of the phase. Starting from two DBCs, one forming a cylinder and the other forming a lamellar phase we obtain a stable G phase by modifying the surface tension. Using particle-based simulations in addition to field-based simulations, we see a high propensity of defective phases

close to the appearance of the G phase. Furthermore, we find smaller domain sizes of bicontinuous phases compared to a pure DBC melt. In both the above strategies, the conformational entropy of the additive is not significant enough to alleviate packing frustration such that more complex bicontinuous phases are stabilized. In chapter 4, we use an additive only slightly smaller than the DBC ($\alpha \sim 1$) selective to only one of the blocks. We start with a G-forming DBC and add a selective homopolymer. This selectivity and high α causes the additive to behave like a dry brush within the A-domains thus expelled from the interface and targeting the bulky nodes. This strategy results in a region of stability of the D phase and coexisting D-P and D-G regions. It also dramatically improves the stability window for the G phase as well as tunability of the G phase. We also concurrently developed a technique to calculate free energy differences using modified thermodynamic integration with enough accuracy that would be able to resolve the phase diagram near a triple point of coexistence of bicontinuous phases. In Chapter 5, we summarize the results and suggest several future directions this work could take.

CHAPTER 2

PHASE BEHAVIOUR OF PMMA-B-PHEMA WITH SOLVENTS METHANOL AND THF: MODELING AND COMPARISON TO THE EXPERIMENT

2.1 Introduction

The self-assembly of block copolymers has long been used for the synthesis of materials for a variety of applications like photovoltaic devices[21], catalysts[126], enantiomer separation devices[32] and nanolithography[90]. Controlling the morphology and tailoring its feature size for a specific application are challenging because in block copolymer melts, these are primarily determined by two key parameters: interaction strength (FloryHuggins parameter χ times the degree of polymerization N) and volume fraction f of one of the blocks. Furthermore, after the copolymer has been synthesized (fixed f and N), the only handle available to tune the morphology is temperature (inversely related to χ). However, morphology control via temperature has some drawbacks since temperature annealing can access multiple phases only near the orderdisorder transition (ODT), and for many polymer chemistries of interest the ODT may be high enough to cause polymer degradation. Instead, solvent annealing of the block copolymer with varying solvent concentrations has been successfully used to tune the morphology[41, 1, 22, 6, 89]. Furthermore, in thin films, solvent annealing neutralizes the surface energy of the air interface allowing further morphological control[103, 18]. Although using a single solvent does provide some tunability, finding the ideal solvent quality and degree of selectivity (for either block at the temperature of interest) can be restrictive if only one among a handful of existing solvents is to be considered. This

limitation is readily removed by using a mixture of two (or more) solvents, so that, e.g., varying the composition of the solvent can allow tuning the solvent quality at a fixed temperature. This approach then provides multiple handles to control the morphology and feature size: the amount of solvent(s) in the mixture, the ratio of solvent quantities, and selectivity (determined by chemistry and temperature). Indeed, solvent vapor annealing has been shown to allow access to structures that are unattainable through thermal annealing[6, 89]. Recently, the two-solvent approach was used to successfully demonstrate control over the lamellar width of sub-20 nm lamellar domains[18].

Self-consistent field theory (SCFT) has shown considerable success in modeling the self-assembly of block copolymer melts at low to intermediate values of χN. In particular, it predicts the stability of the gyroid phase up to $\chi N = 100$[25], a prediction that has been verified in experiments[22]. Another advantage of SCFT is that it can be easily extended to include solvents. However, the SCFT equations quickly get computationally intensive as χN is increased due to the increase in the number of basis sets needed for numerical convergence, thus limiting the range of parameters that can be studied. Keeping this limitation in mind, we adopted this well-established theoretical framework for the present study.

Several theoretical studies have used SCFT to map out regions of the multidimensional phase diagram of block copolymers upon addition of solvents. A phase selective solvent lowers the overall χN[89] by acting as a plasticizer and swelling the polymer. It also alters the effective f value by inducing preferential swelling of one block domain. Several previous studies focused on the regime where the solvents were dilute and neutral, thus, $\chi_{eff} = \phi_{polymer}\chi$[43, 84] and there was no preferential swelling. In such cases the ODT decreases monotonically as more sol-

vents are added[84]. For a single *selective* solvent, the phase diagram shifts toward the selective phase[48], much like the shift of the phase diagram toward the block type having a larger Kuhn length. The solvent size is typically much smaller (a few Ångströms) than that of the block copolymer (tens of nanometres), and since the morphologies have feature sizes of the order of the block length, the solvent is approximated as a structureless particle with a finite size (with the ratio of solvent size to polymer size = α). The smallness of α has been found to lead to a fairly uniform spatial distribution of the solvent except near the interfaces[47].

The vast majority of the work with SCFT has focused on the effect of solvent on the formation of lamellar, cylindrical, and micellar phases[84, 47, 51, 8]. In this work we studied the phase behaviour of poly(methyl methacrylate)-*block*-poly(2-hydroxyethyl methacrylate) (PMMA-*block*-PHEMA) with tetrahydrofuran (THF) and methanol by using both solvent-annealing experiments and SCFT. Particularly, we are interested in exploring the thermodynamic stability of the gyroid phase since, unlike other phases commonly found in block copolymers, it is bicontinuous which means that the two block domains interweave uninterruptedly in all directions. This leads to nanostructures with enhanced mechanical stability (even if one of the block domains is etched away) and transport properties (for thermal or electrical conduction) that are the same regardless of sample spatial orientation; these qualities make the gyroid phase appealing for such potential applications as active porous matrices for solar cells[17], batteries, and separation devices. We find that the gyroid phase is observed in our experiments under conditions which are fairly consistent with those where SCFT predicts its stability.

The rest of this chapter is organized as follows. In section 2.2, the experimental results conducted by members of the Ober group are briefly described. In

sections 2.3 and 2.4 the theory and the estimation of model parameters used by the theory are respectively presented. In section 2.5 the modeling results are expounded and discussed. Finally, the main conclusions are summarized, followed by supplementary information and funding acknowledgements.

2.2 Description of experimental results

The block copolymer used was a 50:50 mass ratio PMMA-*block*-PHEMA, of molecular weight 40 kDa and polydispersity 1.08. The PMMA-*block*-PHEMA chemistry selected is appealing for nanolithography because it allows one to harness both a top-down approach[64] by virtue of one of the blocks being photosensitive, as well as a bottom-up approach by exploiting the self-assembly of the diblock chains into specific nano-segregated morphologies. The experiments were conducted by the Ober group at room temperature which is well below the glass transition temperature of the two blocks in the polymer. Upon thermal annealing, the pure copolymer forms a lamellar phase with about a 40 nm spacing.

Composition(vol%) (methanol/THF)	Film thickness (nm)	Swelling	Time (s)	Resulting morphology
Pure copolymer	145	1.00		Disordered (no annealing)
80/20	440	3.03	6300	Lying cylinders
50/50	368	2.53	6300	Spherical micelles
50/50	368	2.53	20700	Gyroid
20/80	460	3.17	6300	Lying lamellae

Table 2.1: Experimental parameters and results

A detailed explanation of the methods and their applications is the topic of a separate article[9, **?**]. In brief, the copolymer was spin-coated on a thin film. Due to rapid processing conditions, the as-spun thin film was disordered. It was then exposed to vapour with the solvent mixture composition of interest. The swelling

ratio is calculated as the ratio of film thickness after and before exposure to the solvent. The resulting morphologies were characterized by the analysis of both AFM images and in situ GISAXS measurements. In all cases, exposure of the film after solvent annealing caused rapid evaporation of the solvent preserving the same morphologies although with uniaxial shrinking. The solvent-annealing time and the resulting morphologies are listed in Table 2.1.

For the two extreme compositions, a lying cylinder morphology (finger-like AFM pattern) is obtained at the 80:20 methanol-THF ratio, whereas a lying lamella is observed at the 20:80 methanol-THF ratio. At the 50:50 methanol-THF ratio, a gyroid morphology (pin-wheel like AFM pattern) is observed at long annealing times but spherical micelles are seen at short annealing times. Given that the latter difference is observed for the identical swelling ratio, it suggests that kinetic effects were significant, or external conditions were not identical (or varied slightly over exposure time), or both. It would hence be helpful to use a theoretical framework like SCFT to try to outline the regions of thermodynamic stability for the different phases observed experimentally. A more detailed description of the experiments and results (including GISAXS spectra) is given in ref. [**?**].

2.3 Theory

Self-consistent theory[84, 48, 76, 109] treats the solvent as a structureless particle, the polymer as a continuous Gaussian chain and the entire system to be incompressible. For our system, there are four chemical 'species' denoted by subscript i in the system – two monomers (A, B) and two solvents (M, T), and three components (subscript c) – one block copolymer (P) and two solvents (M, T). The

Kuhn lengths of PMMA and PHEMA are given by b_A and b_B respectively, the total degree of polymerization is N and the fraction of PMMA in the copolymer is f. The overall volume fraction of the copolymer in solution is φ_P and those of methanol and THF are φ_M and φ_T, respectively; local densities are denoted by ϕ_i. The ratio of solvent size of methanol and THF to polymer size is α_M and α_T, respectively. In SCFT, particles are in effective fields $\{\omega_i(\mathbf{r}); i = A, B, M, T\}$. For each kind of species i in the system,

$$\omega_i(\mathbf{r}) = \sum_{j \neq i} \chi_{ij} N \phi_j(\mathbf{r}) + \xi(\mathbf{r}) \tag{2.1}$$

where $\xi(\mathbf{r})$ is a Lagrange multiplier to enforce the incompressibility constraint on dimensionless local concentrations, $\phi_A(\mathbf{r}) + \phi_B(\mathbf{r}) + \phi_M(\mathbf{r}) + \phi_T(\mathbf{r}) = 1$. The polymers are parameterized by a continuous contour variable $0 < t < N$. $q_P(r,t)$ is the chain propagator of the $0 - t^{th}$ region in a polymer chain at location r and obeys the diffusion equation:

$$\frac{\partial q_P(\mathbf{r},t)}{\partial t} = \begin{cases} \dfrac{Nb_A^2}{6}\nabla^2 q_P(\mathbf{r},t) - \omega_A(\mathbf{r}) q_P(\mathbf{r},t) & 0 < t < fN \\ \dfrac{Nb_B^2}{6}\nabla^2 q_P(\mathbf{r},t) - \omega_B(\mathbf{r}) q_P(\mathbf{r},t) & fN < t < N \end{cases} \tag{2.2}$$

with $q_P(\mathbf{r},0) = 1$. Its complementary from the $t+1^{th}$ to N^{th} region in the polymer chain is given by

$$\frac{\partial q_P^\dagger(\mathbf{r},t)}{\partial t} = \begin{cases} \omega_A(\mathbf{r}) q_P^\dagger(\mathbf{r},t) - \dfrac{Nb_A^2}{6}\nabla^2 q_P^\dagger(\mathbf{r},t); & 0 < t < fN \\ \omega_B(\mathbf{r}) q_P^\dagger(\mathbf{r},t) - \dfrac{Nb_B^2}{6}\nabla^2 q_P^\dagger(\mathbf{r},t); & fN < t < N \end{cases} \tag{2.3}$$

with $q_p^\dagger(\mathbf{r},1) = 1$. Under the assumption that the solvents are structureless, the diffusion equation for its propagator in the limit $N \to 0$ reduces to

$$\frac{\partial q_S(\mathbf{r},t)}{\partial t} = -\omega_S(\mathbf{r}) q_S(\mathbf{r},t); \qquad \{S = M, T\} \tag{2.4}$$

The partition function of the polymer is given by

$$Q_P = \frac{1}{V}\int \mathrm{d}\mathbf{r} q_P(\mathbf{r},1) \tag{2.5}$$

and for each solvent S is

$$Q_S = \frac{1}{V}\int \mathrm{d}\mathbf{r} q_s(\mathbf{r},1) = \frac{1}{V}\int \mathrm{d}\mathbf{r}\exp(-\alpha_s\omega_s(\mathbf{r})) \tag{2.6}$$

The local concentration for the polymer is

$$\phi_P = \frac{\varphi_P}{V}\int_P \mathrm{d}t q_P(\mathbf{r},t)q_P^\dagger(\mathbf{r},1-t) \tag{2.7}$$

and for the solvents are

$$\phi_S = \frac{\varphi_S}{V}\exp(-\alpha_S\omega_S(\mathbf{r})) \tag{2.8}$$

Finally, the free energy per molecule is given by

$$\frac{F}{kT} = -\sum_{c=\{P,M,T\}}\frac{\varphi_c}{\alpha_c}\ln\left(\frac{\alpha_c Q_c}{\varphi_c}\right) - \frac{1}{V}\int \mathrm{d}\mathbf{r}\left\{\sum_{i=\{A,B,M,T\}}\omega_i(\mathbf{r})\phi_i(\mathbf{r})\right\} \tag{2.9}$$

Equations 2.1 through 2.9 are solved self-consistently using the Polymer Self Consistent Field (PSCF) code[79] which requires a good initial guess for convergence. The ternary phase diagram at a given χN and α was systematically mapped out using the solution from a nearby point for quick convergence. The starting point was chosen as a PMMA-*block*-PHEMA copolymer melt. Methanol was subsequently added (traversing along one axis in composition space) and finally THF was added to span the rest of the phase diagram. Initial simulations were run using only the lamellar and cylindrical phases to quickly search the parameter space; the parameters were then tweaked to produce a cylinder phase in methanol-rich regions and a lamellar phase in THF-rich regions. It was also checked that the choice of traversal of the axis (methanol first and THF second, or *vice versa*) did not affect the free energy calculation.

The number of basis sets N_b required for convergence of the numerical simulation increases rapidly as the Flory-Huggins parameter increases; this is because the

	PMMA	PHEMA
Molecular weight of monomer (g mol^{-1})	100.12[29]	130.14[29]
Degree of polymerization	200	154
Kuhn length (nm)	1.7[93]	1.03[33]
Mole fraction	0.57	0.43
Volume fraction	0.52	0.48

Table 2.2: Polymer parameters

block interfaces become sharper and more basis functions are needed to describe the domain shapes. This large number of basis sets rapidly escalates the simulation time needed, especially as the dimension of the morphology increases (lamellae are one dimensional, cylinders are two-dimensional, while gyroid and spherical micelles are three-dimensional). The inclusion of three-dimensional phases severely limits the range of the Flory-Huggins parameter accessible by the theory.

2.4 Calculation of parameters and modeling details

The input parameters in SCFT include chain architecture, volume fraction of the chain, Flory-Huggins interaction parameters and solvent size. Table 2.2 gives details of the chain architecture in the analogous experiments. Based on the monomer volume, PMMA has approximately 3 monomers per Kuhn segment while PHEMA has about two. Since a Kuhn segment is composed of about two to three monomers, the effective degree of polymerization N to be used in the SCFT model is $200/3 + 154/2 \approx 144$. The Flory-Huggins parameter captures the enthalpic chemical interaction between every pair of species. A positive value indicates repulsive energy whereas a negative value indicates attractive energy. Various empirical formulae exist in the literature to estimate the Flory-Huggins parameters for polymer-polymer, solvent-solvent and polymer-solvent interactions. In this work,

	V_{ref} (cm^3 mol^{-1})	δ_d	δ_p	δ_h
		($J^{1/2}$ $cm^{3/2}$)		
PMMA (group contribution)	85	17.66	5.76	7.82
PHEMA (group contribution)	107	17.3	6.51	15.57
THF	81.7	16.8	5.7	8.0
Methanol	40.7	15.1	12.3	22.43

Table 2.3: Solubility parameters[122, 3] used in the estimation of Flory-Huggins interaction parameters using Equation 2.11.

we used the relationship between the Flory-Huggins parameter and solubilities of the constituents which follows the general principle that 'like solvates like'. It is estimated by the relationship[7]:

$$\chi_{12} = \frac{V_{ref}}{RT} (\delta_1 - \delta_2)^2 \tag{2.10}$$

where χ_{12} is the Flory-Huggins parameter, V_{ref} is the reference volume and δ_i is the Hildebrand solubility parameter (for nonpolar species) of the constituent i. Note that with this formalism the Flory-Huggins parameter cannot be negative and it is inversely proportional to temperature, allowing us to use scaled parameters. For our system, we have used the set of three Hansen solubility parameters[42] in order to incorporate polar and hydrogen bonding effects into the single Flory-Huggins parameter with the relationship

$$\chi_{12} = \frac{V_{ref}}{RT} \left[(\delta_{1,d} - \delta_{2,d})^2 + (\delta_{1,p} - \delta_{2,p})^2 + (\delta_{1,h} - \delta_{2,h})^2 \right] \tag{2.11}$$

The Hansen solubility parameters have a contribution from dispersive (subscript d), polar (p) and hydrogen bonding (h) forces. The solubility parameters for the polymers vary considerably across the literature based on the estimation technique, and, for this current work, these are estimated from group contribution methods[122]. The solubility parameters for the solvents are from standard tables[3]. Table 2.3 lists the values of solubility parameters used and Table 2.4 lists the values of Flory-Huggins interaction parameters at 298 K scaled by $\chi_{PMMA-PHEMA} \approx 2.08$. Thus, χN would be 300 for the block copolymer.

$\chi/\chi_{PMMA-PHEMA}$	PMMA	PHEMA	THF	Methanol
PMMA	0	1	0.01	4.31
PHEMA	1	0	0.96	1.4
THF	0.01	0.96	0	4.18
Methanol	4.31	1.4	4.18	0

Table 2.4: Flory-Huggins parameters normalized by $\chi_{PMMA-PHEMA}$.

It can be inferred from Table 2.4 that methanol is a poor solvent, with its interaction with PHEMA being more unfavourable than that of PMMA with PHEMA. On the other hand, THF and PMMA have almost identical interaction parameters; the key difference between them being that THF is a structureless solvent while PMMA is a chain that has conformational degrees of freedom.

2.4.1 Test runs and adjusting χN and α

For computational expediency, some departures from experimental conditions were introduced. The experimental system consists of a thin film of thickness of a few hundred nanometres (see Table 2.1), which is many times the unit cell of any morphology of interest. The films were cast on native silicon oxide whose polarity imparts some affinity for the polar groups in both PMMA and PHEMA segments and hence one would expect both polymers to have similar substrate wetting properties (the analysis of "as spun" films of the pure diblock copolymer revealed domains with no long-range order nor preferential orientation with respect to the interfaces). While solvent annealing tends to neutralize the surface energy of the air interface, its effect on substrate wetting is more difficult to assess. It is expected that any preferential substrate-polymer interaction will primarily affect the orientation of block domains (relative to the surface) rather than the type of morphology (phase) that it forms. However, if a strong substrate preference for one

block was to occur then the tendency to form, for example, a lying lamellar phase could be enhanced. For our study, we will neglect interfacial effects and focus only on bulk properties, assuming that both solvents are absorbed in the bulk phase. The swelling factor is thus the inverse of the average block copolymer volume fraction. The Flory-Huggins parameters in Table 2.4 only provide a qualitative picture of the interactions because errors in estimation of solubility parameters propagate and are magnified when using Equation 2.11. Since the experiments showed a gyroid phase between cylinder and lamellar phases as the solvent ratio was varied, we perform initial tests probing the stability of lamellar and cylinder phases for a range of conditions. The tests indicated that either a larger FloryHuggins parameter disparity between methanol and PMMA, or a larger solvent size than experimental conditions is required to achieve stable cylinder and lamellar phases in the range of compositions of interest.

Since the simulation becomes costly on increasing the Flory-Huggins parameter disparity, we only use the ratio fixed by the Hansen solubility parameters. The scaled Flory-Huggins parameters in Table 2.4 reflect the actual chemistry of the copolymer and solvents, and we will refer to $\chi_{PMMA-PHEMA}$ as χ henceforth. The other parameters are scaled according to Table 2.4. Furthermore, the range of c explored is limited to $20 \leq \chi N \leq 40$ (and 50 in a special case) due to computational expediency, which is much smaller than the value of 300 that was estimated in the previous section. The contribution to the mixing free energy in Equation 2.9 increases inversely as the size of solvent is reduced. Indeed at a very low solvent size (and thus, low α), the disordered phase is favored; and a very high α results in a breakdown of the assumption of structurelessness of the solvent in comparison with the block copolymer. In order to compensate for the relatively low value of χN that we can practically adopt, we increase α but stay

within a range of values that has been used in previous SCFT studies of block copolymers with solvents[84, 48, 47, 51, 8]. Specifically, we performed simulations with $\alpha_{methanol} = 0.002$ (closest to the experimental value), 0.005 and 0.01. α_{THF} is scaled accordingly. A similar approach was used in a previous SCFT study wherein a lower χN and solvent molecules with the same size of the statistical monomer unit ($\alpha \sim 0.005$) were used to model the lamellar to cylinder transition observed in experiments of PS-PMMA with two solvents[34]. Henceforth, we will only refer to the parameter $a_{methanol}$ and drop the subscript. The phases studied are disordered (homogeneous), lamellar, cylindrical and gyroid phases. The BCC spherical micellar phase has been included only in a special case due to the difficulty in attaining convergence for this phase with a 50:50 block copolymer. Free energies of various phases under study are compared and the one with the lowest free energy is identified as the stable phase (the normalized free energies are calculated to be within 10^{-4}). In all cases studied, we do not find multiphase coexistence (see Section 2.7 for more details).

2.5 Modeling results

Three dimensional ternary phase diagrams for the PMMA-*block*-PHEMA + methanol + THF system are shown in Figure 2.1 for different choices of χN and α parameters. The vertex on the right in each horizontal plane corresponds to pure DBC and thus a swelling factor of 1. The vertex on the left is pure methanol and the vertex on the far back is pure THF. The experimental observations are overlaid by dashed lines/shaded regions for visual comparison. Since the exact partitioning of the solvents into the experimental polymer film is unknown, we assume that the solvent compositions match those of the annealing vapor phase. The vertical axis

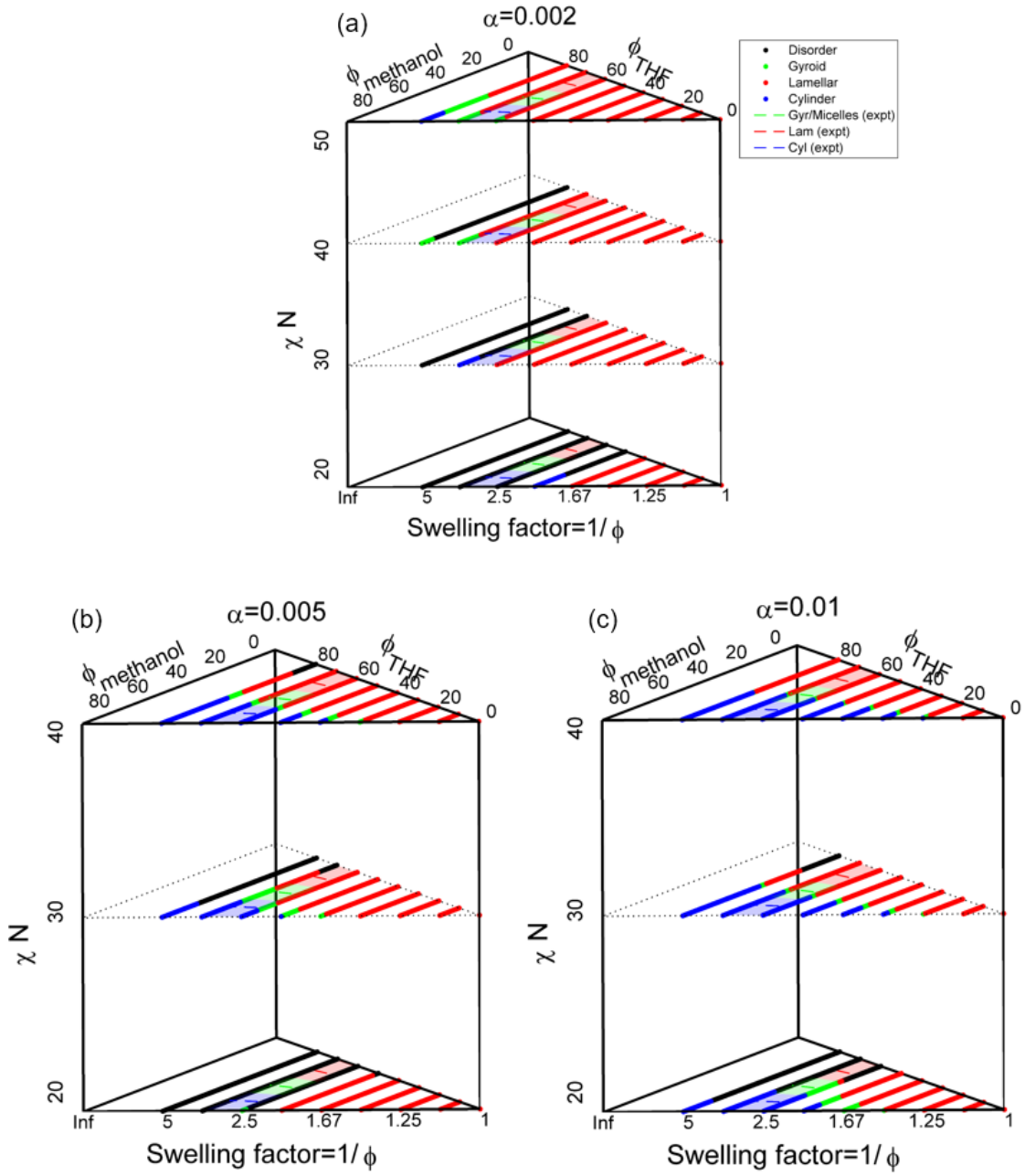

Figure 2.1: Ternary phase diagram for $\alpha = 0.002$, $\alpha = 0.005$ and $\alpha = 0.010$. The dashed lines and shaded regions represent the region of swelling ratios and solvent compositions studied by the experiments.

at a swelling factor $\varphi_{DBC} = 1$ corresponds to the phase diagram of the pure diblock copolymer. Since we have a near 50-50 volume ratio and above $\chi N_{ODT}(\sim 10.5)$ for a melt, we find a stable lamellar phase at this axis for all values of χN in Figure 2.1a through 2.1c.

For $\alpha = 0.002$ (Fig. 2.1a), a transition to the disordered phase takes place as the swelling factor is increased. Since $\chi_{methanol-polymer} > \chi_{THF-polymer}$, the THF-rich mixture undergoes an ODT at lower solvent concentrations than the methanol-rich mixture at a given swelling factor and χN. As χN is increased, the ODT occurs at higher solvent concentration (and thus, a higher swelling factor). Interestingly, the transition to the disordered phase is different between the methanol-rich and the THF-rich regions. The THF-rich region undergoes a lamellar to disordered transition, while in the methanol-rich region, the disordered phase may be approached via the cylinder, gyroid or lamellar phases depending on the χN and swelling factor. As justified in the previous section, we also explore the phase diagram for higher solvent sizes.

The phase diagram for $\alpha = 0.005$ is shown in Figure 2.1b. At $\chi N = 20$, the stable phases are the lamellar and disordered phases. At $\chi N = 30$ and higher, the methanol-rich axis transitions from the lamellar to the gyroid to the cylinder phase as the swelling factor increases. At a given swelling factor, depending on the starting point at the methanol-rich plane, a cylinder to gyroid to lamellar transition occurs as the THF fraction in the solvent mixture is increased. Furthermore, the gyroid region of stability is the widest for $\chi N = 30$ and gets narrower as χN is increased.

The phase diagram for $\alpha = 0.01$ in Figure 2.1c is qualitatively similar to that in Fig. 2.1b except for an apparent shift upward of χN as α is increased; e.g., the

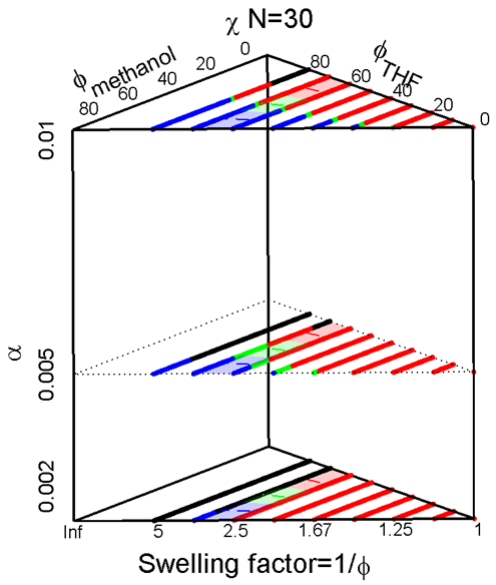

Figure 2.2: Phase diagram at constant χN for increasing α.

diagram for $\chi N = 40$, $\alpha = 0.005$ looks most similar to that for $\chi N = 30$, $\alpha = 0.01$. Figure 2.2 illustrates this by showing the effect on increasing α at constant χN which looks qualitatively similar to Fig. 2.1b. Thus, in this region of phase space explored, we have an effective χ parameter that increases monotonically with φ and α.

2.5.1 Approximate comparison with the experiment

For a specific case of parameters ($\chi N = 30$, $\alpha = 0.01$), we have also included the BCC spherical micellar phase and double diamond phase in the calculations for obtaining the phase diagram (plotted in Figure 2.3). Here, the diamond phase is not stable in any region of the phase diagram while spherical micelles replace part of the phase region where cylinders are stable in Figure 2.2. The spherical micelles become stable near the ODT and the methanol-rich region. Comparing Figure 2.3 with Figure 2.2, the progression of phases is much the same upon including

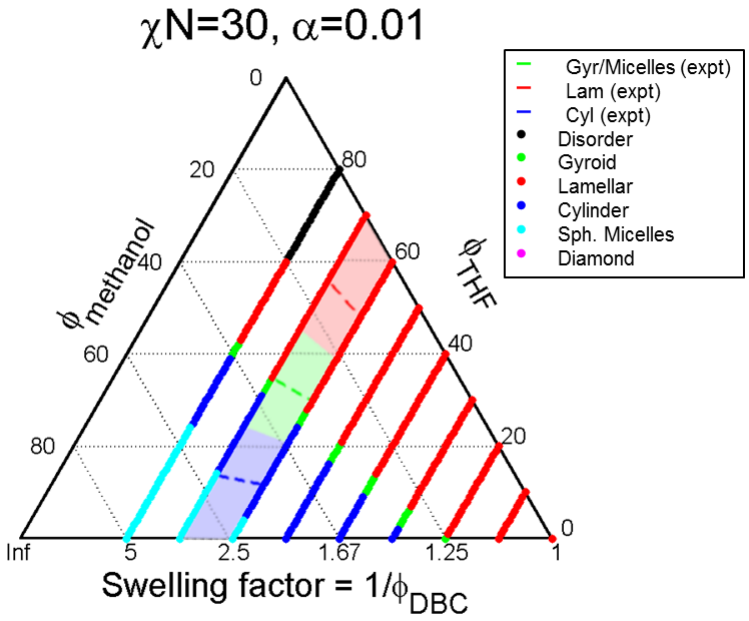

Figure 2.3: Phase diagram including spherical micelles and double diamond in the calculation. Minority phase = PMMA.

the spherical phase (lamellar to gyroid to cylinder to spherical micelles) and is consistent with the effect of reduced χ_{eff} on increasing swelling. Consistent with experimental data, the theory predicts the presence of cylinder and lamellar phases at the 80:20 and 20:80 methanol-THF ratios respectively.

From the theory, near the 50:50 methanol-THF region, one would expect a transition from the micelle to the gyroid phase upon increasing the methanol-THF ratio to occur via an intermediate cylinder phase. In the experiments, this intermediate phase was not seen. One reason for this discrepancy could be that the experimental solvent composition in the polymer film is not necessarily identical to that of the imposed vapor phase composition due to partitioning of components among the vapor and film phases (and that these compositions may have slightly changed during a long annealing period). Even in the simplest case of a binary methanol and THF mixture, the ompositions of the coexisting vapor and liquid

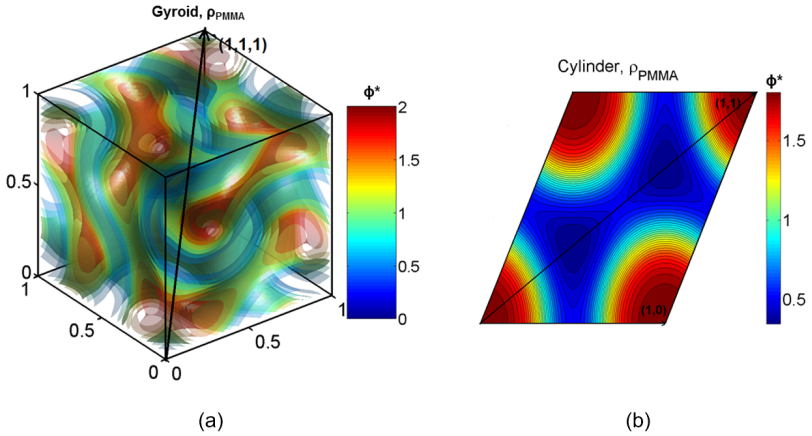

Figure 2.4: Isosurfaces of normalized density ϕ^* of PMMA for (a) the gyroid phase and (b) the cylinder phase.

phases would not be identical[68]. A second possible reason for the absence of the cylinder phase in experiments for this case could be slow kinetics of the gyroid to cylinder transition. Previous studies in the literature of block copolymer melts have shown epitaxial pathways of instability for $\chi N = 20$ and lower[91, 70, 124, 71]. This region of metastability of the gyroid phase for a pure block copolymer melt was shown to extend well into the cylinder phase, close to the cylinder to micelle transition[71]. Furthermore, the free energy barrier for the gyroid to the cylinder phase increases with χN[70]. This scenario seems likely given that the morphology at the 50:50 solvent ratio in experiments nucleates from a disordered film and evolves over time.

2.5.2 Density distributions across the microstructure

We also investigated the spatial distribution of densities normalized by the overall volume fraction of the various components. The densities of the polymer blocks usually vary widely between zero and its maximum value while the solvents, being

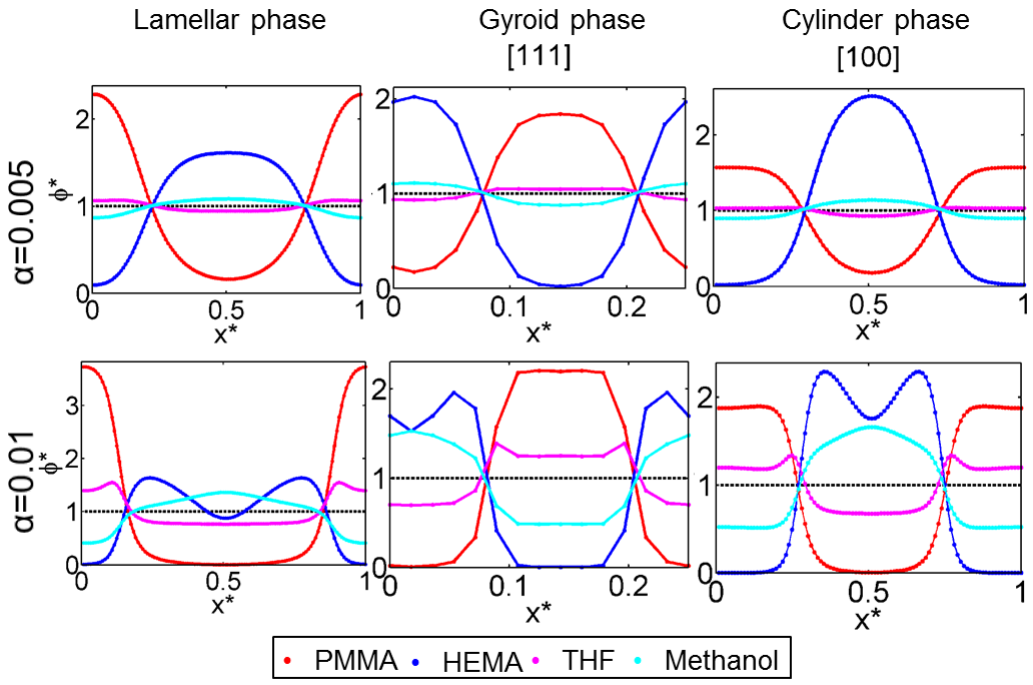

Figure 2.5: Effect of increasing a on the density distributions of different components. Morphologies relevant to $\chi N = 30$, swelling factor = 3.3 with 80:20 methanol-THF. The lowest value of α is not shown here (disordered phase produces a flat distribution of densities).

much smaller, have a more uniform distribution with smaller variations of density from its average, by less than 10% for low values of α. As the swelling factor is increased, the width of the interface increases and the relative density deviations about the mean are suppressed, eventually leading to a disordered phase (not shown). THF and methanol behave slightly differently. THF accumulates at the PMMA-PHEMA interface, whereas methanol prefers the center of the PHEMA domain. Due to the high selectivity of methanol, increasing the ratio of methanol to THF increases the relative width of the PHEMA domain for all phases under study (not shown).

On the other hand, increasing the ratio of THF to methanol results in a higher

accumulation of THF at the interface, with no significant change in the relative width of the PMMA domain. Figure 2.4a and b show density isosurfaces for gyroid and cylinder phases respectively, obtained under identical conditions $\chi N = 30$, $\alpha = 0.005$, swelling factor = 3.3 with 80:20 methanol-THF. Figure 2.5 shows a comparison of density distributions for different phases as the solvent size increases. For the sake of clarity, density distributions for multidimensional phases in Figure 2.5 are shown along the vectors denoted in Figure 2.4a and b. For $\chi N = 30$, a swelling factor of 3.33 and 80:20 methanol-THF, as α is increased from 0.002 to 0.01, the stable phases are disordered, gyroid and cylinder (see also Fig. 2.2a). As α is increased, methanol exhibits a stronger preference for the core of the PHEMA-rich domains. For $\alpha = 0.005$ the positive (and negative) relative deviations in density from the average is about 20%, whereas for $\alpha = 0.01$ this deviation is as high as 50%. In this case, even PHEMA is repelled from the core of the majority domain and is concentrated near the interface.

The aforementioned effect of methanol exclusion from the centers of the PHEMA domain is not seen when increasing χN at fixed α (Figure 2.8 in Section 2.7), at least within the range of χN explored. This suggests that although the "macroscopic" phase diagrams look qualitatively the same on either increasing χN or increasing α, due to changes in the "microscopic" behavior of solvent distribution, these scenarios are certainly not equivalent.

From SCFT, one can also get domain sizes of various morphologies. Figure 2.6 shows the region of the phase diagram where the lamellar phase is stable, color coded by the domain spacing (normalized by that of the pure block copolymer). As swelling increases, the domain size decreases, an effect that is minimal in the methanol-rich region and becomes larger as the THF-methanol ratio is increased.

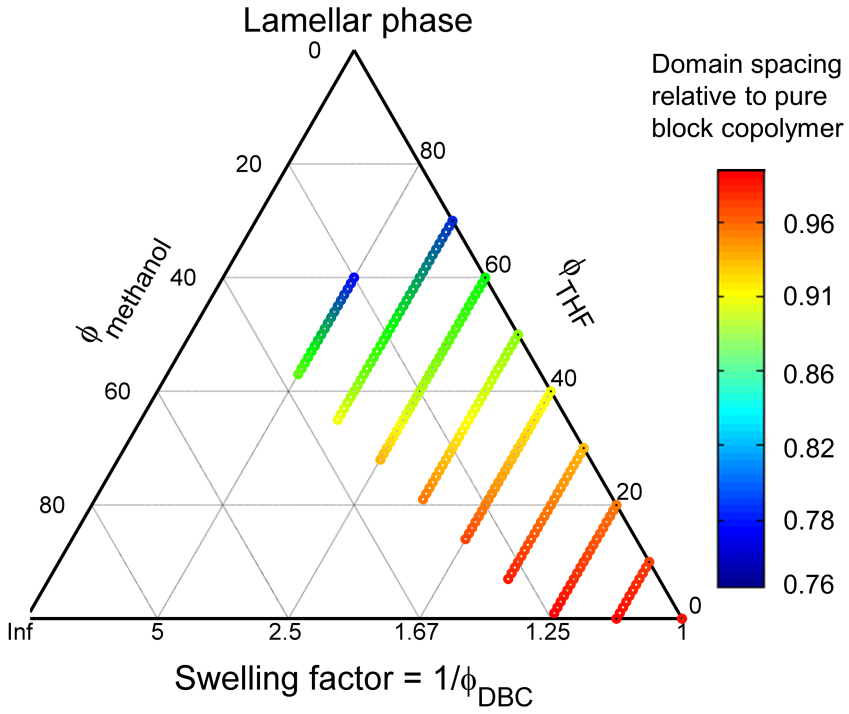

Figure 2.6: Effect of solvent addition on domain spacing for the lamellar phase at $\chi N = 30, \alpha = 0.01$.

The largest spacing reduction we observe (26%) is more significant than that (9%) reported in ref. [18] (for a different system), likely a reflection of the larger swelling ratios we explore. A simplistic explanation of this spacing-reduction is that when the domains are swollen by a good solvent (like THF), the inter-block interfacial tension decreases and its area increases; hence the polymer chain "brushes" that stick out from opposite sides can interpenetrate more. Domain size reduction and enlargement can occur for other phases also (results not shown). Figure 2.6 further illustrates (as in ref. [18]) that solvent annealing may be an effective technique for decreasing the domain size (appealing for lithographic applications), and particularly in our case, for the lamellar phase which occurs for THF-rich conditions.

2.6 Conclusions

We have studied the phase behaviour of 50:50 PMMA-*b*-PHEMA with methanol and THF using both experiments and an approximate model via SCFT. Experiments limited to 3 solvent compositions (and for specific swelling ratios) revealed the formation of different phases including the gyroid phase. Given the uncertainties and challenges associated with exactly matching experimental systems with model parameters, we used SCFT to investigate the dependence of the phase diagram for intermediate values of Flory-Huggins interaction parameters and a range of solvent sizes. Starting from a pure diblock copolymer, increasing the swelling leads eventually to a disordered phase, a process that occurs via the gyroid and cylinder phases near the methanol-rich region, and via a direct lamellar to disordered transition near the THF-rich region. These trends agree well with the accepted tenet that addition of solvents effectively decreases χN and shifts the effective composition of the diblock copolymer towards the more selective solvent by inducing non-uniform swelling. Increasing the solvent size leads to preferential swelling and at $\alpha = 0.01$, it results in depletion of PHEMA at the methanol-rich core of the PHEMA domains. Consequently, the cylinder and gyroid phases are stabilized for significantly larger regions of the phase diagram.

Besides morphological control, co-solvent annealing also allows some control on the domain size by tuning the swelling factor and solvent ratio. Based on the density distribution of the various components, the stability of cylinder and gyroid phases could be attributed to alleviation of packing frustration of the copolymer by the solvents, particularly methanol. Increasing χN also leads to the stabilization of these phases, although over the range of χN values studied this effect was milder than that of the increasing solvent size. Since simulating high values of χN is

computationally prohibitive, we proposed a combination of a somewhat higher α and lower χN than experiments to mimic the phase behavior at high χN, at least qualitatively. We observe a cylinder to gyroid to lamellar phase transition as the ratio of methanol-THF is increased over experimentally relevant swelling factors, although the location of the predicted phase boundaries does not exactly coincide with experiments. This limitation may be partially rooted on the errors associated with the estimation of χ values from solubility parameters; better estimates of the χ parameter should yield more accurate theoretical predictions. Other sources of error may have also been at play in the experiments such as uncertainties on the molecular weights (and polydispersity) of the polymers, variation in the solvent composition, and the possible occurrence of longlived metastable states.

Altogether, our theoretical calculations are consistent with the experimental finding that, starting with a 50:50 block copolymer, the gyroid phase can be stabilized by swelling with a mixed solvent of a suitable composition. They also validate the general strategy of using a mixture of two solvents as a means to vary the solvent quality to allow access to different phases of interest even at a fixed temperature; and provide a comprehensive phase diagram for future experiments to rely on. Whether such a strategy could be used to target bicontinuous phases other than the gyroid remains to be explored but we suspect that non-symmetric block copolymer compositions could be more suitable and that at least one oligomeric "solvent" would be needed to more drastically alleviate the packing frustration that is typically associated with the lack of stability of such complex phases[66, 77]. Our results also suggest some areas that need further improvement and investigation. A more atomistic approach or additional experimental data (for calibration) would be needed to obtain more reliable χ parameters and overcome some of the limitations associated with the group-contribution methods that we

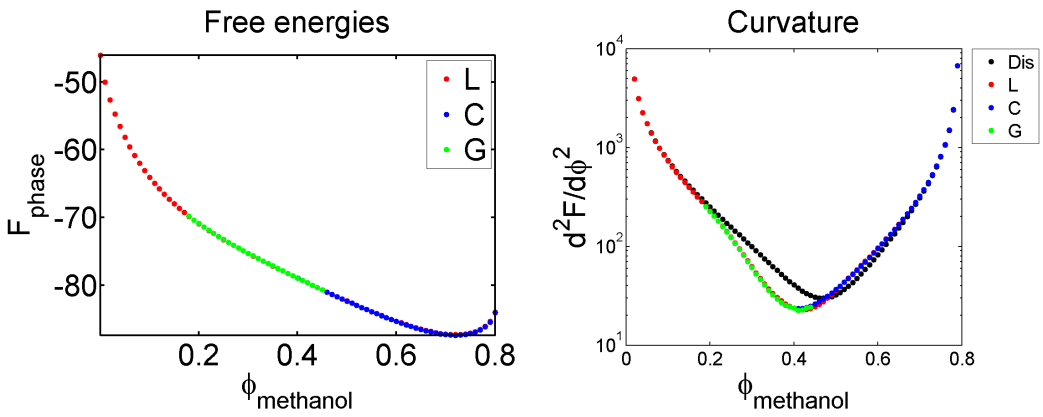

Figure 2.7: Free energy values and curvature at $\chi N = 40$, $\alpha = 0.01$, swelling factor $= 5$.

adopted in this work. Also, more experimental and modeling work is needed to elucidate the pathways and kinetics rates associated with the formation of different phases and their inter-conversion.

2.7 Supplementary information

2.7.1 Possibility of two-phase coexistence

The curvature of free energy (second derivative) with respect to volume fraction was calculated to detect multiphase coexistence. Two-phase coexistence occurs when the curvature of the free energy-volume fraction graph becomes negative, or contains an inflexion point[84]. The curvature is calculated from the second-order central finite difference, i.e.,

$$\frac{\partial^2 F}{\partial \varphi^2} = \frac{F(\varphi + \Delta\varphi) - 2F(\varphi) + F(\varphi - \Delta\varphi)}{(\Delta\varphi)^2}$$

For all points studied, we did not observe a negative curvature although as α was increased the curvature became less positive. Figure 2.7 shows the free energy and

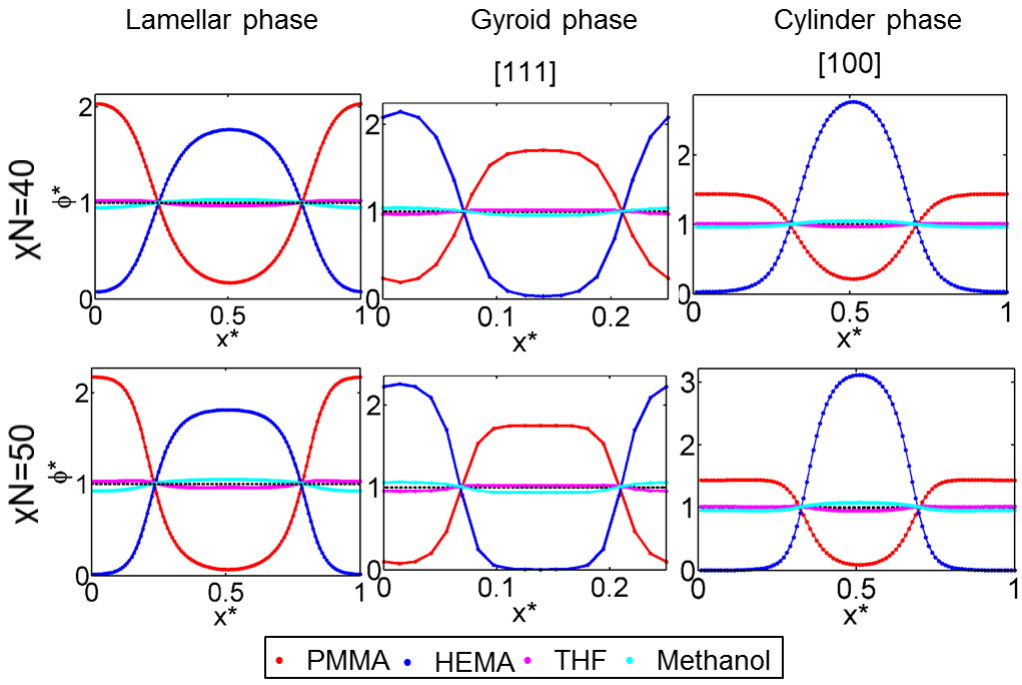

Figure 2.8: Effect of increasing a on the density distributions of different components. Morphologies relevant to $\chi N = 30$, swelling factor = 3.3 with 80:20 methanol-THF. The lowest value of α is not shown here (disordered phase produces a flat distribution of densities).

curvature at $\chi N = 40$, $\alpha = 0.01$ and swelling factor = 5 where the curvature was least positive near 50:50 methanol-THF.

2.7.2 Normalized density distribution on increasing χN

Figure 2.8 shows the density distribution of all the components when increasing χN from 30 at the smallest solvent size. Two effects can be seen: first, the interface gets sharper as χN is increased, and second, the solvent distributes uniformly across both (PMMA-rich and PHEMA-rich) domains and its density variation (around the average) is only ∼5%. This variation is much smaller than that observed upon

increasing the solvent size (as illustrated in Figure 2.5).

2.8 Acknowledgements

This work was supported by Grant CBET 0756248 from the National Science Foundation. We are thankful to Prof. David Morse from the University of Minnesota for the code for implementing SCFT. F.A.E. is grateful for computer cycles supplied by the Extreme Science and Engineering Discovery Environment, which is supported by the National Science Foundation Grant no. ACI-1053575.

CHAPTER 3

A THEORETICAL AND SIMULATION STUDY OF THE SELF-ASSEMBLY OF A BINARY BLEND OF DIBLOCK COPOLYMERS

3.1 Introduction

Diblock copolymers "DBCs" are linear polymers made up of two types of homopolymers (blocks) joined end-to-end. Due to the chemical incompatibility between the monomers, they tend to segregate but cannot do so at the macroscale because of their intramolecular linkage. Exploiting such a tendency for microphase segregation, block copolymers have been used for nanotemplating materials useful in lithography and the synthesis of nanoporous structures for multiple applications including catalysts and solar cell active layers. Of particular interest are bi- and cocontinuous phases that have three-dimensional symmetry, with continuous domains of the different block types. These phases have superior electrical, mechanical, and optical properties[96, 17, 126] which are essentially isotropic; i.e., they do not depend on a particular alignment of the morphology with respect to external interfaces. This is because these phases have either two interweaving (bicontinuous) networks or a single (cocontinuous) network, of the minority block embedded in a matrix of the majority block.

Unfavorable enthalpic interactions in DBCs drive the formation of interfaces during microphase segregation, restricting the junction points of the two different blocks to lie at or near the interface. On the one hand, formation of the interface localizes sections of the DBC chains reducing the configurations they can explore and hence the conformational entropy. On the other hand, the interface tends

to curve towards the minority domain allowing the blocks to balance the amount of stretching required to fill the space. The interplay between these interactions determines the stable microphase[75].

The confluence of results from experiments and self consistent field theory (SCFT) has led to a detailed understanding of the phase diagram of a pure melt of DBCs[72]. Under some approximations, such a phase diagram is completely described by two parameters: The volume fraction of one of the components f, and the product of Flory-Huggins interaction parameter and the degree of polymerization χN. The phases found to be stable (over particular $f - \chi N$ regions) are the micellar (body-centered-cubic and close-packed), cylindrical (hexagonally packed), gyroid, and lamellar phases. Recent SCFT calculations have resolved another fifth stable phase[119] of cocontinuous morphology, O^{70}, which has subsequently been observed in experiments[56].

The incorporation of an additional species to a DBC melt adds more dimensions to the phase diagram, although it also opens up the possibility of macrophase separation. Nevertheless, the new dimensions potentially allow a larger window of stability of the desired phases and perhaps conditions more accessible via experiments. In particular, adding a second DBC made of the same chemical species forces both species to share the interface; such an additive is often referred to as the "cosurfactant". Shi and Noolandi[101] first studied the effect of adding a very small amount of surfactant and analytically studied the change in interfacial tension and its contribution to the free energy. Early work focused on polymers of the same total degree of polymerization but different block lengths (allowing a common χN value for the system). For dilute blends, a one-component approximation was shown to be valid using theory[74]. Later studies on blends over a wide range of

compositions have mapped out macrophase separation and two-phase coexistence, but they were restricted to the cylinder, lamellar, micellar, and disordered phases only, and did not consider the gyroid phase or other bicontinuous and cocontinuous phases[73, 60].

Experiments have shown that it is possible to obtain bicontinuous and cocontinuous phases by blending suitable DBCs – typically an asymmetric copolymer and a symmetric copolymer[105, 16, 11]. It was also shown that blending two symmetric DBCs does not always lead to a lamellar phase, but also to a spongy phase. Hashimoto and co-workers[16, 11] studied a binary blend of asymmetric and symmetric DBCs in detail, and found an unidentified bicontinuous phase in between cylinder and lamellae. Spontak et al.[105] studied a bidisperse blend of DBCs and found a similar behavior, a cylinder to gyroid to lamellar transition upon increase of overall volume fraction of the minority domain. The preparation method was also found to be critical in determining the observable morphology of the binary blends[60]. Previous simulations[52] have shown that for a bidisperse system of carefully chosen composition, the region of stability of the gyroid phase is enhanced due to the preferential arrangement of the longer diblock at the nodes of the gyroid network.

The present work explores via SCFT and particle-based simulation the phase behavior of a binary blend of DBCs consisting, as in former experimental systems, of a longer asymmetric DBC and a shorter, symmetric DBC. A specific goal is to complement previous experimental observations to clarify, in particular, the stability of the gyroid phase versus other bicontinuous or cocontinuous phases, an issue that was left unresolved in the study of Court and Hashimoto[16]. We find that while SCFT does predict the existence of a narrow composition range where

the gyroid phase is stable, particle-based simulations are unable to resolve among the gyroid phase, cylindrical phase, and a disordered cocontinuous phase. The latter simulations also reveal that such a result is partially due to the existence of packing frustration in the majority-block domains of the gyroid phase.

3.2 Simulation Methods

3.2.1 Self-Consistent Field Theory

In SCFT, polymer chains are modeled as flexible Gaussian chains. The main idea is to replace the calculation of the partition function of the entire system by the calculation of the partition function of a single chain in an external field. Here, we describe the theory for a bidisperse block copolymer blend. For each component c in the blend, the degree of polymerization is N_c and the volume fraction of monomer of type A is f_c, with φ_c the overall volume fraction of the component. χ is the Flory-Huggins interaction parameter between unlike monomers A and B, and N is the chain length of one of the components chosen as the reference. The set of equations for the external fields for the canonical ensemble are[75, 72, 119]:

$$\omega_A(\mathbf{r}) = \chi N \phi_B(\mathbf{r}) + \xi(\mathbf{r}) \tag{3.1}$$

$$\omega_B(\mathbf{r}) = \chi N \phi_A(\mathbf{r}) + \xi(\mathbf{r}) \tag{3.2}$$

$$\phi_A(\mathbf{r}) + \phi_B(\mathbf{r}) = 1 \tag{3.3}$$

where ϕ_i are local density fields that satisfy the incompressibility condition (Equation 3.3), $\xi(\mathbf{r})$ is the Lagrange multiplier introduced to enact the incompressibility constraint, and $\omega_i(\mathbf{r})$ is the mean field that acts on a subunit of monomer type i.

The chain propagators "q" obey a diffusion-type of equation,

$$\frac{\partial q_c(\mathbf{r},t)}{\partial t} = \frac{N_c b_i^2}{6}\nabla^2 q_c(\mathbf{r},s) - \omega_i(\mathbf{r}) q_c(\mathbf{r},s) \tag{3.4}$$

for each component c in the blend, b is the Kuhn length of monomer i, s is a contour variable between 0 and 1 specifying position along the polymer chain, and i denotes the identity of the block along the contour length of the chain. Hence,

$$i = \begin{cases} A, & s < f_c \\ B, & s > f_c \end{cases} \tag{3.5}$$

The density fields are calculated as

$$\frac{\phi_A(\mathbf{r})}{N} = \sum_c \frac{\varphi_c}{N_c Q_c} \int_0^{f_c} \mathrm{d}s q_c(\mathbf{r},s) q_c^\dagger(\mathbf{r},s) \tag{3.6}$$

$$\frac{\phi_B(\mathbf{r})}{N} = \sum_c \frac{\varphi_c}{N_c Q_c} \int_{f_c}^{1} \mathrm{d}s q_c(\mathbf{r},s) q_c^\dagger(\mathbf{r},s) \tag{3.7}$$

The partition function of the single chain Q_c is

$$Q_c = \frac{1}{V}\int_V \mathrm{d}\mathbf{r} q_c(\mathbf{r},1) \tag{3.8}$$

The above set of equations [Equations 3.1-3.8] is solved selfconsistently using the pseudo-spectral method and the code developed by Morse and co-workers[79]. The ω fields are initially guessed and expanded in a symmetry-adapted basis function based on the morphology for which the free energy is to be calculated. The equations are then solved iteratively until convergence. Finally, the free energy F is evaluated as

$$\frac{F}{\rho k T} = \sum_c \left(\frac{\varphi_c}{N_c}\left[\ln\left(\frac{\varphi_c}{Q_c}\right) - 1 \right] \right) + \frac{1}{V}\int \mathrm{d}\mathbf{r} \left[\phi_A(\mathbf{r})\phi_B(\mathbf{r})\chi N - \sum_{i=A,B} \omega_i \phi_i(\mathbf{r}) \right] \tag{3.9}$$

The equations are solved in dimensionless units. Different Kuhn lengths are used for the two monomers, and the results depend on the variables χ, N_c, f_c and the blend composition φ_c.

3.2.2 Dissipative Particle Dynamics

Particle-based simulations account for density and composition fluctuations in the system whose effect is neglected in SCFT. Furthermore, they readily allow the analysis of spontaneously formed network phases lacking long-range order. Dissipative particle dynamics (DPD) has been introduced[45] as a coarse-graining approach to study mesoscale phenomena at longer time and length scales than those allowed by conventional molecular dynamics. To achieve this, the potential of interaction between particles is modified and coupled with a thermostat that consists of dissipative and random forces. It has been applied successfully[37, 53] to model microphase assembly of copolymer systems. Each macromolecule is modeled as a chain of beads (particles) linked by harmonic springs with the spring force given by $\mathbf{F}_{ij}^{S} = -k^{S}\mathbf{r}_{ij}$, where bead i is connected to bead j and spring constant $k^{S} = 4$ in our calculations. The interparticle interaction force between beads is given by

$$\mathbf{F}_{ij}^{C} = \begin{cases} a_{ij}(1 - |\mathbf{r}_{ij}|), & |\mathbf{r}_{ij}| < 1 \\ 0, & |\mathbf{r}_{ij}| > 1 \end{cases} \tag{3.10}$$

whose range also defines the effective "bead diameter" and the unit length used to reduce all lengths reported hereafter. It should be noted that we did not incorporate bead size asymmetry in this model, and the mass, length and time scales are all set to unity. To model the differing chemical interactions between monomers of different types, the coefficient a_{ij} is defined as

$$a_{ij} = \begin{cases} 25, & i = j \\ 25 + 3.27\chi, & i \neq j \end{cases} \tag{3.11}$$

where χ is the Flory-Huggins parameter. The equations of motion are integrated using a modified velocity Verlet scheme[38]. The Lowe-Andersen thermostat[62] is

used to maintain the reduced temperature fixed at unity. It acts on the relative velocity along the particles' center of masses and is designed to conserve their momentum. The overall density of the beads in the simulation box is exactly $\rho = 3$ and all simulations are carried out in the canonical (constant density, composition, and temperature) ensemble.

For each blend composition, simulations were carried out in cubic boxes for two million iterations with time step $\delta t = 0.05$; i.e., a duration of 10^5 units in dimensionless time. We only explored cubic boxes because our key interest was in identifying bicontinuous or cocontinuous phases with cubic symmetry. The range of box sizes studied was chosen taking into account that the shorter chains act as a cosurfactant and thus lower the thickness of the minority block domain resulting in smaller unit cells than those used for the pure DBC with the longer chains. Accordingly, our simulation box sizes "L_{box}" ranged from $L_{box} = 10 - 25$. The box size is critical because it artificially imposes a periodic length scale to the system. Cubic bicontinuous and cocontinuous phases are most affected since, e.g., for the gyroid morphology, we have to accommodate an integral number of unit cells (typically just one) in the box. This effect is milder for other phases but even for hexagonal cylinders, the tubes tend to align along the [111] direction of the simulation box. To probe the G phase at multiple box sizes, we used the final configuration obtained from simulations where it formed spontaneously and expanded or contracted the box with appropriate chain insertions and deletions to match both the overall density of $\rho = 3$ and the volume fraction of the blend. For preparing such initial configurations, an ad-hoc Monte Carlo scheme was used wherein the pressure was either reduced (to zero) for volume expansions or increased to large values (80 here) for contractions, while chain insertions/deletions, and relaxation moves were performed concurrently.

After the compression/expansion run, the configurations are further equilibrated using DPD for 2×10^6 time steps at $\delta t = 0.05$, after which the pressure (and compressibility factor) is calculated at a finer time step of $\delta t = 0.01$. Five configurations from this run are used as starting points for separate MC-EXE runs as described below.

3.2.3 Calculation of free energies

Due to the multitude of box sizes studied using DPD and the morphologies obtained at each blend composition, a reliable estimate of the free energy is crucial to determine the stable phase. To calculate the free energy, we resort to Monte-Carlo simulations in an expanded ensemble[27] (MC-EXE). The potential model used for this system is the same one used for the DPD simulations.

To calculate the chemical potential, chains are gradually added/removed, in λ_m stages, i.e., one bead at a time in this work. The transitions between these stages ($\Delta = +1$ for insertion and $\Delta = -1$ for deletion) are accepted according to the Metropolis criterion

$$P_{acc} = \min\{1, \exp(\nu + \psi_{m+\Delta} - \psi_m)\} \tag{3.12}$$

where $\nu = -\Delta \ln W$, with W the Rosenbluth weight[31]. ψ_m are the biasing weights that are iteratively adjusted to attain a uniform sampling of all intermediate λ_m stages (i.e., a "flat histogram" approach). From the simulation, the free energy difference between successive stages is calculated using Bennett's acceptance ratio method[5]

$$\beta \Delta A_{m,m+1} = C - \ln \frac{l_{m+1,m}}{l_{m,m+1}} \tag{3.13}$$

where $l_{m,m+1}$ is the number of transitions from λ_m to λ_{m+1} and C is calculated from

$$\sum_m \frac{1}{1+\exp(\nu_{m\to m+1}-C)} = \sum_{m+1} \frac{1}{1+\exp(\nu_{m+1\to m}-C)} \tag{3.14}$$

The excess chemical potential for the whole chain (each species) is simply the cumulative free energy change over these stages, i.e., $\mu^{ex} = \sum_{m=0}^{N-1} \Delta A_{m,m+1}$. Finally, the excess free energy of the system is calculated by

$$\beta a^{ex} = \beta \sum_c y_c \mu^{ex} - (Z-1) \tag{3.15}$$

$$= \beta \sum_c \left(y_c \sum_{m=0}^{N-1} \Delta A_{m,m+1} \right) - (Z-1) \tag{3.16}$$

where y_c is mole fraction of component c, $Z = \beta PV/(\sum_c M_c)$ is the compressibility factor, M_c is the number of chains of component c, and $\beta = 1/kT$ (with $k =$ Boltzmanns constant). Error bars in the free energy estimates (for each set of blend compositions and system sizes) were obtained as the standard deviation of the values obtained from 5 independent simulations.

The free energies from this MC-EXE method (Equation 3.16) are expected to be suitable for the purpose of discerning the stability of different morphologies obtained at the same thermodynamic conditions. It should be pointed out, however, that for morphologies with three dimensional symmetry, like the bicontinuous phases, equation 3.16 ignores a correction needed to account for the fact that our simulations do not allow fluctuations in the number of unit cells (of the given morphology) in the system[111, 78]. Such a correction is especially important to identify the optimal system size at which a phase attains its minimum free energy. In such cases, an alternative "thermodynamic integration" method "TI" is preferable to simulate free energies. With TI, we can estimate the free energy difference (of a given phase) between the desired χN and the disordered phase at $\chi N = 0$ by

Component	N	f
as	2.866	0.185
s1	1	0.485
s2	0.79	0.455
s3	0.652	0.490

Table 3.1: Chain lengths used in the SCFT study. N is the "relative" degree of polymerization and f is the fraction of monomer A in each component.

constructing a 3-step reversible path from the initial and final states[80] consisting of: (i) applying an ordering field of the desired morphology at $\chi N = 0$ to drive self-assembly, (ii) increasing the value of χN to the final state, and (iii) switching off the ordering field at the final value of χN. A detailed account of how this TI method is implemented (e.g., to create the ordering field) and its application to different systems is the subject of a forthcoming publication. In this paper, we will just use it for a representative case to validate the conclusions drawn from the MC-EXE results.

3.3 Results

3.3.1 SCFT

We used SCFT in a canonical ensemble to predict the phase behavior of three binary blends in the composition range $0 \leq \varphi_s \leq 1$, for varying lengths of the symmetric chains. Here, φ_s is the volume fraction of the symmetric diblock copolymer chains in the mixture. It is related to the overall volume fraction of the minority block or monomer type A (φ_A) by the relation $\varphi_A = f_{as}(1-\varphi_s)+f_s\varphi_s$. Asymmetric Kuhn lengths were used, namely, $b_A : b_B = 1{:}1.11$, to mimic PS-b-PI. Three lengths of the shorter diblock were studied, which are denoted in order of decreasing size

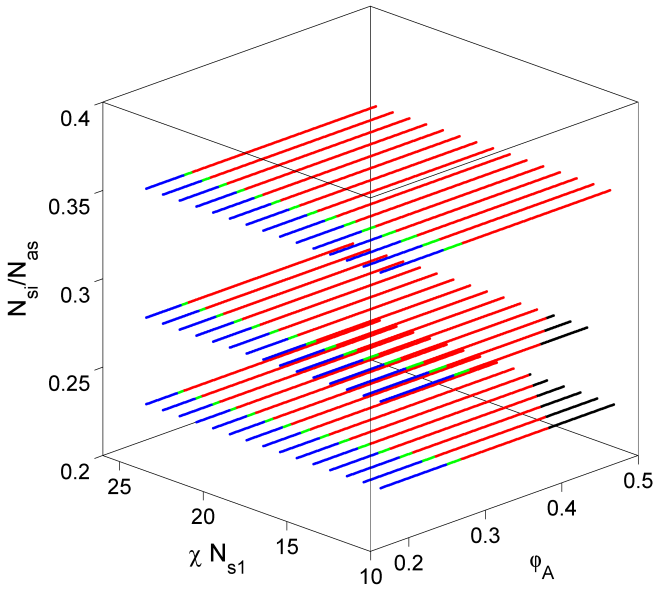

Figure 3.1: Phase diagram from SCFT for blends *s1* (top), *s2* (middle), and *s3* (bottom) as described in Table 3.1. Blue = cylinders, green = gyroid, red = lamellar, black = disordered.

as s_1, s_2, and s_3. Note that since SCFT describes the behavior of chains in the infinitely long chain length limit, only relative chain length values are meaningful and we choose as reference $N_{s1} = 1$. Details of the system are found in Table 3.1 and the results are summarized in Figure 3.1. The phase diagram was constructed for χN_{s1} ranging from 11 to 25 in steps of unity. This enables us to study the blends in the same temperature range, with the *as-s1* blend entirely above the ODT ($\chi N_{s1} = \chi > \chi N_{ODT}$). As φ_A is increased, a progression of phases from C to G to L was observed for each of the blends. At low values of χN_{s1}, the blends of *s2* and *s3* with large amounts of the symmetric component were in the disordered state as is expected due to the proximity of the ODT for the pure symmetric DBC. Other candidate phases included in the study were the double diamond and body-centered-cubic micellar phases, but these were found to be always unstable.

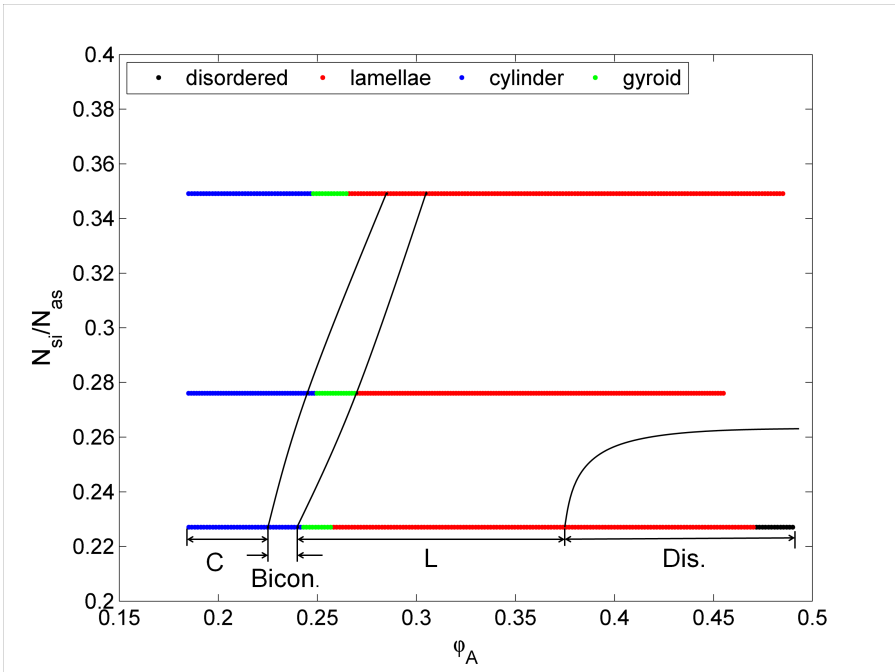

Figure 3.2: Phase diagram at constant temperature ($\chi N_{s1} = 15$). The solid black lines mark the phase boundaries obtained by Court and Hashimoto [16].

The predicted sequence of stable phases on increasing φ_A; i.e., C $\rightarrow$ Bicontinuous $\rightarrow$ L and the L $\rightarrow$ Disorder (for small N_{si}/N_{as}) is consistent with the experimental observations of Hashimoto and co-workers[16]. Note also that in their experiments no macrophase separation was observed for any of the blends under study. Figure 3.2 compares all three mixtures at the same value of χ, and the experimental data by Court and Hashimoto at room temperature. The unidentified bicontinuous (Bicon.) phase in the experiments occurs around regions in the theoretical phase space where the gyroid is stable. In the experiments, the pure asymmetric polymer yielded a BCC sphere microstructure, which we did not observe in our SCFT calculations, although the free energy of the spheres was only marginally higher than that of hexagonal cylinders. For both theory and experiment, the *as-s2* blend has the widest range of stability of gyroid which may be attributed to the highest degree of asymmetry ($f = 0.455$) in the short chain.

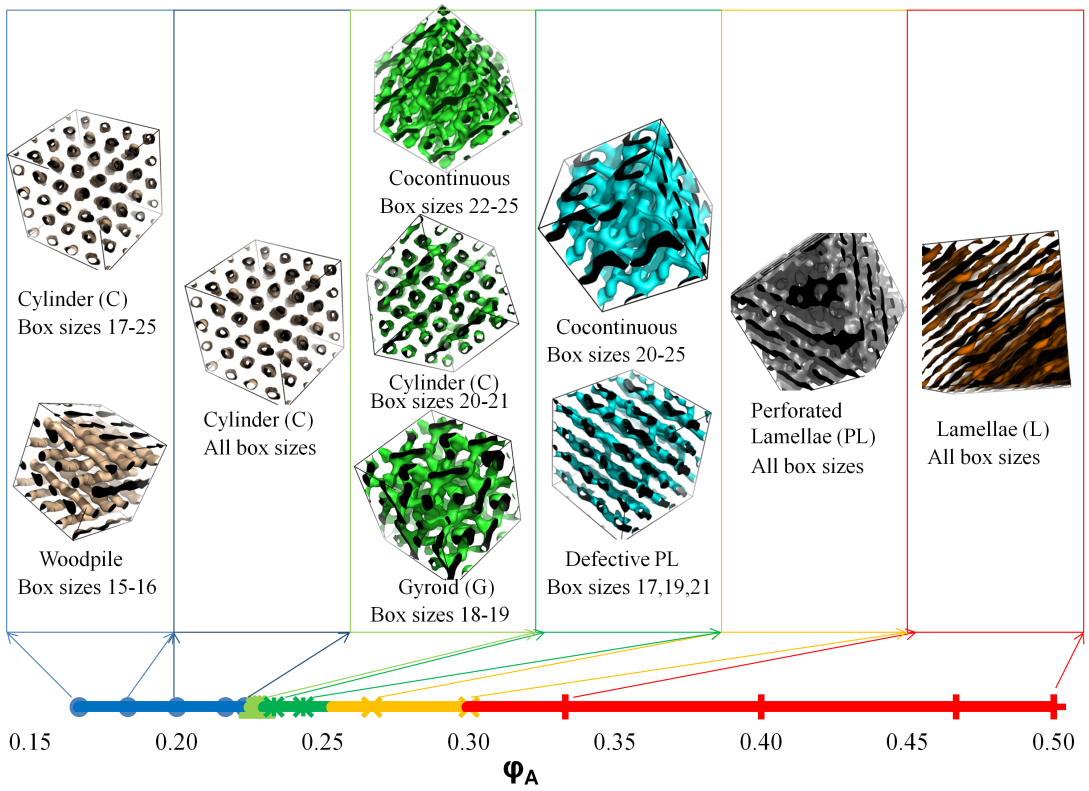

Figure 3.3: Morpohlogies obtained at $\chi N = 35$ for various blend compositions φ_A and at various box lengths. For clarity, only the interfaces between block domains are shown.

However, there is disagreement between the theory and experiments in the location of the φ_A window where the bicontinuous phase is stable. In experiment, there is a significant shift towards higher volume fractions whereas in the theory there is hardly any shift at all (for all the values of χ explored). The reason for such qualitative difference is unclear, although it may be partially attributed to differences between the gyroid morphology of SCFT and the unresolved experimental bicontinuous morphologies.

3.3.2 DPD

We performed DPD simulations for only one of the systems studied with SCFT, the one with the longest symmetric diblocks, *s1*. This choice was set by the requirement of a moderate chain length for the long asymmetric DBC to keep the system size computationally tractable; accordingly, a too-short symmetric DBC would have entailed the use of unrealistically few beads in that chain. For the asymmetric chain, the number of beads per chain is $N_{as} = 18$ and the fraction of beads of type A is $f_{as} = 1/6$. For the symmetric chain, the chain length is $N_s = 6$ and the fraction of A-type monomers is $f_s = 0.5$. This results in both types of chains having the same number of A-type beads (=3). The systems were simulated at a value of $\chi N_s = 35$, hereafter simply denoted as χN, and for different values of blend composition φ_s, which is the volume fraction of the short, symmetric chains in the blend. φ_s is varied from 0 to 1, so that the overall volume fraction of A, $f_A = 1/6 + \varphi_s/3$ varies from $f_{as} = 1/6$ to $f_s = 1/2$.

The double gyroid (G) and cylinder (C) phases were formed spontaneously at relatively low values of φ_s. Other spontaneous phases that were observed during the course of these simulations were the simple cubic woodpile (W) phase[115], perforated lamellar (PL) phase, lamellar phase (L), and various cocontinuous networks whose symmetry could not be ascertained. Snapshots of spontaneously appearing microphases are shown in Figure 3.3.

At $\varphi_A = 0.167$ ($\varphi_s = 0$), we observe hexagonally arranged cylinders (C) for moderate values of box size ($17 \leq L_{box} \leq 25$). For small box sizes ($15 \leq L_{box} \leq 16$), we observe a 2-layer woodpile phase (W). To our knowledge, this phase has never been reported in simulations (a four-layer woodpile structure was recently reported in experiments[115]). In this phase, cylinders of alternating layers point

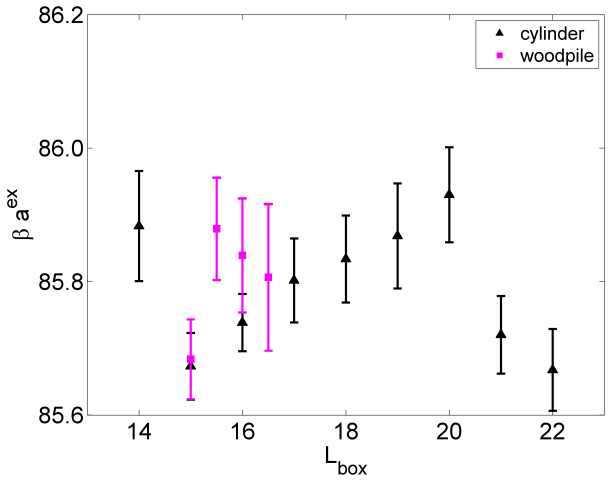

Figure 3.4: Variation of free energies of the woodpile and cylinder phases with box size at blend composition $\varphi_A = 0.1833$. The error bars give the standard deviation of the data.

in perpendicular directions with the two layers repeating periodically.

Figure 3.4 shows the calculated free energies for the woodpile and C phases for a blend composition of $\varphi_A = 0.1833$. Although the stable phase could not be resolved from this plot given the proximity of free energy minima and the size of the error bars, finite size effects are likely more significant for the woodpile phase which only occurs for small boxes. For $L_{box} = 15$ at which the woodpile phase has the lowest free energy, it remains stable for over 10 million steps. Once formed, there are likely both a considerable kinetic barrier and a stabilizing finite size effect (from the tubes connecting through the box periodic boundaries) to allow the reorientation of tubes into a hexagonally arranged C structure. On doubling the box size, the woodpile phase undergoes a transition to the C phase in fewer than one million steps, further supporting the idea that the woodpile phase is metastable with respect to the cylinder phase.

The woodpile phase continued to appear at smaller box sizes for values of φ_A up to 0.2167 ($\varphi_s = 0.15$). For the rest of the box sizes only cylindrical morphologies

formed, albeit with the appearance of more defects as φ_A increased. These defects included necking of cylinder tubes and the formation of loops, branched points (nodes), and in some cases, undulating tubes.

For $\varphi_A = 0.2267$ ($\varphi_s = 0.18$), we first observed a G morphology that emerged spontaneously for $L_{box} = 19$. In this vicinity, we ran simulations at finer intervals in φ_A. The G phase appeared spontaneously for $\varphi_A = 0.2250, 0.2267, 0.2283$, and 0.2300 in competition with both the C phase and cocontinuous network structures. A discussion of the free energy results and stability of these phases is described in detail in section 3.3.3.

Between $\varphi_A = 0.2333$ ($\varphi_s = 0.20$) and $\varphi_A = 0.2433$ ($\varphi_s = 0.23$) no clear symmetry of the morphologies could be identified for any box size. A dominating feature of these morphologies was the prevalence of single networked structures, instead of the two interweaving networks characteristic of bicontinuous phases. Since both the majority and minority phases were continuous, these network phases were termed cocontinuous. Upon increasing φ_A to 0.2667 ($\varphi_s = 0.3$), we observed perforated lamellar structures (PL) for most of the box sizes investigated. It should be noted that these perforations were not always hexagonally arranged but were more of a random nature. At $\varphi_A = 0.3$ ($\varphi_s = 0.4$), the PL phase was observed for most box sizes, with the L phase appearing for smaller box sizes. Up to $\varphi_A = 0.4$ ($\varphi_s = 0.7$), the L phase competed with the PL phase. However, for $\varphi_A = 0.4$, the perforations were tiny and dynamic, appearing and disappearing throughout the lamellae. We therefore concluded that the phase observed is indeed the L phase and the perforations are just a transient feature of the morphology. Upon increasing φ_A, the perforations disappeared entirely and we get a perfect L phase.

To map out in more detail the conditions at which the G phase emerges, further

χN	φ_A				
	0.2233	0.2250	0.2267	0.2283	0.2300
30	def C	def C/def PL	def C/def PL	def C/def PL	def C
35	C	G, C, Cocon.	G, C, Cocon.	G, C, Cocon.	G, C, Cocon.
40	PL, C	G, C, Cocon.	G, C, Cocon.	PL, C, Cocon.	PL, C, Cocon.
45	C	Cocon.	PL, C	–	def PL

Table 3.2: Morphologies obtained using DPD by varying χN for blend compositions $0.2333 \leq \varphi_A \leq 0.2300$. "Def" refers to morphologies with defects, C = cylinders, G = gyroid, PL = perforated lamellae, and Cocon. = cocontinuous phase.

simulations were run by varying χN in steps of 5 in the vicinity of 35. A summary of our findings is presented in Table 3.2. For $\chi N = 30$ only the PL and C phases appear spontaneously. For $\chi N = 40$, we again observe the G phase, but in a narrower window than for $\chi N = 35$, and for larger values of χN values, the G phase altogether disappears.

It should be noted that for the model adopted in the DPD simulations, the order-disorder transition (ODT) occurs at $\chi N_{ODT} \sim 28$ and hence our choice of χN would put the *as-s2* blend near the vicinity of the ODT and the *as-s3* blend below the ODT, which is qualitatively similar to the experimental conditions. At $\chi N = 35$, $(\chi N - \chi N_{ODT})/\chi N_{ODT} = 0.25$, which would correspond to a χN of 13.125 for SCFT (a value included in the results of Figure 3.1). Note that differences between the simulated and theoretical phase diagrams are caused not only by the difficulties in exactly mapping model parameters but more importantly by the effect of local fluctuations and finite chain length which are not accounted for in the theory.

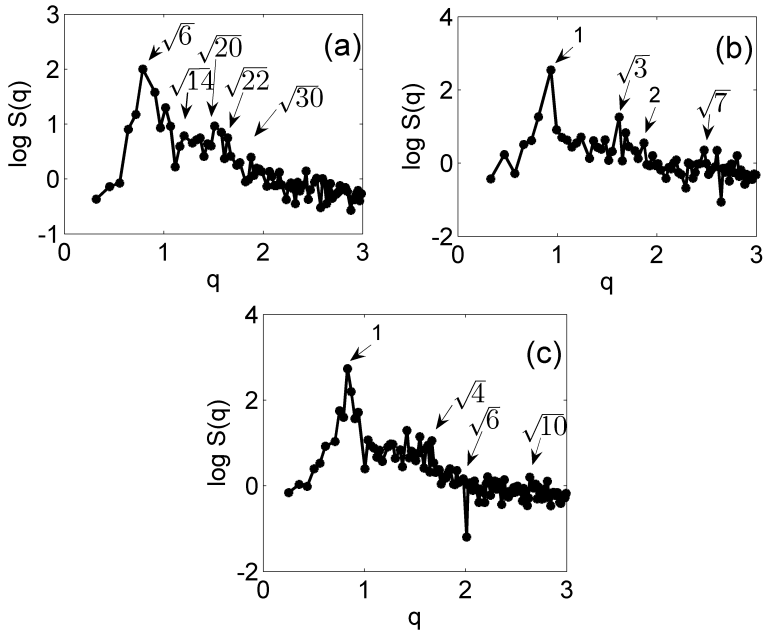

Figure 3.5: Structure factor of (a) gyroid for $L_{box} = 19.5$, $\varphi_A = 0.2250$, (b) cylinders for $L_{box} = 19$, $\varphi_A = 0.2250$, and (c) cocontinuous phase for $L_{box} = 25$, $\varphi_A = 0.2267$.

3.3.3 Stability of the G phase

The G phase appeared spontaneously for certain box lengths at compositions between $\varphi_A = 0.2250$ and $\varphi_A = 0.2300$. At the same volume fractions, we also found the C phase at slightly larger box sizes, and cocontinuous morphologies at even larger box sizes. The cylinder morphologies were not all defect-free, with some necking between some tubes. For some box sizes, the defects occurred throughout the tubes and led to a cocontinuous network. To classify the observed morphologies, the structure factor of block A was calculated from[99]:

$$S(\mathbf{q}) = \frac{\left(\sum_j \cos(\mathbf{q}\cdot\mathbf{r}_j)\right)^2 + \left(\sum_j \sin(\mathbf{q}\cdot\mathbf{r}_j)\right)^2}{M} \tag{3.17}$$

where $\mathbf{r}_j$ is the position vector for beads of the minority block and M is the total number of all beads in the system. For the morphologies labeled as the G phase,

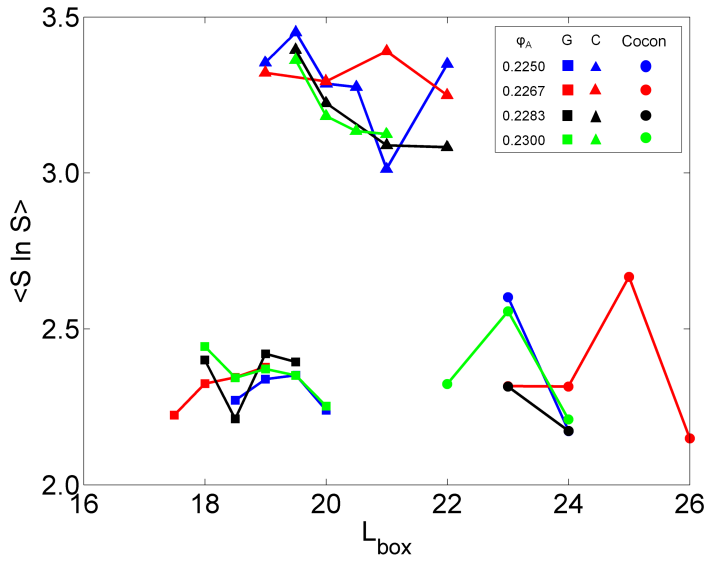

Figure 3.6: Order parameter $\langle S \ln S \rangle$ as a function of box size for the gyroid, cylinders and cocontinuous morphologies for blend compostiions $0.2250 \leq \varphi_A \leq 0.2300$; $\chi N = 35$.

the peaks in $S(\mathbf{q})$ occurred at positions consistent with the ratios $\sqrt{6} : \sqrt{8} : \sqrt{14} : \sqrt{16} : \sqrt{20} : \sqrt{22} : \sqrt{24} : \sqrt{26} : \sqrt{30} : \sqrt{32} : \sqrt{38} : \sqrt{42}$[24], although not all of them were always present prominently. An example is plotted in Figure 3.5a for a snapshot taken at $\varphi_A = 0.2250$. For the C phase, we get peaks consistent with the ratios $\sqrt{1} : \sqrt{3} : \sqrt{4} : \sqrt{7}$, indicating a hexagonal ordering (Figure 3.5b). Figure 3.5c shows peaks of a cocontinuous phase in the ratios $\sqrt{1} : \sqrt{4} : \sqrt{6} : \sqrt{10}$, which are inconsistent with any known cubic bicontinuous phase; these phases are termed as disordered cocontinuous because often the square of the peak wavelengths is not in integral ratios.

Visual inspection of snapshots and structure factors proved inadequate to characterize a particular type of order in cocontinuous phases; e.g., to determine whether it is a highly defective C phase or not. To try to characterize the order in these cocontinuous phases, we used the order parameter given by $\langle S \ln S \rangle = \int \mathrm{d}\mathbf{q} S(\mathbf{q}) \ln S(\mathbf{q})$, which measures the amount of order in the system[37].

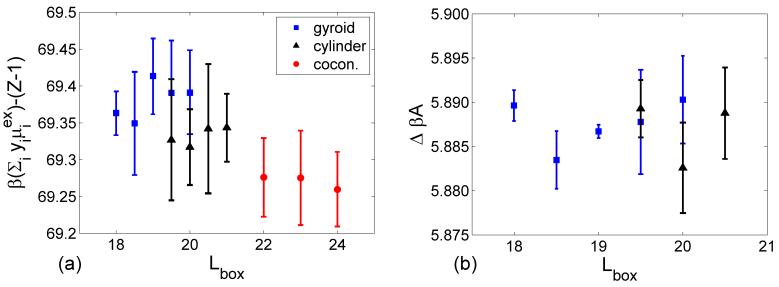

Figure 3.7: Variation of free enenrgy with box size for different morphologies for blend composition $\varphi_A = 0.2300$ and $\chi N = 35$: (a) from MC-EXE method and (b) from TI method (showing free-energy diference relative to that at $\chi N = 0$).

This order parameter is therefore akin to the negative of an "entropy" in the structure factor. In general, it is expected to be highest for the lamellar phases, somewhat lower for hexagonal cylinders and perforated lamellae, even lower for bicontinuous and cocontinuous phases (as the number of peaks contributing to the structure increases), and is zero for the disordered phase. The results are plotted in Figure 3.6 for $\chi N = 35$. It is seen that the G phases have much lower values than the C phases, whereas some of the cocontinuous morphologies are more network-like while others have some cylinder-like character. This order parameter was used to distinguish perforated lamellae from cocontinuous phases for blend compositions in the $0.2333 \leq \varphi_A \leq 0.2433$ range.

For the blend composition $\varphi_A = 0.2300$, the simulated free energy via MC-EXE is plotted against simulation box size in Figure 3.7a. Changes in free energy with box size are most pronounced in the G phase (observed in other blend compositions as well). In contrast, the average free energies of the cocontinuous phases seem the least sensitive to box size. Figure 3.7b shows the free energy relative to $\chi N = 0$ for the gyroid and cylinder phases using the TI method. Note that the TI results exhibit error bars (O(0.01)) that are much smaller than those for theMC-EXE method (O(0.1)), and that (at least in this case) the MC-EXE and TI results are

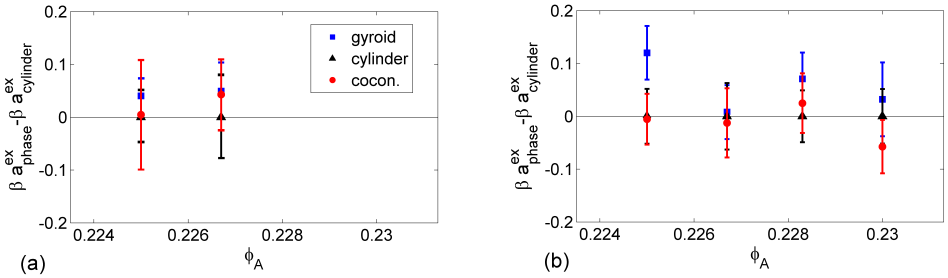

Figure 3.8: Free energies of the gyroid and cocontinuous phases relative to that of the cylinder phase for various blends at (a) $\chi N = 40$, (b) $\chi N = 35$.

consistent in that: (i) the free energies of the cylinder and gyroid phase are within error bars of each other and (ii) the free energy minimum for a given phase occurs at the same box size (L_{box}). In view of this and that the TI method would be difficult to apply to get free energies for the disordered cocontinuous phases, we will henceforth only discuss results obtained via the MCEXE method.

For a given set of conditions (χN and blend composition), the stable phase is the one which has the lowest free energy among all box sizes. Figure 3.8 gives the lowest free energy of each phase relative to that of the cylinder phase for the range of φ_A studied. One can see that the free energies for the three competing phases are within error bars of each other for all blend compositions, and variations in simulation initial conditions might lead to the appearance of one phase or another (even if only as a long-lived metastable state). Furthermore, with free energies so close together, multi-phase coexistence is a possibility (a scenario that could not be directly explored due to the small box sizes used for computational expediency). It is conjectured that similar metastability issues and partial phase transformations may have contributed to the difficulty in identifying the "bicontinuous" structure observed in the experiments of Court and Hashimoto[16].

We also examined the effect of box size on the contributors to the free energy

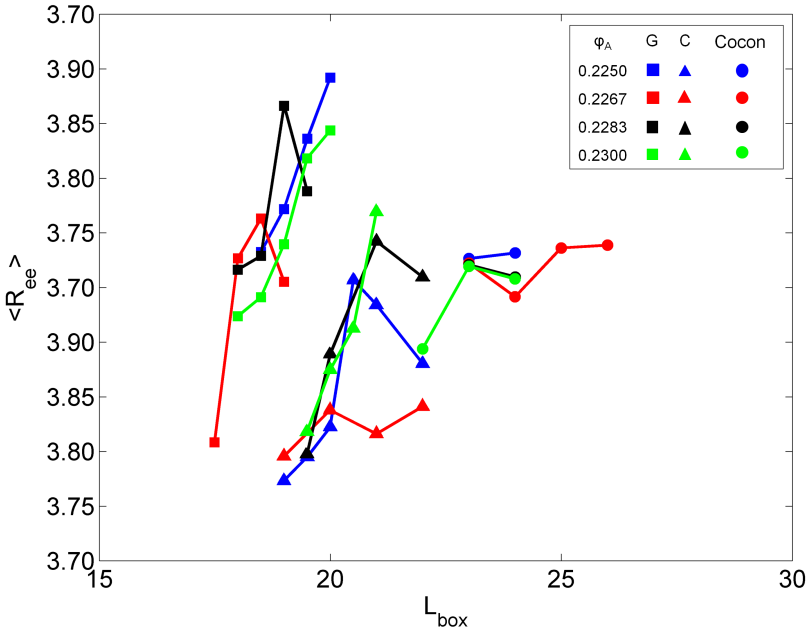

Figure 3.9: End-to-end distances for B block of asymmetric chains *as*.

(as per Equation 3.16). The compressibility factor (Z) and therefore the pressure tend to decrease slightly upon increasing box size, suggesting that larger box sizes may help relieving some mechanical stress associated with the orientation or compatibility of the morphological patterns in the simulation box. In contrast, the chemical potential for each component does not follow any particular trend among all blend compositions studied (results not shown), thus indicating a non-trivial dependence of the free energy of such contributors. We also calculated the end-to-end distances for both the asymmetric and symmetric chains in all morphologies. For the G phase, as box size increases, the end-to-end distance of the asymmetric chains as increases; this is true for the overall chain and for the individual A and B blocks within as. These data are shown in Figure 3.9 for $\varphi_A = 0.2300$. On the other hand, the end-to-end distances of the symmetric chains *s1* of all morphologies lie within the same range of values ($\sim$1.295 – 1.315 data not shown). This is expected, as shorter chains are known to act as stiffer entropic springs. It is

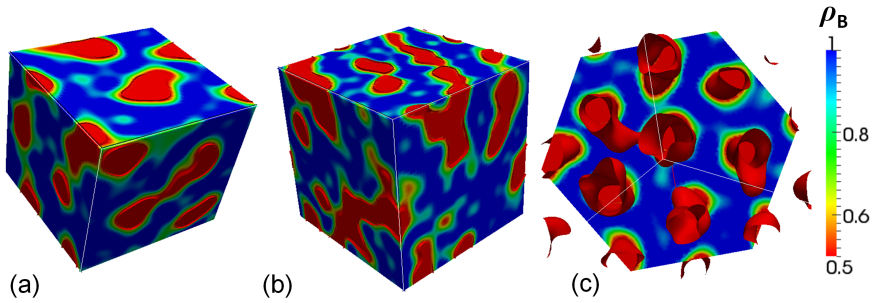

Figure 3.10: Local density of the majority domain. Red portions indicate regions of the minority domain. Green (low density) pockets in the 'bulk' of blue domain evidence packing frustration. (a) Gyroid phase for $L_{box} = 19.5$, $\varphi_A = 0.2250$, (b) cocontinuous phase for $L_{box} = 25$, $\varphi_A = 0.2267$, and (c) cylinder phase for $L_{box} = 19$, $\varphi_A = 0.2250$.

then the extension of the longer (15-bead) B blocks in the *as* component that is expected to have a larger contribution to conformational entropy in the system and serve as a probe of the degree of confinement in the B-rich domain. The fact that for all morphologies the *as*-B block end-to-end distance tends to decrease upon reducing the box size reflects a concomitant decrease in the B-domain "thickness" that accentuates the confinement of the enclosed chains. However, this trend need not be monotonous (e.g., if the domain geometry does not scale affinely with L_{box}) and is strongly dependent on morphology (e.g., chain extension in the disordered cocontinuous phases seems the least sensitive to box size).

Figure 3.9 also shows that the C phase is the one that achieves the lowest level of chain stretching (for a suitable choice of box size). Because chain stretching is a hallmark of packing frustration, these observations suggest that one should also observe regions of lower density in the centers of the B (majority) block domains which the *as*-B block chains are trying to fill (driving their over extension). This expectation is verified in Figure 3.10 which shows the spatial variation of the B-block density and where one can see lower density regions (green) in the center

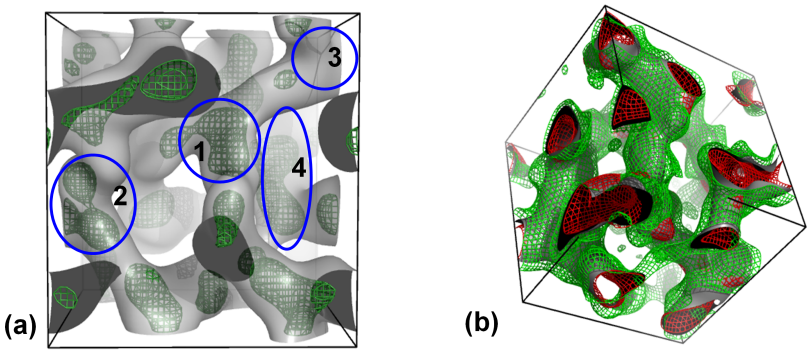

Figure 3.11: Isosurfaces of A-block fraction = 0.5 for the gyroid phase with L_{box} = 19.5, $\varphi_A = 0.2250$: grey surface represents overall A-monomers in the blend, green mesh for symmetric chains, and red mesh for asymmetric chains. (a) Density calculated as the *number of symmetric chain A beads over total number of beads*. Points 1 and 2 show nodes that the symmetric chains occupy, 3 is a node which such chains do not occupy, and 4 refers to a tube that such chains occupy. (b) Density calculated as *number of A beads of all chains over total number of beads*.

of the B-domain. Indeed, one also sees that the low B-density pockets increase going from the C to the G and to the cocontinuous phases, in correspondence to their average as-chain end-to-end distances under those conditions. While packing frustration is the result of morphology-specific competition of enthalpic interactions (trying to minimize the interfacial surface area) and entropic interactions that favor uniform mixing and density, it is likely that the disparity in the B-block lengths enhances packing frustration in the B domain. Note that since the SCFT we used before (in Section 3.3.1) assumes uniform domain densities and Gaussian chain behavior, it is not suitable to capture the chain stretching behavior and the local lower density regions as described in Figures 3.9 and 3.10.

Finally, we examined the spatial distribution of chains in the A (minority) domain and around the block interfaces to detect any signs of morphology-dependent packing frustration or local segregation. No regions of lower density are detectable in the A domains (results not shown), perhaps a consequence of the short A blocks and the thin tubes or struts involved. The structure factors of each of the com-

ponents indicate that there is no preferential arrangement towards nodes or tubes for the longer chains (results not shown) and that the interface is shared evenly between the two components (see Figure 3.11a). However, the A-B junctions of the longer, asymmetric chains are more confined within the minority domain while the A-B junction of the shorter, symmetric chains occupies the domain periphery in the G (see Figure 3.11b), C, and cocontinuous phases. In a sense, two parallel interfaces emerge having the same morphology separated by a small distance (equal or less than one bead diameter), with the shorter chains occupying the one with the lower curvature. These results are surprising in that one may have expected the outer interface to be formed by the asymmetric chains since these are being "pulled" toward the centers of the B domains (i.e., the packing frustration of their B-blocks).We conjecture that it is the shorter symmetric chains that form the outer interface because in this way (i) they are less confined at the interface and hence lose less translational and mixing entropy and (ii) the *packing frustration in the narrow A domains* is alleviated. Interface "shifting" could then be seen as an alternative strategy to fill the A-domain uniformly when chain stretching is too demanding and minimal (as with the short A-blocks used here). As blend composition is increased and the curvature of the A-B interface decreases, we find that these two interfaces almost coincide and for the perforated lamellae, these are essentially identical.

3.4 Conclusions

In this work, we have shown that for a binary blend of DBCs containing a longer cylinder-forming asymmetric DBC and a shorter lamellae-forming symmetric DBC, the phase diagram reveals the progression from a cylinder to a lamellar phase

with an intermediate morphology. Although SCFT calculations predict that the gyroid phase is stable over a narrow composition range of the blend, particle-based simulations indicate that in such a region the free energy of the gyroid, cylinder, and disordered cocontinuous phases are within error bars of each other, even for multiple values of χ. Further examination of the structure factor and chain spatial distributions show that both types of DBCs occupy the interface evenly; e.g., they do not preferentially reside in the nodes or the struts of the gyroid phase. However, the shorter chains penetrate less and the longer chains penetrate more into the minority domain, creating a "double" interface that likely relieves packing frustration in the A-rich phase but contributes to packing frustration in the B-rich phase. Such chain stretching and interface shifting can be seen as mechanisms by which the system can realize a given morphology minimizing the loss in chain conformational entropy (by extending mostly the more forgiving longer chains) and in translational entropy (by reducing the confinement of the shorter chains). In the future, it will be interesting to explore the feasibility of using an asymmetric DBC additive but of a composition chosen to alleviate packing frustration in both of the domains; depending on the length and composition of such an additive, it could stabilize a gyroid phase over a broader range of conditions and at overall A-block volume fractions that may be lower or higher than those where it is observed in pure DBCs[95].

An intriguing finding in this work is the appearance of a metastable woodpile phase. Although its free energy was found to be within error bars of the cylindrical phase, the woodpile phase transforms to a cylinder phase when the box size is doubled in each dimension. In spite of this, the fact that the woodpile phase appears spontaneously seems to indicate that its stability could be achieved not far from the composition space explored in this work. Some of our ongoing work entails

precisely exploring DBC blends and conditions where the woodpile phase becomes stable. A related but broader area of interest relates to understanding how the preparation and processing conditions (e.g., via the use of transient external forces and flows) could bias the system to be kinetically trapped in a desired metastable phase among a number of competing phases having similar free energies (e.g., to trap the woodpile phase at compositions where it competes with a stable C phase, or to form the G phase at conditions where it competes with the C and cocontinuous phases).

Finite size effects associated with small box sizes constitute one of the important shortcomings of particle-based simulations. In principle, for periodic ordered morphologies one should consider using ensembles where the number of unit cells is increased until attaining a limiting convergent behavior. Ongoing work focuses on determining the true unit cell size of the morphologies by indirect estimation of the "chemical potential" associated with number of unit cells[111] from calculations of free energy using thermodynamic integration[78] and those of chemical potentials and compressibility factors using the methods described in this paper. In the case of ordered, orthorhombic cocontinuous phases, one should consider varying not only the system size but also the asymmetry of the box sides to attain the optimal unit cell shape (which need not be the same as the theoretical one). Constant pressure simulations, as opposed to constant density simulations, could also help discriminate the most stable phase at conditions where competing phases may lead to non-negligible differences in density. Clearly, such undertakings would entail large investments of computational resources and advocate for alternative hybrid approaches, like the one adopted here, where the results and strengths of SCFT and particle-based simulations are combined to probe both large system-size behavior (via SCFT) and crucial details of the local structure of selected phases

(via DPD).

3.5 Acknowledgements

This work was supported by Grant CBET 0756248 from the National Science Foundation. This publication is also based on work supported in part by Award No. KUS-C1-018-02, made by King Abdullah University of Science and Technology (KAUST). F.J.M.V. was supported by the ERC (Advanced Grant Agreement No. 227758). We are thankful to Professor David Morse from University of Minnesota for the code for implementing SCFT.

CHAPTER 4

SIMULATION OF FREE-ENERGIES OF BICONTINUOUS PHASES FOR BLENDS OF DIBLOCK COPOLYMER AND SELECTIVE HOMOPOLYMER

4.1 Introduction

In block copolymer and surfactant systems, bicontinuous phases like the gyroid (G), the double diamond (D), the plumbers nightmare (P), and Neovius (N) phase are characterized by a periodic cell that has 3D symmetry and where the minority component forms two networks embedded in a continuous matrix of the majority component that interweave but never intersect each other. These networks are made of struts and nodes where the number of struts that connect into a node are 3,4, 6, and 8 for the G, D, P, and N phases, respectively. The field of bicontinuous network synthesis has become an area of prolific research with application-driven goals. These range from photonic devices, solar cells, drug-delivery patches to complex coacervates. Several material properties directly depend on the underlying structure (e.g., optical, electrical, mechanical, transport, etc.)[21, 54, 59, 85, 120, 123, 126] and being able to synthesize a variety of morphologies using the same set of building blocks can provide great flexibility in designing new materials. Over the last two and a half decades, considerable success has been achieved in synthesizing a variety of morphologies using bottom-up approaches by self-assembly of block copolymer materials.

However, the assembly of bicontinuous morphologies from block copolymers continues to be a challenging task for several reasons. First, these phases are typically stable only in a narrow region of the phase diagram. The need to synthesize

molecules with very tight compositions and to operate at very specific conditions can be not only expensive but also limiting in terms of practicability and potential applications. Second, kinetic trapping, whose effects are enhanced near phase boundaries, may preclude their timely formation and long annealing times are often necessary in experiments to obtain bicontinuous structures. In the past, bicontinuous morphologies have been misidentified in several experimental studies[114, 39] and sometimes cannot be unambiguously identified when appearing as a mixed or partially transformed material[14, 15]. To circumvent these issues, incorporating additives to the block copolymers is a promising route to expand the stability region of these phases and to reduce kinetic traps by targeting conditions near the center of the stability regions. Given the different types of additives that can be used, theoretical and simulation studies are necessary to chart the associated phase diagrams which can be used to guide experiments towards the facile realization of any desirable bicontinuous phases.

The blend of an A-B type DBC with a homopolymer of type A provides a route to obtain multiple bicontinuous morphologies where we have two non-intersecting, interweaving networks of A-type material assembled within a matrix of the majority B[24, 28, 73, 23, 65, 66, 77, 76, 118]. The relevant design parameters for this bottom-up assembly are: (i) volume fraction of B in the DBC (fdbc), (ii) relative degree of polymerization of the homopolymer ($\alpha = N_{hom}/N_{dbc}$), and (iii) volume fraction of the added homopolymer (ϕ = volume of homopolymer/total volume of the blend). Our focus will be on the G forming volume fraction of DBCs ($f_{dbc} = 1/3$), since that is the only bicontinuous morphology stable for a pure DBC and has been shown to lead to progressively more complex bicontinuous phases as more homopolymer is added[65, 66].

Previous work[65, 66] focused extensively on values of $\alpha = 0.8$ and used both self-consistent field theory (SCFT) and particle-based simulations to predict conditions at which the three bicontinuous phases – the G, D and P phases would be stable. While SCFT provides a relatively expedite and reliable means to map out such phase diagrams, its reliance on mean-field approximations can make its predictions inaccurate at conditions where, e.g., density fluctuations or non-ideal chain conformations are important. Particle-based simulations, where polymers are modeled as chains of connected beads, are in principle free of the effects of mean-field assumptions and can be used to gain insights into the kinetic aspects of self-assembly but are computationally much more expensive. Accordingly, it is only feasible to conduct particle-based simulations of chains of relatively small degree of polymerization which introduces a discreteness to the polymer compositions and size ratios that are studied. We note, however, that the use of soft-bead potentials like that associated with Dissipative Particle Dynamics (DPD) to some extent circumvents the short-chain curse in that each soft bead is meant to represent the effective interaction potential of a short polymer (hence a 10-bead DPD chain could approximate a polymer with 100-1000 repeat units). Even so, each unit cell of a bicontinuous phase will typically contains several thousand chains and it becomes computationally prohibitive to simulate more than one unit cell.

Another key challenge that is especially formidable for particle-based models of bicontinuous phases is that their unit cell size is not known a-priori. This implies that the stability of the morphology is sensitive to the box size, and only for a box size commensurate with the natural unit cell size can one be guaranteed to attain optimal stability. In practice, upon varying the simulation box size, different morphologies may nucleate, and free energy calculations are required to ascertain the morphology that is thermodynamically stable. For one dimensional

or two dimensional morphologies, a small-to-moderate mismatch in unit cell size and simulation box size is naturally circumvented because the structure can rotate in space and align in a way that best fit the periodic box. For example, the hexagonally packed cylinders can point anywhere between the [111] direction and the [100] depending on box size. This is not the case for a bicontinuous phase whose three dimensional unit cell cannot rotate to accommodate slight mismatches in the size of the simulation box. Note that this issue is not addressed by box length search algorithms that look for equal pressure in all dimensions[97]. Also, we will only be concerned with a constant density ensemble, primarily because the soft DPD potential we adopted was developed for constant density simulations[37]. Also, because the optimum cell size for a bicontinuous morphology is determined by a unique (a-priori unknown) number of molecules $N*$, neither an NPT ensemble (where N need not be N*) nor a μVT ensemble will get around this issue.

Thus, to discriminate among competing phases and to determine the correct unit cell size of a bicontinuous phase, one needs to calculate free energies for different box sizes and identify the lowest free energy conditions and phases. However, simulating the free energy for such materials is highly non-trivial and is the biggest challenge that this work addresses. Indeed, since bicontinuous phases can be considered to be soft crystals (which are unique in having a very large number of molecules per unit cell), simulation of their free energies is subject to the key difficulties that were first pointed out by Swope and Andersen[110]. In particular, the use of periodic boundary conditions precludes the possibility of changing the number of unit cells, rising the potential of neglecting an additional contribution to the free energy corresponding to the number of unit cells N_c and the associated 'potential of the unit cell' ν_c:

$$d(\beta A) = U d\beta - \beta p dV + \beta \mu dN + \beta \nu_c dN_c \tag{4.1}$$

where $\beta = 1/k_BT$. Thus methods based on Equation 4.1 like those relying on molecular insertions to estimate chemical potentials are unreliable for free energy calculations of crystalline structures because: (i) they typically ignore the important finite size effect associated with constraining the number of unit cells, and (ii) they result in large error bars (arising not only from the chemical potential of each species but also from the pressure[88]. Although advanced methods have been proposed to concurrently calculate unit cell sizes and free energies for simple crystals[125], thermodynamic integration is the most appealing option when dealing with the complex DBC phases of interest. We have previously discussed the limitations of chemical-potential-based methods in connection to simulations of the G phase[88], and shown that they can be circumvented by using thermodynamic integration[57], which has also recently been shown to be effective in calculating the free energies of simpler morphologies in DBC systems[80, 83] and soft crystalline materials[19]. To the best of knowledge, however, such a method has not been applied to discriminate the stability of different bicontinuous phases.

The aims of this chapter are twofold: (i) To use a variant of thermodynamic integration to reliably estimate the correct unit cell size for bicontinuous phases in particle-based simulations, and (ii) to study the effect of homopolymer chain length on the stabilization of different types of bicontinuous phases. In particular, we will focus on the region of the phase diagram (parameterized by α and ϕ) near a triple point where the G, D, and P phases have been predicted to occur by SCFT.

4.2 Methods

4.2.1 Model for molecular interactions

We adopt a coarse-grained model of polymers based on the bead-spring soft potential model typically associated with DPD simulations. This model has been extensively used for capturing the microphase separation of DBCs while abstracting out detailed molecular information.[37, 45] We only describe here the most relevant model features; readers are referred to reference [88] for more details. Let U_{soft} be the contribution of the soft repulsive potential between all beads (irrespective of bead type) which depends on r_{ij}, the distance between the beads; and let U_{spring} be a harmonic potential that connects the different beads within a single polymer molecule which depends on rs, the distance between bonded beads:

$$U_{soft} = \sum_{i,j\neq i}^{\#\text{ beads}} U_{soft,ij}(r_{ij}) = \sum_{i,j\neq i}^{\#\text{ beads}} 12.5(1 - r_{ij})^2 \tag{4.2}$$

$$U_{spring} = \sum_{s=1}^{\#\text{ bonds}} U_{spring,s}(r_s) = \sum_{s=1}^{\#\text{ bonds}} 2r_s^2 \tag{4.3}$$

Finally, let U_{int} denote the interatomic potential between unlike beads in the system (where τ_i is the type of bead i) that depends on the strength of χ, the Flory-Huggins parameter:

$$U_{int} = \sum_{i,j;\tau_i\neq\tau_j}^{\#\text{ beads}} U_{int,ij}(r_{ij}) = \sum_{ij;\tau_i\neq\tau_j}^{\#\text{ unlike pairs}} 1.635\chi(1 - r_{ij})^2 \tag{4.4}$$

All simulations were performed at the monomer density $\rho = 3$, using $\chi N_{dbc} = 45$ and a DBC length of $N_{dbc} = 18$, each containing 6 beads of type A and 12 beads of type B. Correspondingly, the length of the homopolymer Nhom (restricted to whole number) was coupled to the parameter $\alpha = N_{hom}/N_{dbc}$. We used the values

$N_{hom} = 12(\alpha = 0.667)$, $N_{hom} = 13(\alpha = 0.722)$ and $N_{hom} = 14(\alpha = 0.778)$, since these were the ones closest to the triple point where the G, D, and P phases were predicted to coexist17. The volume fraction of homopolymer in the blend is given by ϕ.

We used molecular dynamics (MD) simulations with time step $\delta t = 0.05$ and cubic boxes of side L_{box} to explore a range of Lbox between 15 and 35. This range is broad enough to capture all three bicontinuous morphologies of interest, based on knowledge of the approximate unit cell sizes from Ref. [65]. From these simulations, we obtain a list of candidate ordered phases. We then expand or compress the box of any such phase to other desired L_{box} values and correspondingly insert or delete chains to maintain the target monomer density ($\rho = 3$). At the new box sizes, we run MD for an additional dimensionless time t* =10^5 units and ascertain that the morphology does not get destroyed. For more details, the reader is referred to Ref. [88]. We then use these configurations as starting point for calculating the free energies as described below.

4.2.2 Calculation of free energies

Construction of a reversible path

To evaluate the free energy of a target ordered phase at given conditions ($\chi N, \phi$, and α) we use a reference state with $\chi N = 0$ where the A-B DBC plus A-homopolymer blend behaves as a disordered blend of homopolymers. Such a reference state is convenient since it will be the same for any ordered phase that may form at different box sizes at the χN of interest (for given ϕ and α). However, evaluating the free energy difference between the ordered state or state 1 (at high χN)

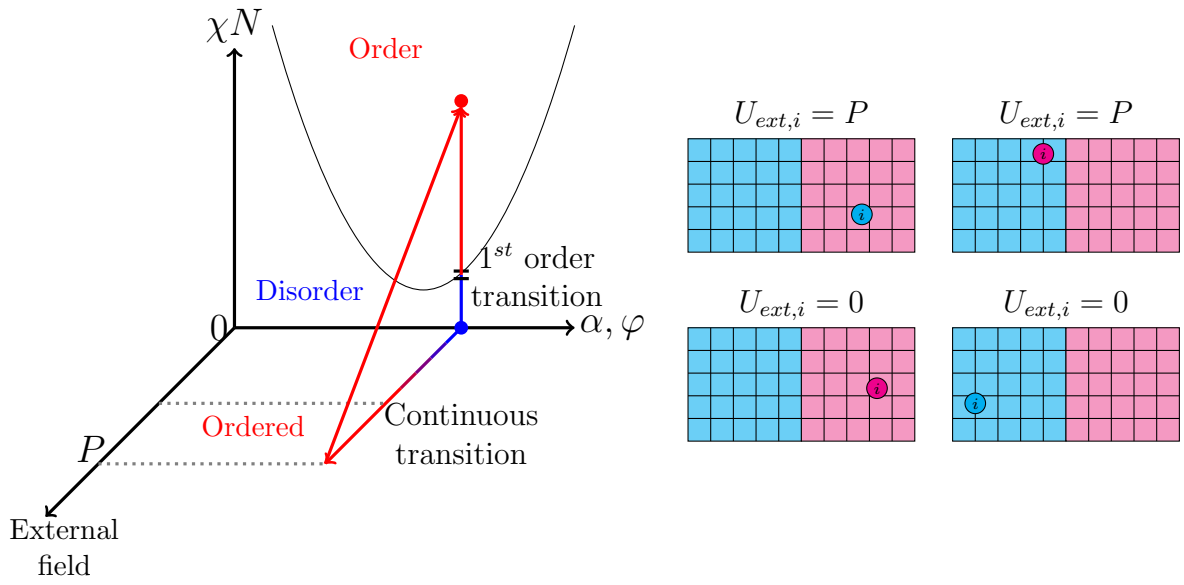

Figure 4.1: Illustration of the reversible path to caculate free energy.

and the disordered state or state 0 (at $\chi N = 0$) involves at least one phase transition (e.g., a disorder-to-order transition) and it is typically very difficult to directly pinpoint the phase transitions via simulations due to the significant hysteresis that occurs upon heating or cooling the sample across transitions.

The method of thermodynamic integration to calculate free energy differences across a phase transition relies on using a suitably parametrized potential energy function that can gradually be turned off and on to bridge the different phases involved in the transition. We construct a reversible (hysteresis-free) path along a phantom dimension by applying an external field whose strength can be changed to drive the transition (Figure 4.1a). Previous authors have employed a similar technique[80, 82] but we introduce some specific adaptations. Our external field is generated by creating a grid in the simulation box that forms a pixelated representation of the phase segregated morphology (i.e., the A and B domain volumes are discretized into voxels) and gradually applying an energy penalty P (in k_BT units per atom) for any bead that is located in the wrong voxel type. No penalty is

applied if the bead is in the correct region, as illustrated in Figure 4.1b. This step involving the application of the external field Uext will be referred to as Branch 1 and its parametrizing variable as ξ. Subsequently, in branch 2 we increase χN in U_{int} (parametrized by λ) while concurrently remove the external field P. The overall potential for this process is given by

$$U(\xi, \lambda) = U_0 + \xi U_{ext} + \lambda(U_{int} - U_{ext}) \tag{4.5}$$

$$U_0 = U_{soft} + U_{spring} \tag{4.6}$$

And the free energy change for the two-branch process is:

$$\Delta F(\text{disorder} \rightarrow \text{order}) = \Delta F(\xi : 0 \rightarrow 1; \lambda = 0) + \Delta F(\xi = 1; \lambda = 0 \rightarrow 1) \tag{4.7}$$

$$\Delta F = \int_0^1 \left\langle \frac{\partial U}{\partial \xi} \right\rangle_{\xi,\lambda=0} \mathrm{d}\xi + \int_0^1 \left\langle \frac{\partial U}{\partial \lambda} \right\rangle_{\xi=1,\lambda} \mathrm{d}\lambda \tag{4.8}$$

$$= \int_0^1 \langle U_{ext} \rangle_{\xi,\lambda=0} \mathrm{d}\xi + \int_0^1 \langle U_{int} - U_{ext} \rangle_{\xi=1,\lambda} \mathrm{d}\lambda \tag{4.9}$$

Calculation of the external field

The ordering field U_{ext} is defined on a cubic grid in the simulation box. The geometry of the external field can be obtained either from: (i) simulated morphologies derived from those spontaneously nucleated or (ii) the idealized phases predicted by SCFT. In principle, the proposed free-energy calculations should not depend on the precise field geometry chosen, provided that it drives the system into the target phase and it does not leave any spurious effect that lingers in the final morphology (once the field is turned off). Unless otherwise stated, we used approach (i) as the details of the geometries thus generated (like node and tube shapes and

dimensions) were expected to be closer to those of the target phase. Additional details of this approach are described in Section 4.5.1.

Choosing the strength of the external field P is an important consideration for computational efficiency since too strong a P will make both branches longer. Indeed, P should be just strong enough to induce order in the system. For this, we examined the evolution of both the structure factor (calculated according to reference[99] and the average chain end-to-end distances for a system that forms a diamond phase at $\phi = 0.3, \alpha = 0.722$ in a $20 \times 20 \times 20$ simulation box. A value of $P > 1k_BT$ per bead was found to be sufficient to attain the ordered structure factor while a value of $P = 5k_BT$ was an overkill; we henceforth adopt a conservative value of $P = 2k_BT$ per bead.

Based on the position $\mathbf{r}_i$, each bead i is assigned to a voxel in the grid we created, $v(\mathbf{r}_i)$. The external potential applied depends on the type of bead τ_i and the average density of that monomer in the voxel $[\rho^*_\tau(v)]$ and is defined as follows:

$$U_{ext,i}(v(\mathbf{r}_i); \tau_i) = \begin{cases} P & , \rho^*_\tau(v) > 0.5 \\ 0, & \rho^*_\tau(v) < 0.5 \end{cases} \tag{4.10}$$

Finally, we have $U_{ext} = \sum_i^{\#\text{ beads}} U_{ext,i}$.

Assessing integration methods

The next question in using thermodynamic integration is to select a method to obtain free energy changes. Some authors[88, 80] have used expanded ensembles (EXE)[63, 58, 13] to obtain the total free energy change along the integration path

in a single simulation (by calculating and adding up free energy differences between neighboring stages along the path). The relative probability of transitioning between adjacent values of the integration parameter (for example, ξ), which is proportional to $\exp(-U_{ext}\Delta\xi)$ since $k_BT = 1$, should ideally be between 0.1 and 1 for obtaining a flat histogram in the expanded ensemble and to get good statistics. Since at $\xi = 0$ the morphology is disordered, a large number of beads will reside in the 'wrong' grid, resulting in a large contribution to U_{ext}. This would require the ξ-staging to have very small step sizes with several hundred such steps to cover the entire ξ range, leading to an exponential increase in the time needed to complete a round trip thus making impractical the generation of enough round trips to attain accurate statistics. A partial workaround for this issue is to use a "divide and conquer" strategy so that the ξ steps are grouped into several "blocks" so that numerous round trips can be achieved within each block. However, a more common way to overcome such an issue (well-suited to large-system sizes) is by using methods that do not require the system to be able to jump between neighboring ξ states; e.g., by using suitable numerical quadrature formulas.

We hence chose to run several parallel simulations at selected values of the integration parameter and to evaluate the integrals in Equation 4.9 numerically. Several such quadrature methods exist and have been used in molecular simulations; namely: (i) Trapezoid and Simpson's quadrature (for uniform spacing of ξ and λ), (ii) Curve fitting (with arbitrary choice of spacing) followed by an analytical integration of the curve[102, 55, 86], and (iii) Gaussian quadrature - Lobatto or Legendre[104, 19] scheme (for prescribed spacing of ξ and λ). To identify the best technique, we calculated the free energy change for a model lamellar phase with $L_{box} = 10$ at $(\chi N, \phi, \alpha) = (45, 0.300, 0.722)$. The smallness of the box size results in a (metastable) lamellar phase, albeit with a high free energy, and forms

entirely due to the strong confinement. Nevertheless, these simulations are more than an order of magnitude faster than those for the box sizes relevant to this work and allow us to test several spacings of the integrating parameters ξ and λ and variations of the quadrature technique. Based on these comparisons, which are described in detail in Sections 4.5.2 and 4.5.3, in subsequent simulations, we adopted an 11-point Gauss-Legendre quadrature for each of the two integration branches.

The starting configurations for each of the points along the integration branches are generated serially starting from $(\xi, \lambda) = (0, 0)$ and using the final snapshot of a previous point until the entire path has been traversed. Longer equilibration times (2×10^5 MC cycles) are required when the morphology is disordered and shorter equilibration (5×10^4 MC cycles) is sufficient after the morphology becomes ordered. After equilibration, data is collected for at least over 10^6 MC cycles for each point, with up to 3×10^6 cycles for values ($\xi < 0.2; \lambda = 0$). Errors for each value of (ξ, λ) are estimated using block averages as described in Ref. [31], and since the Gaussian quadrature scheme is a weighed summation, the total error is calculated by weighting and summing over the individual errors.

4.3 Results and discussions

We choose specific regions within the previously predicted SCFT phase diagram[67] as shown in Figure 4.2 to calculate the free energies using particle-based simulations. First, we briefly focus on the region marked by an X in Figure 4.2 where the G phase at $(\phi, \alpha) = (0.100, 0.722)$ is the only morphology expected to be stable; this state is used to validate the TI method. Subsequently, we focus our attention

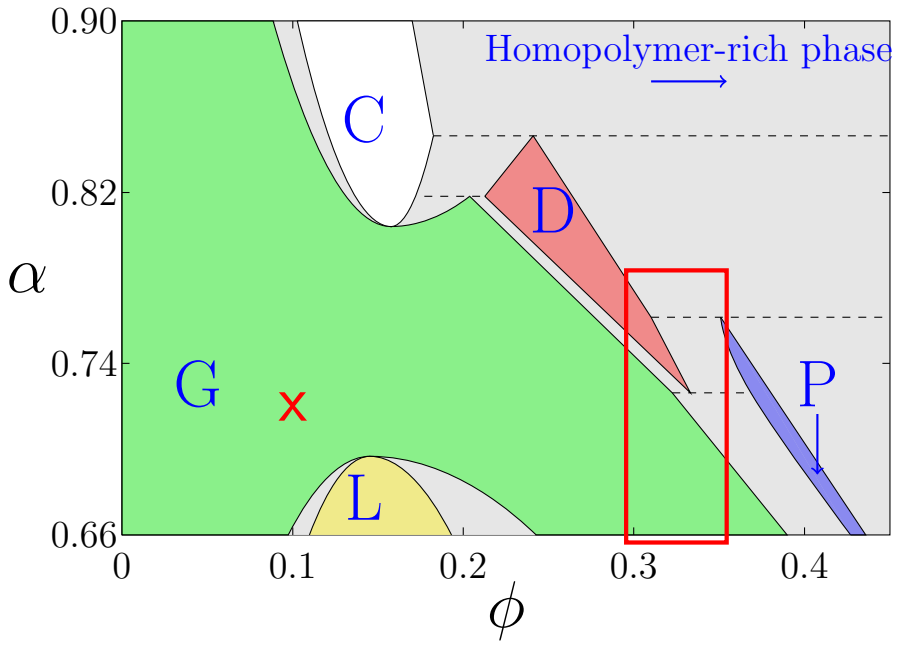

Figure 4.2: Phase diagram as predicted by SCFT[67] showing C and L phases in addition to G, D and P phases. Using particle-based simulations, we studied the point marked by a red cross and the region within the red box.

on the region enclosed by the red box in Figure 4.2 that contains the triple point where the G, D and P phases coexist.

4.3.1 Finding the correct box size

At $(\phi, \alpha) = (0.100, 0.722)$, we find that a G phase spontaneously nucleated at $L_{box} = 24$. Other box sizes nucleate disordered tubes connected by nodes. Using chain insertions and deletions to keep the target density, we obtain the G phase at neighboring box sizes with ΔL_{box} of -1.5, -1 and +1 (relative to the $L_{box} = 24$ base case). We subsequently run MD simulations for at least 10^6 time steps and determined the average morphologies for which to calculate the free energy.

The free energy per monomer is plotted for these box sizes in Figure 4.3. From

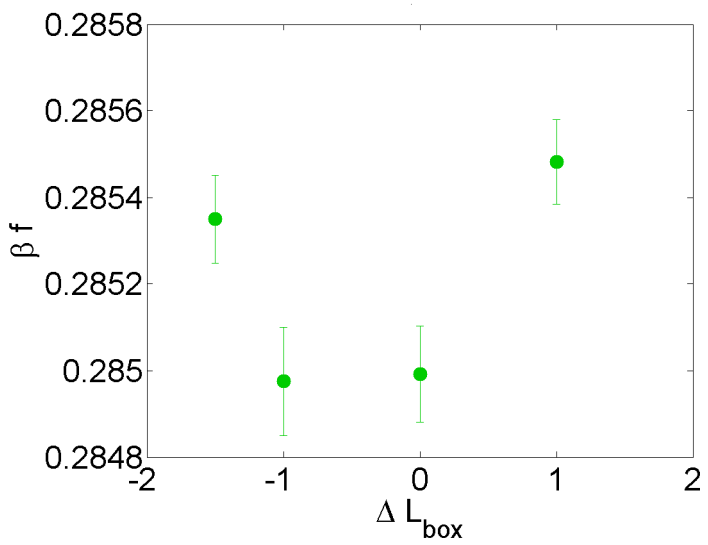

Figure 4.3: Free energy calculated using thermodynamic integration for the G phase in a DBC + homopolymer blend at $(\phi, \alpha) = (0.100, 0.722)$.

these, we see that the free energy goes through a clear minimum with respect to box size, and the optimum box size for the G phase at these macro-conditions of ϕ and α is between 23 and 24. These error bars can further be reduced by running longer simulations depending on the resolution required, especially if competing phases are present with similar free energies values. The fact that the most stable box size (lowest free energy) within the discretization of box lengths tested – essentially corresponds to the box size where the G phase formed spontaneously, is consistent with the intuitive notion that it would also have the lowest nucleation free-energy barrier from the disordered state.

4.3.2 Vicinity of the triple point

Spontaneously formed morphologies

From MD simulations, we get a variety of ordered morphologies that spontaneously formed from a disordered melt in the range $0.3 \leq \phi \leq 0.35$ and $0.667 \leq \alpha \leq 0.778$. The box lengths at which these were spontaneously formed are given in Table 4.1. The D phase forms at all the values of (ϕ, α) studied. These D morphologies have two nodes in the unit cell, and on replicating the structure in all directions, we get two interweaving networks of the minority component A. The cylinder (C) morphology is observed at box sizes quite close to those where the D phase forms, and each unit cell has one tube in the [111] direction which forms a hexagonal pattern upon replicating the simulation box. The P phase forms at three of the nine points explored, and each simulation box contains two nodes, one belonging to each network. The G phase occurs only at $\phi = 0.3$ and each simulation box contains sixteen nodes, eight belonging to each network. Since each G network is chiral, more nodes are present within a unit cell than for the other morphologies, hence requiring larger box sizes. The G phase formed at $\alpha = 0.667$ was found to contain a defect which could not be averaged out. The spontaneous box sizes of all morphologies generally increase upon increasing either ϕ or α, the only exception being at the box size where the defective G phase formed.

Morphology stability

The results for the free energy calculations are shown in Figure 4.4, where f is the Helmholtz free energy per monomer and $\beta = 1/k_B T$. The difference between the βf for each calculation and the lowest βf (called βf_{min}) among all box sizes

	$\phi = 0.300$		$\phi = 0.325$		$\phi = 0.350$	
	L_{box}	Phase	L_{box}	Phase	L_{box}	Phase
$\alpha = 0.778$	20 21	C D	22	D	22,23 28	D P
$\alpha = 0.722$	20 33	D G	23 21,22 25	D C P	22 27	D P
$\alpha = 0.667$	20,21 34	D Defective G	21	D	21,22 23	D C

Table 4.1: Ordered morphologies at their spontaneously nucleated box sizes

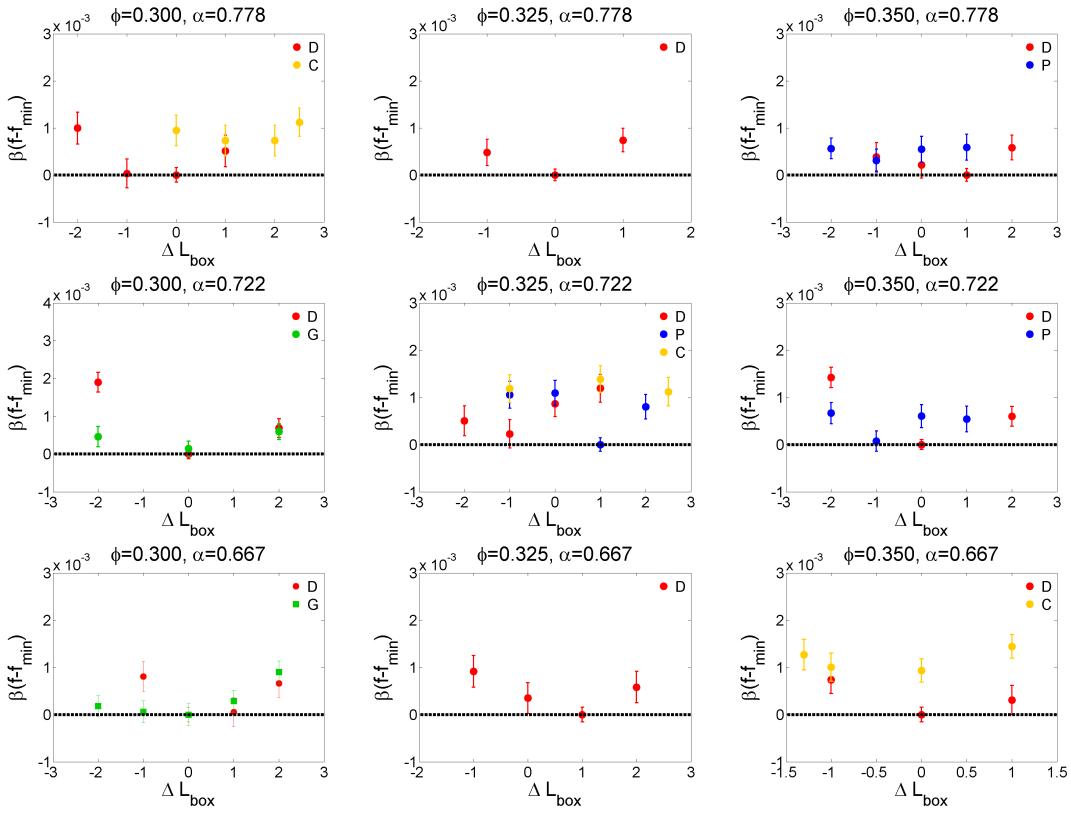

Figure 4.4: Per monomer free energy differences between the current phase and the most stable phase at the given macroconditions for the for the DBC + homopolymer blend at $\chi N_{dbc} = 45$ with the (ϕ, α) composition indicated. ΔL_{box} is the difference between the L_{box} of a given phase and the smallest L_{box} where that phase formed spontaneously.

and morphology types for the same (ϕ, α) is plotted against ΔL_{box}. ΔL_{box} is the difference between the box size the free energy is evaluated at, and the box size at which the morphology was spontaneously formed (see Table 4.1). In cases where there are more than one box size at which the morphology nucleates, we choose the lower value. For the G phase at $(\phi, \alpha) = (0.300, 0.667)$ only, we calculated the free energies by using the SCFT-based external field as explained in Section 4.2.2. As can be observed, the free energies for all morphologies exhibit a minimum at or near $\Delta L_{box} = 0$. Errors calculated in f by block averages are smaller than 5×10^{-4} and may further be reduced by running longer simulations. Specific comments on each phase follows:

C phase: The C phase is not the stable morphology at any of the (ϕ, α) values tested and only appears accompanying the D phases. Typically, but not always, it nucleates when the box size is slightly mismatched for the optimum D morphology. At $(\phi = 0.325, \alpha = 0.667)$ and $(\phi = 0.325, \alpha = 0.778)$, the D phase is the only ordered phase to appear at all.

D phase: For the shortest homopolymer added $(N_{hom} = 12, \alpha = 0.667)$, the D phase is completely stable for $0.3\phi0.35$. The G and C phases are metastable with respect to the D phase. Upon increasing to 0.722, the D phase has arguably a slightly lower free energy with respect to the G phase at $\phi = 0.3$, but has a slightly higher free energy with respect to P phase at $\phi = 0.325$, and comparable to the P phase (within error bars) at $\phi = 0.35$. For higher $\alpha = 0.778$, the D phase again has the lowest free energy compared to all other competing phases (i.e., the C and P phases).

P phase: It is stable only at $(\phi = 0.325, \alpha = 0.722)$. At $(\phi = 0.350, \alpha = 0.722)$, its free energy is within error bars from that of the D phase, indicating that these

	$\phi = 0.300$		$\phi = 0.325$		$\phi = 0.350$	
	L_{box}	Phase	L_{box}	Phase	L_{box}	Phase
$\alpha = 0.778$	21	D	22	D	23	D
$\alpha = 0.722$	20	D	26	P	22	D
	33	G			26	P
$\alpha = 0.667$	20	D	22	D	22	D
	34	G				

Table 4.2: Stable morphologies and box sizes

two morphologies may coexist.

G phase: It appears only at $\phi = 0.3$, and for both $\alpha = 0.667$, and $\alpha = 0.722$, it is of comparable free energy with the D phase, indicating that these two morphologies may coexist.

The summary of stable phases and findings are given in Table 4.2. In the region of parameter space we explored, the D phase is the predominant stable phase. Although we do not find a point that could be assigned to be a triple point where the G, P, and D phases would coexist (which SCFT predicts in this region), one can argue that somewhere in between the $(\phi, \alpha) = (0.300, 0.722)$ composition where the G and D "coexist, and the $(\phi, \alpha) = (0.325, 0.722)$ composition where the P and D phases almost coexist, would be a good candidate for a triple point. Interfacial simulations that could probe the direct coexistence among these morphologies are highly non-trivial given the disparate unit cell sizes involved and are not addressed in this work.

Direct one-to-one comparison between SCFT and MD phase diagrams is challenging due to the disparity in the assumptions underlying these models. For DBCs, the χN at which the order-disorder transition occurs for chains of finite length and soft DPD beads is higher than that predicted by SCFT. This partially motivated our choice of a higher value of $\chi N = 45$ in our simulations to allow for

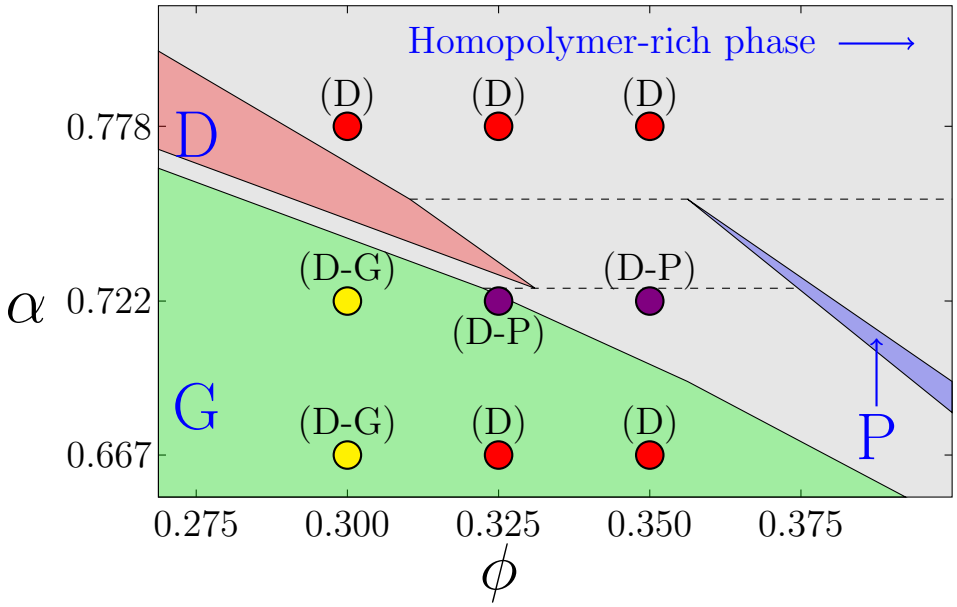

Figure 4.5: Comparison between phase diagrams from SCFT (full lines) and MD (dots). Green: stable G phase, red: stable D phase, purple: D coexisting with P, blue: G coexisting with P and yellow: G coexisting with D

an approximate comparison with a $\chi N = 25$ SCFT phase diagram. Furthermore, the SCFT phase diagram was found to be little sensitive to changes in χN near the triple point[1]. Figure 4.5 compares our results from those obtained from SCFT[67]. The ordered bicontinuous phases from SCFT are in colored regions while the gray regions denote two-phase coexistence. Results from our MD simulations are overlaid using circles. We have good agreement for all three a points at $\alpha = 0.778$, and for the D-P coexistence regions at $\alpha = 0.722$. For $(\phi, \alpha) = (0.300, 0.722)$ our results are indicative of a D-G phase coexistence region, a location that is not far from the corresponding region predicted by SCFT. For the $\alpha = 0.667$ case, however, our results do not agree with SCFT. In particular, the $\phi = 0.300$ point would be expected to have the highest propensity to form a stable G phase for being the farthest from the (SCFT-predicted) phase boundary. Instead, our results for

[1]SCFT calculations by J. C. Araque showed that the phase diagram was essentially unchanged by increasing χN up to 30.

$(\phi, \alpha) = (0.300, 0.667)$ indicate a D-G phase coexistence since both phases have similar free energies. Therefore, our MD results indicate that the stability region of the D phase and D-G coexistence regions is larger than that predicted by SCFT near the triple point. For higher ϕ, the G phase has disappeared and D is the only stable ordered phase. Aside from kinetic reasons that may have precluded the timely formation of the G phase in simulation, the decrease in stability of the G phase may be attributed to density fluctuations that become progressively more important as decreases, leading to deviations from SCFT predictions.

4.3.3 Analysis of microstructure

Particle-based simulations allow us to probe the microscopic details of the different bicontinuous morphologies. In this section we primarily revisit the notion of packing frustration, which has been a successful framework to explain why some bicontinuous morphologies are usually unstable in amphiphilic systems[75]. Some studies rationalize such differences in stability by examining interfacial curvatures and mathematical descriptions of idealized surfaces[69, 36]. However, particle-based simulations yield fluctuating interfaces with transient non-idealities and hence it is more convenient to look at packing frustration from the chain stretching perspective. Bicontinuous networks consist of approximately cylindrical short tubes or struts which are interconnected by nodes to form the network. Since the nodes are bulkier than the tubes, their centers are at a greater distance from the interface and DBCs straddling the nodal surface have to stretch to occupy the centers of the nodes. This stretching, however, leads to a loss of conformational entropy since the chains would prefer to adopt more relaxed conformations. Failure to stretch results in low density regions near the centers of nodes, which would lead

to a loss of mixing entropy. Both scenarios are manifestations of entropic packing frustration and their interplay contributes toward shaping the stable morphology.

To detect signs of packing frustration in our systems, we calculated the average end-to-end distances of the A-blocks in each molecule while keeping track of the location of the voxel containing the center of mass of that block. First, we identify the individual networks by calculating clusters of voxels where the density of A beads (see SI) is greater than 0.5. Within each network, we calculate the distance of each voxel from the interface (edge of the cluster), d_i. For bicontinuous networks, centers of nodes are well defined within the network as the geometric center of the set of voxels with maximum d_i. From the geometric center of each node, we also calculate the distance of each A-type voxel within the network, d_c. Further details of this calculation are provided in the section 4.5.4. Finally, we calculate the mean square end-to-end distance of the chains and the number of chains with centers of masses in voxels parametrized by the pair of values (d_i, d_c). The end-to-end distances (calculated for ten snapshots to improve statistics) are normalized by the average end-to-end distances in a homopolymer melt of the same length as the A-blocks of the chains.

We confine our analysis to the three bicontinuous morphologies near the triple point where they have almost identical composition (i.e., similar α and ϕ). We show plots for the mean square end-to-end distances $\langle R^2 \rangle$ in Figure 4.6, averaged over (a) d_i and (b) d_c. From Figure 4.6a, we see that the DBCs are confined near the interface within $0 \leq d_i \leq 3$ and that there is a remarkable increase in end-to-end distance $\langle R^2_{dbc} \rangle$ indicating that the chains overstretch for $d_i > 1$. Homopolymer chains, on the other hand, have relaxed conformations with a mean square end-to-end distance $\langle R^2_{hom} \rangle$ around unity. Conceptually, this observation is consistent with

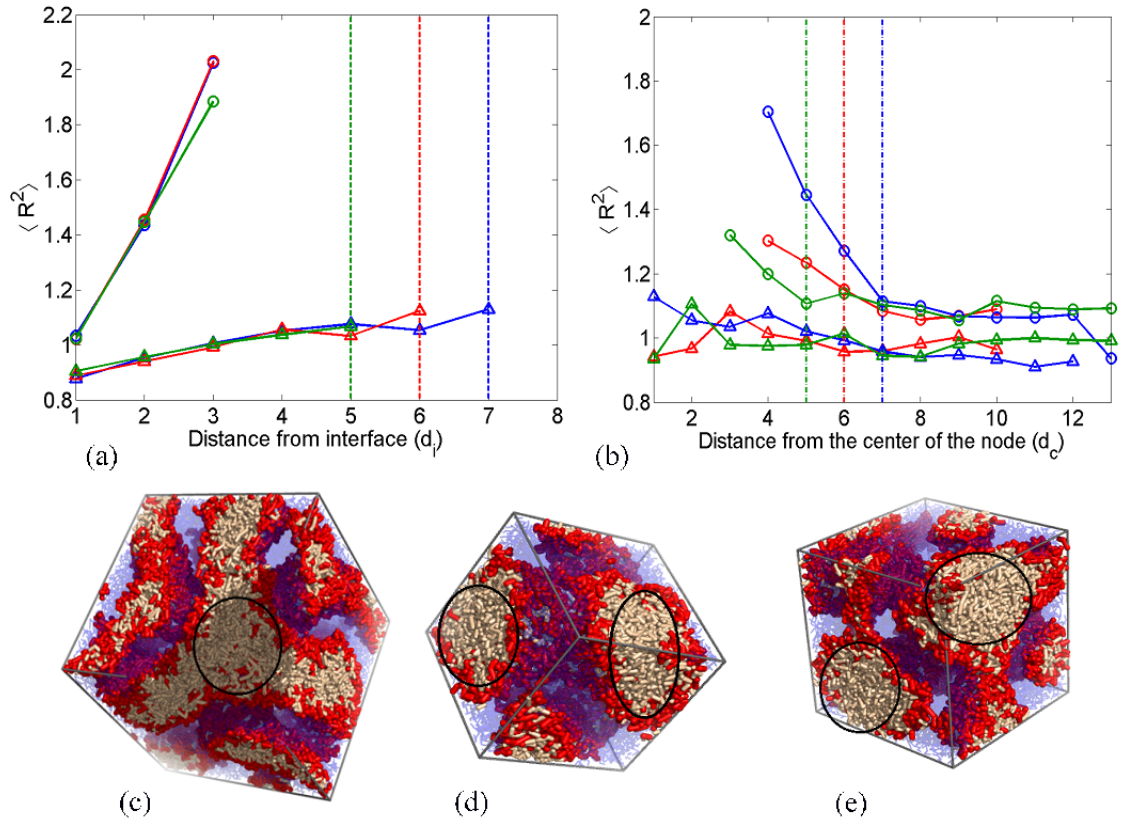

Figure 4.6: Mean square end-to-end distances for DBCs (circles) and homopolymers (triangles) as a function of d_i (a) and, d_c (b). Symbols are in green for the G phase at $(\phi, \alpha, L_{box}) = (0.300, 0.722, 33)$, red for the D phase at $(\phi, \alpha, L_{box}) = (0.325, 0.722, 22)$, and blue for the P phase at $(\phi, \alpha, L_{box}) = (0.325, 0.722, 26)$. The colored vertical dashed lines denote the node radius for the corresponding morphology. Snapshots of G (c) , D (d) and P (e) phases. Homopolymer is shown in brown and DBC is shown in red (A-block) and blue (B-block). Black circles show the nodes.

the notion that it is through homopolymer chains maximizing their conformational entropy (inside the A domains) that bicontinuous phases with larger nodes can be stabilized. There is a slight decrease in $\langle R^2_{hom} \rangle$ from unity as the chains get closer to the interface, where the chains are expectedly more confined since they do not penetrate into the B domains. Finally, the node radius (r_{node}) is inferred from the maximum value of d_i for each phase (marked with a dotted line in Figure 4.6a).

In Figure 4.6b ($\langle R^2 \rangle$ vs. d_c), we again observe that DBCs stretch as they penetrate the node ($d_c < r_{node}$, where r_{node} is marked by a dotted line). Furthermore, DBCs stretch more for phases with larger nodes. Since these morphologies allow probing the effect of enlarging the nodes while preserving the total volume fraction of A-type beads, we calculated for each phase the fraction of each type of chain within the node with respect to the total number of chains of that type. Going from $G \rightarrow D \rightarrow P$, the fraction of homopolymer chains increases from $0.27 \rightarrow 0.55 \rightarrow 0.79$, while for DBC chains (lining the node surface) it increases from $0.11 \rightarrow 0.23 \rightarrow 0.41$. As the node volume increases, both types of chains are increasingly confined to the nodes.

Packing frustration in a phase would be significant only if a large number of chains stretch to a large degree. In Figure 4.7 and in Section 4.5.4 we plot population color maps where the surface height is proportional to the total number of chains for all voxels at a distance d_i and d_c and the color represents the corresponding $\langle R^2 \rangle$. Those plots show that the maximum number of DBC centers of mass lie at the interface ($d_i = 1$), while a maximum number of homopolymer centers of mass lie just below the interface, i.e., at $d_i = 2$. Further, all morphologies have an overall normalized $\langle R^2 \rangle$ value close to 1, implying that the chain conformations approach those of the pure homopolymer melt, even for the DBC chains.

The color maps for the homopolymers also capture some physical attributes of the interconnecting tubes, as illustrated in Figure 4.7 for the P phase . The gray surface marks the boundary of the node; the region toward the reader being the node while the region farther back being the tubes. From the tube region in Figure 4.7 one can conclude that the tubes have a constant thickness and do not taper as one goes away from the node. We denote the maximum value of d_i outside

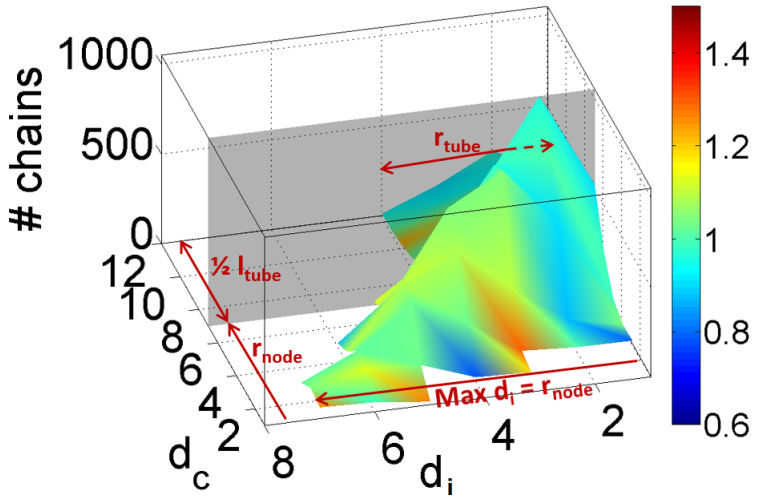

Figure 4.7: Population color maps showing the number of chains as a function of d_c and d_i and color coded based on $\langle R^2_{hom} \rangle$ for P phase: $(\phi, \alpha, L_{box}) = (0.325, 0.722, 26)$.

the node as r_{tube}. The P phase has a well-defined and bulky node ($r_{node} > r_{tube}$), whereas it is less demarked for the D phase and the size of the node is almost indistinguishable from the tube ($r_{node} \approx r_{tube}$) for the G phase for $\phi \geq 0.300$ (see Section 4.5.4). This latter blurriness of the nodal interface (rooted in dynamic fluctuations) could be one of the underlying reasons why $\phi = 0.300$ is at the limit of stability of the G phase. At conditions where the G is the only stable phase; e.g. for $(\phi, \alpha) = (0.100, 0.722)$, one has that $r_{node} > r_{tube}$ despite that $\langle R^2_{hom} \rangle$ deviates from unity (see Section 4.5.4).

As the number of tubes per node increases, the corresponding tube thicknesses actually decreases for these morphologies ($r_{tube} : 5 \rightarrow 4 \rightarrow 3$ while $r_{node} : 5 \rightarrow 6 \rightarrow 7$ as $G \rightarrow D \rightarrow P$). Furthermore, we know the average distance between nodes which is $2\pi/q^*$, where q^* is the abscissa of the primary peak of the structure factor. From this and our knowledge of the node radius, we can calculate the average length of the interconnecting tubes which goes as $l_{tube} : 17 \rightarrow 13.5 \rightarrow 12$ as

$G \rightarrow D \rightarrow P$. Both of these observations are consistent with a smaller fraction of homopolymers residing in the tubes and being distributed among more numerous, thinner and shorter interconnecting tubes.

4.3.4 Free energies of structures containing defects

Another important consideration in analyzing bicontinuous structures is the effect of morphological defects on their free energy and relative stability. This can be illustrated with the G phase that spontaneously nucleated at $\phi = 0.300$ for $\alpha = 0.667$ which contained a defect in one of the nodes as shown in Figure 4.8a. When such a structure is used to define the geometry of the external field in the thermodynamic integration, the nodal defect lingers throughout and leads to G-phase free energies which are slightly larger than those that we obtained using a defect-free external field (based on SCFT). This comparison is shown in Figure 4.8b where, interestingly, the optimal box size for the defect-containing G phase is larger ($L_{box} = 35$) than that for the defect-free G phase ($L_{box} = 34$). The difference in the free-energy minima between these two morphologies (evaluated at those optimal box sizes) can be seen as the free-energy cost associated with the nodal defect.

A second kind of defect we investigated was the volume asymmetry of networks within the spontaneously nucleated bicontinuous phase. The two minority component networks do not intersect and the diffusive barrier is too high for the timely exchange of either type of molecules between the two networks. Therefore, once nucleated, the structures asymmetry remains essentially fixed, allowing only minor fluctuations. The asymmetries we obtained ranged from 0.1% to 7% (see details in Section 4.5.5) which produced free energy differences of about 2×10^{-4} (in $k_B T$

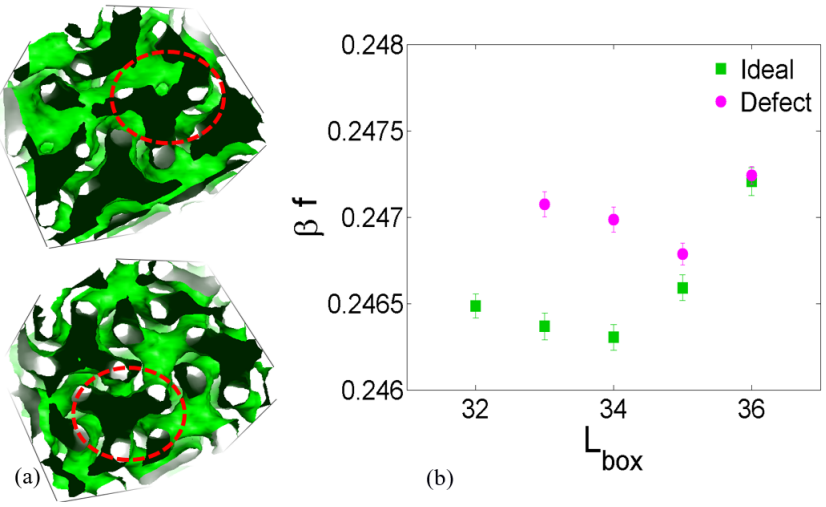

Figure 4.8: (a) Morphology of G phase at $L_{box} = 34$ obtained using U_{ext} generated from a defective (top) and non-defective (bottom) G morphology. The regions inside the red ellipse show the same nodal region in both morphologies, highlighting a defect in one of the networks of the top phase. (b) Free energies for the G phase obtained from the defect-based U_{ext} and the non-defect-based U_{ext} at $\phi = 0.300, \alpha = 0.667$.

units), which is slightly higher than the error bars in the individual simulations (1.2×10^{-4}), but significantly lower than the change produced by the defect studied in Figure 4.8.

To the best of our knowledge, this is the first time that free energies of specific defects have been calculated for any bicontinuous phase. Understanding the free energies of defects is the first step in identifying the free energy landscape of a particular phase, and subsequently, to probe the barriers to morphology formation for kinetic studies.

4.3.5 Nucleation of bicontinuous phases

Having identified conditions (and box sizes) at which the G, D, and P phases are stable, we can use them to monitor the dynamic process by which they are spon-

taneously nucleated. A rigorous analysis of their nucleation kinetics would entail not only simulating free energy barriers but also creating an ensemble of transition pathways (for selected values of supersaturation) so as to identify transition states and quantify rates. These calculations require specialized techniques such as forward flux sampling[113, 2] or the string method[49], and larger system sizes (to reduce finite size effects); such highly challenging calculations are beyond the scope of this work.

We can nonetheless get some preliminary insights into the ordering process by following the trajectories of brute-force simulations. By starting from a completely disordered state (stable at high temperatures or $\chi N \to 0$), we are enacting a very rapid quench at the temperature (or χN) of interest so that there is a significant degree of supercooling (or supersaturation) of that initial metastable disordered phase that drives it into the stable ordered state. We illustrate this analysis for the D phase and at conditions chosen because a competing C phase also appears at very similar box lengths; namely at $(\phi, \alpha) = (0.300, 0.722)$ and $L_{box} = 20$.

For $\chi N = 45$, we may get either the D phase or the C phase depending on the random seed used to assign velocities at the start of the simulation. At this degree of supercooling, the A domains first coarsen and later coalesce then align to form the final morphology, as shown in Figure 4.9. We also looked at the evolution of the structure factor at the wave vector magnitudes (q) corresponding to the first four peaks of the phase.. For the D phase[112] these occur at ratios $\sqrt{2} : \sqrt{3} : \sqrt{4} : \sqrt{6}$, and for the C phase[30] at $1 : \sqrt{3} : \sqrt{4} : \sqrt{7}$. The first peak occurs at $\sqrt{2}\pi/L_{box}$ for the D phase and $4\pi/(\sqrt{3}L_{box})$ for the C phase pointing in the [111] direction. When forming the D phase at $\chi N = 45$, the first four peaks grow during coarsening until $t^* \sim 1000$. Afterwards, as the domains split into two

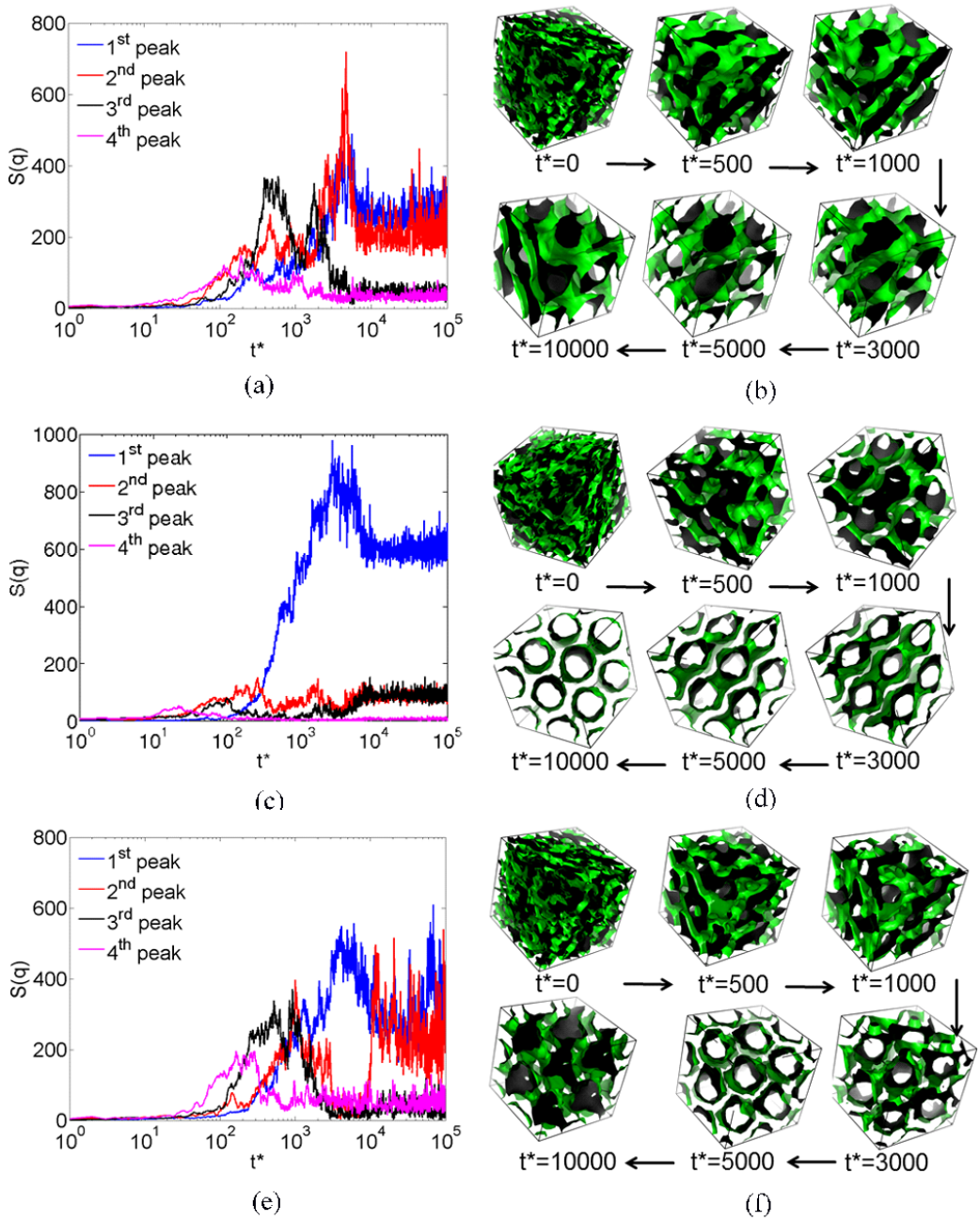

Figure 4.9: Evolution from structure factor peaks and snapshots of C and D phases. (a), (b): D phase formation at $\chi N = 45$. The second peak shows a sharp maximum when the morphology splits into two distinct networks. (c), (d): C phase formation at $\chi N = 45$. The first peak is significantly larger than subsequent peaks. (e),(f): D phase formation through C phase intermediate at $\chi N = 30$. Morphology first segregates into aligned cylinders with small defects which later order into the D phase. The second peak increases from low (C-like) values to a high (D-like) value.

non-intersecting networks, the second peak rises sharply before settling to a value close to the first peak height. In contrast, *en route* to forming the C phase (Figure 4.9c), prolate domains align by $t^* = 1000$ causing the first peak to rise above the others and is the highest at around $t^* = 3000$ where the morphology resembles a perforated lamellae. As the perforations decrease to form the C phase, the first peak settles to a steady value, much higher than the second peak. Interestingly, at lower $\chi N = 30$ (corresponding to a lower degree of supersaturation), we observe a transition from the C to the D phase within a total simulation time of $t^* = 10^5$ – as detected by both visual inspection of the morphology and the evolution of structure factor peaks (see Figure 4.9e). We note that such a reduction of χN is mostly expected to slow down the kinetics of the ordering process, while leaving the relative stability of the D and C phases largely unchanged (as per unreported SCFT calculations).

Altogether, our results suggest that in the formation of the D phase at the conditions studied, the C phase or a defective C phase (e.g., a phase containing aligned but partially connected prolate domains) could in some spatial regions be an important intermediate that ripens into the final D morphology. Whether partially connected cylinders may also play a role in preforming the tubes and nodes associated with other bicontinuous structures remains to be explored. In a methodological context, our results suggest that the structure factor peak heights may be an informative order parameter for future studies concerned with tracking the evolution of phase transitions involving bicontinuous phasees.

4.4 Conclusions

We have demonstrated the use of thermodynamic integration to calculate the free energies of bicontinuous phases using a two-branch reversible path evaluated using Gauss-Legendre quadrature. Other free energy calculation techniques (e.g., based on calculations of chemical potentials) usually ignore the effect of constraining the number of unit cells in the simulation box[110]. In the parameter range we investigated; i.e., $0.3 \leq \phi \leq 0.35$ and $0.667 \leq \alpha \leq 0.778$ and $\chi N = 45$, the D phase is the predominantly stable phase. Conditions are identified where the P and the D phases as well as the G and D phases have free energies very close to each other, which would foreshadow a proximal coexistence region for these pairs of phases.

Furthermore, our approach identifies the optimum box size, which is particularly important for bicontinuous phases whose free energy is very sensitive to the simulation box length. In this study we only obtained the optimum box size within a discretization of $\Delta L_{box} = \pm 1$ in box length; if a higher accuracy is desired, one may perform calculations for smaller ΔL_{box} values. In most cases, the box length at which a phase nucleates spontaneously coincides with that of the optimum box size inferred from free energy calculations. Having identified the most stable phase at particular conditions, we probed the effects of microscopic details of the spontaneously formed network phases. We found that defects in the geometry of the external field used in the integration can affect the resulting free energy if such defects do not anneal out in the final target structure. We also found that the relative volume asymmetry between the two networks, if less than 7%, does not significantly affect the free energy, but such small differences could slightly alter the coexistence regions for the P phase and the relative stability between the G

and D phases.

We also examined how the chains are spatially distributed within different regions of these bicontinuous phases. The homopolymers are expectedly excluded from the A-B interfaces while the DBCs are absent in the tube interiors. Our analysis based on distributions of the distance between the center of mass of individual chains and the interfaces reveals some structural details not apparent using visual inspection. For example, the G nodes and tubes are of similar thicknesses at conditions where the stability of the G phase is borderline, while the node and tubes are more distinguishable in size at conditions where the G phase is fully stable. As the nodes get larger going from $G \rightarrow D \rightarrow P$, the chains spatially redistribute to accommodate both more homopolymers within the nodes, and more DBCs on the surface of the nodes. These trends result in the interconnecting tubes getting both thinner in radius and shorter in length. In all morphologies, the majority of chains have end-to-end distances close to that of a pure homopolymer of the same length in the melt state, and only a few DBC chains that stray from the interface have stretched conformations. These observations are consistent with the idea that the added homopolymer effectively eliminates the packing frustration that DBC chains would experience to fill in the bicontinuous nodal centers.

In this work, we used as-nucleated morphologies spontaneously formed upon quenching it from a disordered system. For the case of $(\phi = 0.300, \alpha = 0.667)$, the G phase thus formed had a defect in the node, and we found its free energy to be higher than the defect-free morphology generated via a SCFT-based external field. In the literature, thermodynamic integration has been successfully used to probe the relative stability of defects in a lamellar phase[82]. Similarly, our work could be extended to explore the free-energy and morphological changes associated

with the annealing of defects in bicontinuous phases. This is especially important in the context of understanding the nucleation of these phases and the transitions between them, which is also a topic of our future studies.

We have focused on conditions in the vicinity of the theoretically predicted triple point where the G, D, and P phases coexist. Only recently has the D phase been shown to be a stable morphology in blends of DBC and homopolymer[112] albeit for a different A-B ratio in the DBC and smaller α. Despite the initial report of a P[28] in a copolymer-ceramic hybrid material, a recent re-examination of those samples revealed that it is more consistent with a distorted G[116]. Further strategies to enlarge the stability window of the P are required other avenues such as adding nanoparticles and star polymers to this blend might prove productive and are the object of ongoing research.

4.5 Supplementary information

4.5.1 Calculation of average density for U_{ext}

The ordering field U_{ext} is defined on a cubic grid and the number of voxels in each dimension is the closest integer of the box length. Thus, each voxel is approximately a unit length in each direction. As indicated in the main text, we preferred to determine the geometry of the external field based on the morphologies spontaneously nucleated via MD. Accordingly, the geometry of the ordering field is based on averaging over 10 snapshots taken 10^4 dimensionless time units apart from an MD simulation of the target morphology formed at the conditions of interest. This averaging is done to smooth out the resolution of the morphology and to eliminate

the spurious effects of transient defects. To calculate the average spatial density distribution, one cannot directly calculate them from different snapshots because the interfaces are not only locally fluctuating but can also shift (translate) over the course of the simulation. Therefore, we need to translate each snapshot to a common position[98].

To calculate the magnitude of structure factor $S_\tau(\mathbf{q})$ of component τ of each individual snapshot, we use the equation:

$$S_\tau(\mathbf{q}) = \frac{\left(\sum_{\tau_j=\tau} \cos(\mathbf{q}\cdot\mathbf{r}_j)\right)^2 + \left(\sum_{\tau_j=\tau} \sin(\mathbf{q}\cdot\mathbf{r}_j)\right)^2}{N_\tau} \tag{4.11}$$

where $\mathbf{q}$ is the wave vector and $\mathbf{r}_j$ is the location of particle j of type τ and N_τ is the total number of beads of τ in the box. The phase θ_k is given by

$$\theta_k = \tan^{-1}\left(\frac{\sum_{\tau_j=\tau} \cos(\mathbf{q}_k\cdot\mathbf{r}_j)}{\sum_{\tau_j=\tau} \sin(\mathbf{q}_k\cdot\mathbf{r}_j)}\right) \tag{4.12}$$

The density (reduced by the average volume fraction of the minority domain) at the center of each voxel is given by

$$\rho^*(\mathbf{r}) = 1 + \sum_{k,|q_k|<2} \beta_k \sin\left(\mathbf{q}_k\cdot\mathbf{r} + \theta_k\right); \qquad \beta_k = \frac{2}{\rho^*_\tau}\sqrt{\frac{S_\tau(\mathbf{q})}{N}} \tag{4.13}$$

The cutoff in $\mathbf{q}_k$ is used to smear out the effect of individual beads. For a translation $\mathbf{r} \to \mathbf{r}' = \mathbf{r} + \Delta\mathbf{r}$, the new density profile is:

$$\rho'^*(\mathbf{r}) = \rho'^*(\mathbf{r}' - \Delta\mathbf{r}) \tag{4.14}$$

$$= 1 + \sum_{k,|q_k|<2} \beta_k \sin[\mathbf{q}_k\cdot(\mathbf{r}' - \Delta\mathbf{r}) + \theta_k] \tag{4.15}$$

$$= 1 + \sum_{k,|q_k|<2} \beta_k \sin[\mathbf{q}_k\cdot\mathbf{r}' + \{-\mathbf{q}_k\cdot\Delta\mathbf{r} + \theta_k\})] \tag{4.16}$$

$$= 1 + \sum_{k,|q_k|<2} \beta_k \sin(\mathbf{q}_k\cdot\mathbf{r}' + \theta'_k) \tag{4.17}$$

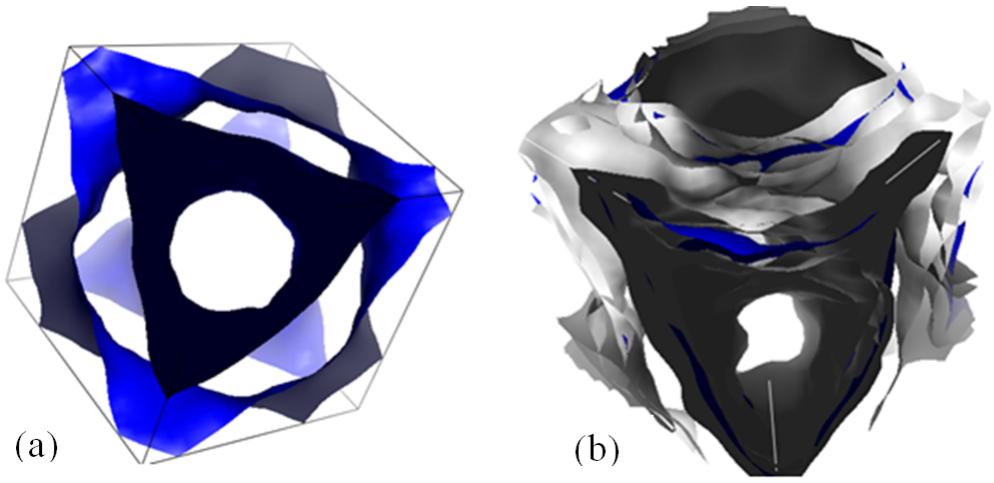

Figure 4.10: (a) Average D morphology, and (b) Ten morphologies translated such that they overlap. Note how each snapshot has fluctuating interfaces. Only the AB interfaces are shown.

Defining $\theta'_k \equiv -\mathbf{q}_k \cdot \Delta\mathbf{r} + \theta_k$,

$$\implies \Delta\theta = -\mathbf{q}_k \cdot \Delta\mathbf{r} \tag{4.18}$$

We see that a translation only produces a change in the phase factor[98]. In order to pick the translation $\Delta\mathbf{r}$ for each snapshot, we choose a basis set of three wave vectors that best describes the morphology. The set of basis vectors is obtained by trial-and-error of various combinations of linearly independent qks that contribute to the largest peak in the structure factor calculated from Equation 4.11. Taking any one of the snapshots as the reference snapshot, we readily have $\Delta\theta$, and we can then calculate $\Delta\mathbf{r}$ for each snapshot from Equation 4.18. Finally all the newly translated θ values are averaged over and we invert the average structure factor to calculate the average density profile. One example of calculating the average morphology for the diamond phase at $L_{box} = 20, \phi = 0.3, \alpha = 0.722$ is shown in Figure 4.10.

This averaging procedure did not work well for the G phase at one particular state point studied because the simulated morphologies contained a long-lived de-

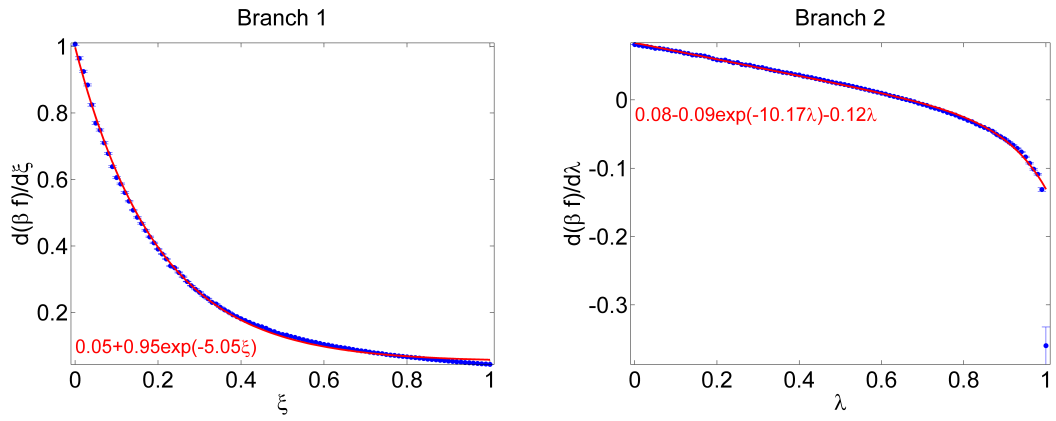

Figure 4.11: Integrand along each integration branch. The blue points are from a simulation of 100 equally spaced points for each branch. The red text shows the equation of the fitted curve drawn in red. The simulation conditions were $L_{box} = 10$, $\phi = 0.300$, $\alpha = 0.722$, and $P = 2$.

fect that persisted in the averaged G phase. For this case only (corresponding to $\phi = 0.300$ for $\alpha = 0.667$), we used a defect-free (ideal) morphology of the G phase obtained from SCFT.

4.5.2 Choice of quadrature method

In Figure 4.11, we plot the integrand for 100 equally-spaced points for both branches. We shall use this to compare the free energies calculated for fewer number of points using the methods described below.

1. **Trapezoid quadrature**: The trapezoid quadrature is a suitable first guess because it fits a zero curvature line between neighboring integration points. Although this systematically underestimates the free energy because the derivative of free energy is always negative, this error is small when using 100 points for evaluation of the integral, and we shall use this estimate to compare the accuracy of other techniques.

2. **Curve fitting**: The integral can be evaluated by fitting a curve (function) and evaluating its antiderivative. Polynomials usually provide a good fit; however higher order polynomials lead to oscillations near the edge of the range of integration (Runge's phenomenon). An erroneous or ill-sampled data point can also lead to fluctuations in the fitted polynomial, and thus the resulting answer[102]. Instead, we propose a non-polynomial fitting function. Based on the behavior of the comprehensive 100-point calculation, we propose an exponential (stretched) function of this type for the first branch:

$$g(\xi) = \alpha + \beta e^{-\gamma\xi} \tag{4.19}$$

The advantages of using Equation 4.19 are that: (i) its antiderivative is readily available $G(\xi) = \alpha\xi - \frac{\beta}{\gamma}e^{-\gamma\xi}$, and (ii) approximate values α and β are easily available. From Figure 4.11, and simulations for other box sizes (not shown), we observe $\gamma \approx 5 \sim \mathcal{O}(10)$ for $P = 2$. Thus, $\alpha + \beta = g(0)$ and $\beta \approx g(1)$, which are the end points in our simulation (whose values may be easily estimated by short simulations). For the second branch, the same function with respect to λ works with an additional linear term $\alpha_1\lambda$ for the increase in χN. The coefficients are different for both branches but can be estimated similarly.

P was varied from 1, 2, 5, and 1000 without detecting any discernible change in the estimate of free energy using the 100-point integration. The quality of the fit (and value of all coefficients) depended on the value of P imposed. A very high value of P causes the curve to linearize near $\xi = 1$, and subsequently branch 2 gets very sharp near $\lambda = 1$. $P = 2$ was chosen for subsequent simulations to sample according to g.

Furthermore, with the knowledge of the nature of the curve, we can leverage the use of non-uniform sampling[31] in ξ or λ, but at points such that G is

uniformly spaced. This is to obtain a slowly varying integrand which could require fewer evaluations to evaluate the integral accurately.

$$F(\lambda = 0 \to 1) = \int_0^1 \mathrm{d}\lambda \left\langle \frac{\partial U}{\partial \lambda} \right\rangle_\lambda = \int_0^1 \mathrm{d}\lambda \frac{\left\langle \frac{\partial U}{\partial \lambda} \right\rangle_\lambda}{g(\lambda)} g(\lambda) \tag{4.20}$$

$$= \int_{G(0)}^{G(1)} \frac{\left\langle \frac{\partial U}{\partial \lambda} \right\rangle_\lambda}{g(\lambda)} \mathrm{d}[G(\lambda)]; \quad \frac{dG(\lambda)}{d\lambda} = g(\lambda) \tag{4.21}$$

3. **Gaussian quadrature schemes**: We can also apply Gaussian quadrature schemes that approximate the integrals as a weighted sum of the integrands, with pre-specified weights and points at which to evaluate the integral. For the kind of integral we have (with unity as weighting function), we compare two options: the Lobatto scheme that specifically includes both end-points and the Legendre that uses neither end-points[86].

4.5.3 Comparison of methods

We compare the accuracy of these methods in Figure 4.12 for the overall process across different numbers of integration points in each branch. As expected, the trapezoid rule fares the worst, irrespective of whether the points are uniformly spaced in ξ/λ or $G(\xi/\lambda)$. The spacing sampled according to Equation 4.21 performs significantly better by fitting for the coefficients and integrating. Among the Gaussian quadrature methods, the Gauss-Legendre integration (not including end points) is accurate even for just 5 integrating points, while the Gauss-Lobatto (including end points) fares as poorly as conventional trapezoid integration. As explained below, the issue can be traced to the behavior of the integrand when the external field is completely switched off.

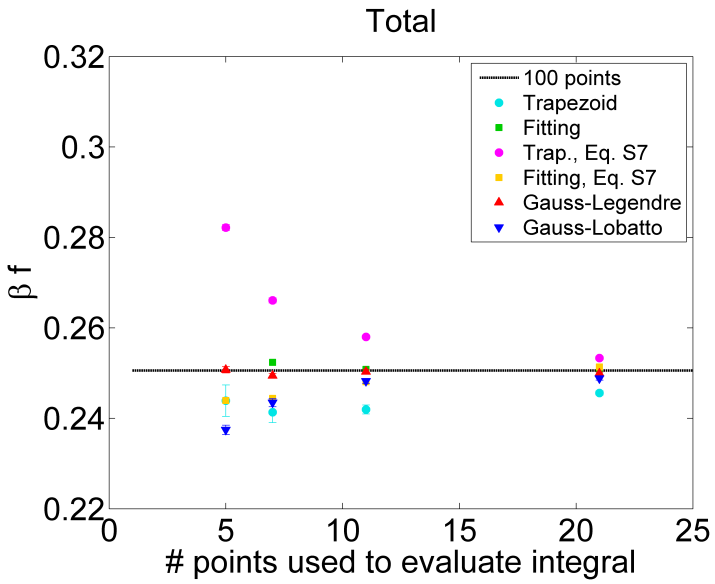

Figure 4.12: Free energy versus number of points used to evaluate the integral. The following methods were compared: (i) Using trapezoid integration of the data (blue dots), (ii) Fitting the data according to Equation S6 and analytically evaluating of the integral (green squares), (iii) Evaluating Eq. 4.21 using trapezoid (purple dots), (iv) Evaluating Eq. 4.21 by fitting a curve (orange squares), or Gauss-Legendre (red triangles) and Gauss-Lobatto (blue triangles)

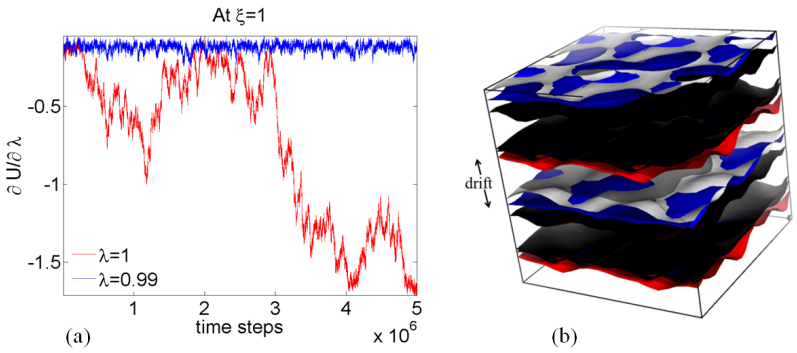

Figure 4.13: (a) Values of the integrand ($U_{int} - U_{ext}$) over the course of a simulation. (b) Comparison of the grid used to calculate the integrand (grey) with the actual morphology (blue for $\lambda = 0.99$, red for $\lambda = 1$) after 4 million MC cycles. The interface drift is apparent for $\lambda = 1$.

The Gauss-Lobatto quadrature includes the point $(\xi, \lambda) = (1, 1)$. At this value of λ the external field is completely removed during the simulation. This often leads to a drift in the morphology over the course of a long simulation because the center of the morphology is not constrained (recall that this drift necessitated shifting of snapshots to a common position before calculating the average isosurface, as mentioned earlier). However, our grid on which U_{ext} is defined was not designed to drift during the simulation, but is set at the beginning of the simulation. Thus, there is a significant contribution to the integrand $(U_{int} - U_{ext})$, not because the morphology itself deviates from the imposed one, but because it drifts across the periodic boundaries. This drift contributes erroneously to the free energy estimate, a problem that is worse for a small box size ($L_{box} = 10$). This issue can be worked around by imposing a small departure from zero in ξ and λ; namely of magnitude 0.01, to inhibit this artificial drift as demonstrated in Figure 4.13. Using this approach and for large box sizes (all of our morphologies are at least twice the model lamellar unit cell) we see only minor fluctuations. The extreme points used in Gauss-Legendre quadrature do not include $(\xi, \lambda) = (1,1)$, but rather $(\xi, \lambda) = (1, 0.99)$, so it is able to produce accurate results.

4.5.4 Analyzing network topologies

In order to investigate the evidence of packing frustration in our systems, we calculated topological markers d_i and d_c of voxels with majority of A-type beads. d_i is the distance of the voxel from the interface while d_c is the distance of the voxel from the center of the closest node. Here, we describe in detail the method used to calculate d_i and d_c. We demonstrate an example in Figure 4.14 for a 2-D cross-section of the P phase. The simulation box is divided into a cubic grid of

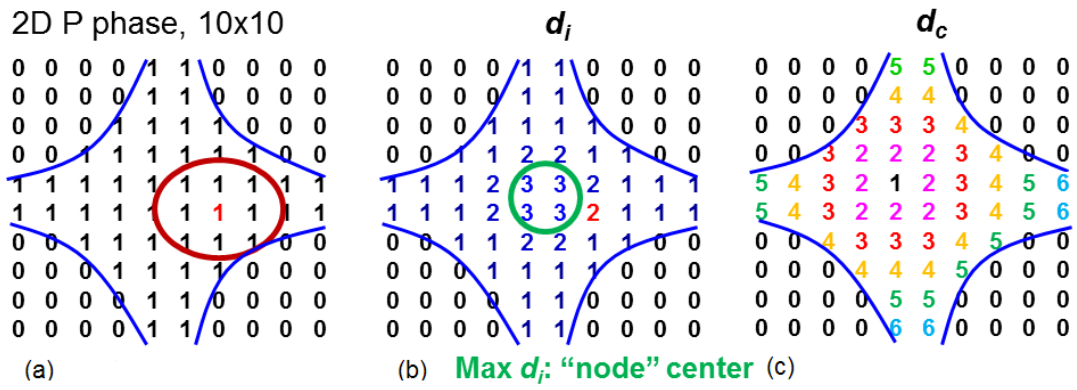

Figure 4.14: Illustrations for how the network structure is characterized, showing a 2-D projection of one network of the P phase (centered around a node) in a 10×10 grid. (a) Assigning voxels to clusters of type A and marking them as 1. The distance from the interface (d_i) of the voxel marked in red is found by drawing a circle that touches the interface. (b) Assigning d_i for each voxel and inferring the node center by the set of voxels with max d_is. (c) Calculating d_c for each voxel within the network.

voxels of approximate one distance unit in edge that would yield an integer number of voxels in the box. The local density for each voxel is calculated using Equation 4.13 and the voxel is labeled 1 if the normalized density of A-type beads is greater than 0.5 and 0 otherwise, as shown in Figure 4.14a. In order to identify the unique networks, we find clusters of voxels marked 1 with the criterion that if the nearest neighbor is also marked 1 it belongs to the same cluster. This is the region enclosed in blue. Within each cluster, we then calculate the distance of each voxel from the interface, or the edge of the cluster, d_i. We do so by calculating the radius of the largest sphere still enclosed within the cluster. For the voxel marked in red in Figure 4.14a, this value is 2. The corresponding di for each voxel is shown in Figure 4.14b. We then identify the set of voxels farthest from the interface (possessing highest values of d_i), enclosed in green in this case. The geometric center of the voxel is then denoted as the center of the node and in Figure 4.14c, we calculate the distance from the center of the node for each voxel (rounded to nearest whole number). Thus, each A-type voxel has two numbers associated with it, d_i and

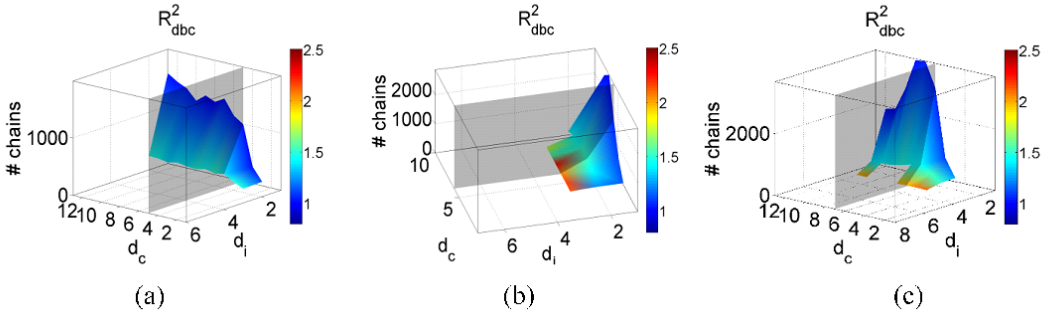

Figure 4.15: Population color maps showing the number of chains as a function of d_c and d_i and color coded based on $\langle R^2_{dbc} \rangle$. (a) G phase: $(\phi, \alpha, L_{box}) = (0.300, 0.722, 33)$, (b) D phase: $(\phi, \alpha, L_{box}) = (0.325, 0.722, 22)$, (c) P phase: $(\phi, \alpha, L_{box}) = (0.325, 0.722, 26)$.

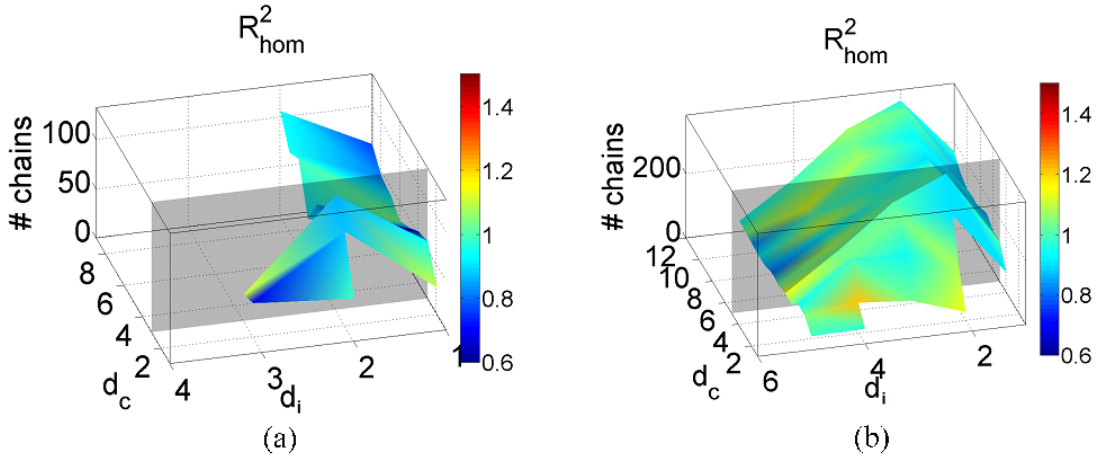

Figure 4.16: Population color maps for (a) stable G phase at $(\phi, \alpha, L_{box}) = (0.100, 0.722, 24)$, and (b) G phase coexisting with D at $(\phi, \alpha, L_{box}) = (0.300, 0.722, 33)$. Note that $\langle R^2_{hom} \rangle < 1$ and $r_{node} > r_{tube}$ in (a), while $\langle R^2_{hom} \rangle \approx 1$ and $r_{node} \approx r_{tube}$ in (b).

d_c. We then calculate the number of chains whose center of mass lies in the voxel possessing values of (d_i, d_c), and their associated square end-to-end distances.

The population color maps for each of the bicontinuous phases near the triple point is shown in Figure 4.15. The homopolymer color maps can be used to distinguish the geometric features of the phases as explained in the main text.

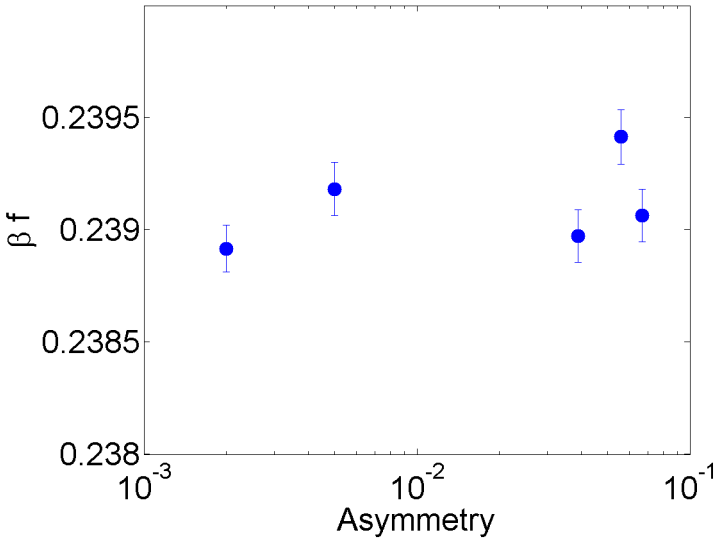

Figure 4.17: Dependence of free energy on network asymmetry for the P phase at conditions $(\phi, \alpha, L_{box}) = (0.325, 0.722, 25)$.

The DBC color maps, on the other hand (Figure 4.15), are similar for the G, D and P phases with the maximum number of DBC centers of mass lying at the interface ($d_i = 1$); and the value of $\langle R^2 \rangle$ is fairly independent of d_c along a fixed d_i. We finally plot in Figure 4.16 the homopolymer color maps for the G phases having significantly different composition (amount of homopolymer), one is the stable G phase with $\phi = 0.1$ and the other is the G phase with $\phi = 0.3$ that coexists with the D phase.

4.5.5 Asymmetry in networks of G and P phases

An important feature of the G and P microstructures spontaneously nucleated is that their networks may have asymmetric volumes as the two minority component networks do not intersect. Furthermore, the diffusive barrier is too high for exchange of either type of molecules between the two networks in the unit cell.

Therefore, once nucleated, the structures asymmetry is fairly fixed allowing only minor fluctuations. We define the degree of asymmetry as the difference in the number of voxels occupied by each network divided by the total number of voxels in the simulation box. The asymmetries we obtained ranged from 10^{-3} to 0.07. The different values occur by chance based on how the phases nucleated from a disordered system quenched to the target value of χN. It could be expected that asymmetry in the volumes of these networks would contribute to the free energy as well. To quantify this effect, we performed free energy calculations for P networks at $(\phi, \alpha, L_{box}) = (0.325, 0.722, 25)$ with varying asymmetry. Ten independent simulations were run for the given box size value and the average configurations from each of these simulations was evaluated for network asymmetry. We then selected networks with particular values of asymmetry and use them to create the geometry of the external fields needed for the calculation of free energies. As Figure 4.17 shows, these free energies have a spread of about 2×10^{-4}, which is slightly higher than the error bars in the individual simulations (1.2×10^{-4}). It appears that the free energy does not change significantly up to a network asymmetry of nearly 0.076, although this wasn't tested for every box size of every morphology because of the limited availability of computational resources. In any case, there might be a slight shift in the stability of the phases depending on the network asymmetry at which the free energies were calculated.

4.6 Acknowledgements

Partial support from the National Science Foundation award CMMI 1435852 is gratefully acknowledged. The authors are also grateful to computer cycles supplied by the Extreme Science and Engineering Discovery Environment (XSEDE) which

is supported by National Science Foundation grant number ACI-1053575. Early input from Dr. J. C. Araque is also acknowledged.

CHAPTER 5

OUTLOOK

The primary goal of this work was to stabilize bicontinuous phases using additives with a view to make them more accessible in experiments. We have identified routes to obtain a stable G phase using additives that target different aspects of the microstructure. Using uneven swelling of the microdomains using selective solvents in different volume ratios (Chapter 2), we were able to access the gyroid phase starting from a lamellar-forming DBC. Additionally, we calculated a four-dimensional phase diagram that provides a design roadmap to obtain specific domain sizes in the lamellar phase for nanolithographic applications. In chapter 3, using an interface modifier we modified the curvature of a cylinder-forming block copolymer to induce the formation of a G phase. In Chapter 4, we start with a G phase at overall volume fraction of A components $\phi_A = 1/3$ and find it to be stable over a large region of volume fractions up to $\phi_A = 0.53$. Thus we have established routes using suitable additives to obtaining the G phase starting from a DBC whose composition can lie between $f = 0.167$ to $f = 0.5$, instead of a very narrow region near $f = 1/3$ for a pure DBC.

These studies also show the improved tunability of morphologies of DBCs. We showed in Chapter 2 how solvents can be used to decrease the width of lamellar domains. This is possible even for bicontinuous phases. The unit cell sizes vary from $L_{box} = 19$ to $L_{box} = 33$ for the G phase which is about 4.6 to 8 times the root mean squared end-to-end distance of the 18-mer polymer used in our simulations. Adding a cosurfactant decreases the domain sizes by decreasing surface tension, while adding a long homopolymer that acts as a dry brush, significantly increasing the domain sizes. Figure 5.1 shows that upon adding the appropriate additive,

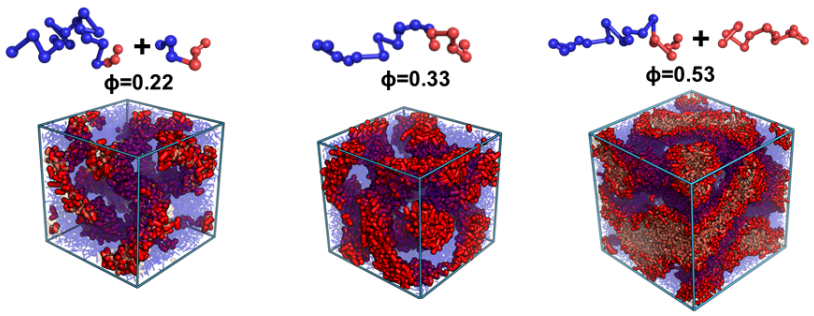

Figure 5.1: Tuning size of G domains using additives. Adding a cosurfactant decreases the domain size relative to a pure DBC, while adding a homopolymer increases the domain size relative to pure DBC. In this figure, ϕ refers to the total volume fraction of all A-type beads.

we not only tune the unit cell sizes, but can also obtain a much wider range of volume fractions of the A-domains of the G phase. Thus, by selectively choosing the right additives bicontinuous phases are accessible from three different starting morphologies as well as widely tunable in terms of the domain sizes.

With respect to simulation methodology, we used both SCFT and MD were used to study the phase diagrams. In Chapter 2 (two solvents), SCFT was the only applicable technique because of large disparity in sizes of the solvent and polymer. Thus, below $\alpha = 0.05$ we cannot use particle-based simulations directly. We found a region of phase space ($\chi N = 30, \alpha = 0.01$) that showed good agreement with experiments and predicts that the BCC micelles found in experiment was a kinetically trapped state. In Chapter 3 (cosurfactant straddling the surface), SCFT was used to quickly summarize the phase diagram to identify regions of interest for performing detailed MD simulations. Using MD, it was difficult to discern the stable phase because both C and G occurred at the same macroscopic conditions (ϕ_A, α) but at different simulation box sizes. An incommensurate simulation box size also frustrates the bicontinuous morphologies and this can artificially induce the appearance of kinetically trapped phases. Thus, free energy techniques are

required to identify the stable phase, as well as the optimum simulation box size. Methods used primarily in Chapter 2 using chemical potential calculations were within error bars of each other. A more serious issue with the technique is that it does not allow a change in number of unit cells which introduces an additional term in the free energy calculation[110]. Thus, we identified a need to develop a newer technique to calculate free energies directly (particularly for bicontinuous phases), that would both find the optimum box size for each morphology and with smaller error bars.

In Chapter 4 (homopolymer additive), we developed and used a modified version of thermodynamic integration that constructs a reversible path from the morphology of interest and a disordered structure. Free energies were calculated with a resolution of $10^{-4}k_BT$ per monomer which is suitable to resolve the stability of phases near the triple point, and to pinpoint the optimum box size for each phase. Furthermore, this technique may be used to calculate free energies of specific defects or topological features. In agreement with previously predicted SCFT calculations[67], we found D-G and D-P regions with comparable free energies close to the triple point, while deviating from SCFT At lower α, thus elucidating the effects of fluctuations.

The next direction of research lies in extending current free energy calculations to include calculation of free energy barriers that occur during the nucleation of these phases. Studying phase transformations (order-order transitions) between phases with disparate unit cell sizes is an open problem, and therefore we can only study specific transitions where the unit cell sizes match. In Chapter 4, we have shown how the C and D phases can switch back and forth in a single MD simulation at $L_{box} = 20$. Using more sophisticated methods[113, 49], we can

look at mechanisms of the growth of these domains and splitting of a disordered structure into two distinct networks, or between two ordered phases that occur at a single box size. From Chapter 3, we can also look at C-G transition because they occur at box sizes close to each other. Other than a rapid temperature quench (such as the one we studied in Chapter 4), rapid expansion can be another route to obtain metastable phases, which could subsequently trapped in those states. This was demonstrated in simulation[81] for the transition from BCC micelles to a more complex I-WP phase (Each node interconnects 8 tubes). These studies are experimentally relevant and can help design better routes to obtaining the morphology of interest.

The search for newer and more complex phases is not over. We showed a woodpile phase occurring in simulation in Chapter 3. This points to a region of stability nearby, or a larger region of metastability in the vicinity of parameters studied. Detailed SCFT calculations for the two-layer woodpile phase could be a future direction. Entropically engineered materials[26], rather than enthalpy alone, has been an emerging field of research. Additives bring in translational and mixing entropy while polymer-based additives essentially provide a large degree of conformational entropy (as extensively studied in this work). By leveraging the added entropy of homopolymers, an entire repository of lamellar bend angles was successfully obtained for incorporation in nanolithographic applications. Use of tethered nanoparticles[50] also produces a similar phase behavior as block copolymers. Techniques exploiting other forms of entropy (such as rotational entropy, new chain architectures) and more numbers of blocks[4] can yield newer kinds of phases. For instance, introducing chirality in one of the blocks has been shown to produce new phases (helical H*[44]) and even phase transitions ($H^* \rightarrow G$[10]) in experiment. This also opens the door to developing coarse-grained models for

chiral molecules. Branched chain architecture produces newer arrangements of micelles (A15)[35]. Changing the stiffness of the individual blocks (rod-coil DBCs, or liquid crystalline molecules with a side chain[117]) also affects the phase behavior. Currently, we are working on obtaining the G phase for a bolaamphiphile[61] containing a branched side chain.

BIBLIOGRAPHY

[1] Paschalis Alexandridis, Ulf Olsson, and Björn Lindman. A record nine different phases (four cubic, two hexagonal, and one lamellar lyotropic liquid crystalline ad two micellar solutions) in a ternary system of an amphiphilic block copolymer and selective solvents (water and oil). Langmuir, 14:2627–2638, 1998.

[2] R J Allen, D Frenkel, and P R ten Wolde. Simulating rare events in equilibrium or nonequilibrium stochastic systems. J. Chem. Phys., 124(2006):24102, 2006.

[3] Allan F. M. Barton. Handbook of polymer-liquid interaction parameters and solubility parameters. Boca Raton: CRC Press, 1990.

[4] F. S. Bates, M. a. Hillmyer, T. P. Lodge, C. M. Bates, K. T. Delaney, and G. H. Fredrickson. Multiblock Polymers: Panacea or Pandora's Box? Science, 336(6080):434–440, 2012.

[5] Charles H. Bennett. Efficient estimation of free energy differences from monte carlo data. Journal of Computational Physics, 22:245–268, 1976.

[6] Joan K. Bosworth, Marvin Y. Paik, Ricardo Ruiz, Evan L. Schwartz, Jenny Q. Huang, Albert W. Ko, Detlef-M. Smilgies, Charles T. Black, and Christopher K. Ober. Control of self-assembly of lithographically patternable block copolymer films. ACS Nano, 2:1396–1402, 2008.

[7] J. Brandrup, E. H. Immergrut, and E. A. Grulke. Polymer Handbook. John Wiley and Sons, 4 edition, 1999.

[8] Yung Chang, Hsiao-Yang Hsueh, Wen-Chang Chen, and Ching-I Huang. Effects of neutrak solvent addition on the body-centered cubic spheres of block copolymers. Polymer, 46:3942–3951, 2005.

[9] Michelle Chavis. in preparation. PhD thesis, Cornell University, 2014. Chapter 5.

[10] Chun Ku Chen, Han Yu Hsueh, Yeo Wan Chiang, Rong Ming Ho, Satoshi Akasaka, and Hirokazu Hasegawa. Single helix to double gyroid in chiral block copolymers. Macromolecules, 43(20):8637–8644, 2010.

[11] F. Chen, Y. Kondo, and T. Hashimoto. Control of nanostructure in mixtures of block copolymers: Curvature control via cosurfactant effects. Macromolecules, 40:3714–3723, 2007.

[12] Joy Y. Cheng, Caroline a. Ross, Henry I. Smith, and Edwin L. Thomas. Templated self-assembly of block copolymers: Top-down helps bottom-up. Advanced Materials, 18(19):2505–2521, 2006.

[13] Christophe Chipot and Andrew Pohorille, editors. Free Energy Calculations: Theory and Applications in Chemistry and Biology. Springer Series in Chemical Physics, 2007.

[14] F Court and T Hashimoto. Morphological Studies of Binary Mixtures of Block Copolymers. 1. Cosurfactant Effects and Composition Dependence of Morphology. Macromolecules, 34(8):2536–2545, 2001.

[15] F Court, D Yamaguchi, and T Hashimoto. Morphological and scattering studies of binary mixtures of block copolymers: Cosurfactant effects observed in the parameter space of temperature, blend composition, and molecular weight ratio. Macromolecules, 41(13):4828–4837, 2008.

[16] Francois Court and Takeshi Hashimoto. Morphological studies of binary mixtures of block copolymers. 1. cosurfactant effects and composition dependence of morphology. Macromolecules, 34:2536–2545, 2001.

[17] Edward J. W. Crossland, Marleen Kamperman, Mihaela Nedelcu, Caterina Ducati, Ulrich Wiesner, Detlef-M. Smilgies, Gilman E. S. Toombes, Marc A. Hillmyer, Sabine Ludwigs, Ulrich Steiner, and Henry J. Snaith. A bicontinuous double gyroid hybrid solar cell. Nano Letters, 9:2807–2812, 2009.

[18] Julia D. Cushen, Lei Wan, Gunja Pandav, Indranil Mitra, Gila E. Stein, Venkat Ganesan, Ricardo Ruiz, C. Grant Willson, and Christopher J. Ellison, 2014.

[19] Giuseppe D'Adamo and Carlo Pierloni. Crystalline free energies of micelles of diblock copolymer solutions. The Journal of Chemical Physics, 133:204902, 2010.

[20] S.B. Darling. Directing the self-assembly of block copolymers. Progress in Polymer Science, 32(10):1152–1204, 2007.

[21] Seth B. Darling. Block copolymers for photovoltaics. Energy & Environmetal Science, 2:1266–1273, 2009.

[22] Drew A. Davidock, Marc A. Hillmyer, and Timothy P. Lodge. Persistence of the gyroid morphology at strong segregation in diblock copolymers. Macromolecules, 36:4682–4685, 2003.

[23] Tomonari Dotera. Tricontinuous cubic structures in abc/a/c copolymer and homopolymer blends. Physical Review Letters, 89:205502, 2002.

[24] Thomas H. Epps III, Eric W. Cochran, Travis S. Bailey, Ryan S. Waletzko, Cordell M. Hardy, and Frank S. Bates. Ordered network phases in linear poly(isoprene-b-styrene-b-ethylene) triblock copolymers. Macromolecules, 37:8325–8341, 2004.

[25] Carlos J. Garcia-Cervera Eric W. Cochran and Glenn H. Fredrickson. Stability of the gyroid phase in diblock copolymers at strong segregation. Macromolecules, 39:2449–2451, 2006.

[26] Fernando A. Escobedo. Engineering entropy in soft matter: the bad, the ugly and the good. Soft Matter, 10(42):8388–8400, 2014.

[27] Fernando A. Escobedo and Juan J. de Pablo. Monte carlo simulation of the chemical potential of polymers in an expanded ensemble. The Journal of chemical Physics, 103:2703–2710, 1995.

[28] Adam C Finnefrock, Ralph Ulrich, Gilman E S Toombes, Sol M Gruner, Ulrich Wiesner, Clark Hall, and New York. The Plumber s Nightmare : 1 A New Morphology in Block Copolymer - Ceramic Nanocomposites and Mesoporous Aluminosilicates. The Journal of American Chemical Society, 125(43):13084–13093, 2003.

[29] National Institute for Materials Science database. http://polymer.nims.go.jp/index_en.html.

[30] S F"orster, A Timmann, M Konrad, C Schellbach, A Meyer, S S Funari, P Mulvaney, and R Knott. Scattering Curves of Ordered Mesoscopic Materials. Journal of Physical Chemistry B, 109(4):1347–1360, 2005.

[31] Daan Frenkel and Berend Smit. Understanding Molecular Simulations: From Algorithms to Applications. Academic, San Diego, CA, 2 edition, 2002.

[32] A. Gabashvili, Dana D. Medina, A. Gedanken, and Y. Mastai. Templating mesoporous silica with chiral block copolymers and its application for enatioselective separation. The Journal of Physical Chemistry B, 111:11105–11110, 2007.

[33] Marina I. Giannotti and G. Julius Vansco. ChemPhysChem, 8:2290–2307, 2007.

[34] Kevin W. Gotrik, Adam F. Hannon, Jeong Gon Son, Brent Keller, Alfredo Alexander-Katz, and Caroline A. Ross. Morphology control in block copolymer films using mixed solvent vapors. ACS Nano, 6:8052–8059, 2012.

[35] G.M. Grason and R.D. Kamien. Self-consistent field theory of multiply branched block copolymer melts. Physical Review E, 71(5):051801, 2005.

[36] Gregory M. Grason. The packing of soft materials: Molecular asymmetry, geometric frustration and optimal lattices in block copolymer melts. Physics Reports, 433(1):1–64, 2006.

[37] Robert D. Groot, Timothy J. Madden, and Dominic J. Tildesley. On the role of hydrodynamic interactions in block copolymer microphase separation. The Journal of chemical physics, 110:9739–9749, 1999.

[38] Robert D. Groot and Patrick B. Warren. Dissipative particle dynamics: Bridging the gap between atomistic and mesoscopic simulation. The Journal of chemical physics, 107:4423–4435, 1997.

[39] D A Hajduk, P E Harper, S M Gruner, C C Honeker, G Kim, E L Thomas, and L J Fetters. The gyroid- a new equilibrium morphology in weakly segregated diblock copolymers. Macromolecules, 27(15):4063–4075, 1994.

[40] I. W. Hamley. Ordering in thin films of block copolymers: Fundamentals to potential applications. Progress in Polymer Science (Oxford), 34(11):1161–1210, 2009.

[41] Kenneth J. Hanley and Timothy P. Lodge. Phase behavior of a block copolymer in solvents of varying selectivity. Macromolecules, 33, 2000.

[42] Charles M. Hansen. Hansen solubility parameters: a user's handbook. Boca Raton: CRC Press, 2 edition, 2007.

[43] Takeji Hashimoto, Mitsuhiro Shibayama, and Hiromichi Kawai. Ordered

structure in block polymer solutions. 4. scaling rules on size of fluctuations with block copolymer weight, concentration, and temperature in segregation and homogeneous regimes. Macromolecules, 16:1093–1101, 1983.

[44] Rong Ming Ho, Yeo Wan Chiang, Chun Ku Chen, Hsin Wei Wang, Hirokazu Hasegawa, Satoshi Akasaka, Edwin L. Thomas, Christian Burger, and Benjamin S. Hsiao. Block copolymers with a twist. Journal of the American Chemical Society, 131(17):18533–18542, 2009.

[45] P. J. Hoogerbrugge and J. M. V. A. Koelman. Simulating microscopic hydrodynamic phenomena with dissipative particle dynamics. Europhysics Letters, 19:155–160, 1992.

[46] Han-Yu Hsueh, Yi-Chun Ling, Hsiao-Fang Wang, Lung-Yu Chiang Chen, Yu-Chueh Hung, Edwin L. Thomas, and Rong-Ming Ho. Shifting networks to achieve subgroup symmetry properties. Advanced Materials, 26:3225–3229, 2014.

[47] Ching-I Huang and Yu-Chieh Hsu. Effects of solvent immiscibility on the phase behavior and microstructural length scales of a diblock copolymer in the presence of two solvents. Phys. Rev. E: Stat., Nonlinear, Soft Matter Phys., 74:051802, 2006.

[48] Ching-I Huang and Timothy P. Lodge. Self-consistent calculations of block copolymer solution phase behavior. Macromolecules, 31:3556–3565, 1998.

[49] Su-Mi Hur, Vikram Thapar, Abelardo Ramírez-Hernández, Gurdaman Khaira, Tamar Segal-Peretz, Paulina A. Rincon-Delgadillo, Weihua Li, Marcus Müller, Paul F. Nealey, and Juan J. de Pablo. Molecular pathways for defect annihilation in directed self-assembly. Proceedings of the National Academy of Sciences, 112(46):201508225, 2015.

[50] Christopher R. Iacovella, Aaron S. Keys, Mark A. Horsch, and Sharon C. Glotzer. Icosahedral packing of polymer-tethered nanospheres and stabilization of the gyroid phase. Physical Review E, 75(4):040801, 2007.

[51] Haitao Jia, Haiying Huang, Tianbai He, and Yumei Gong. A theoretical study on the inverted phase formation in diblock copolymer solutions. The Journal of Chemical Physics, 137:224902, 2012.

[52] Francisco J.Martinez-Veracoechea and Fernando A.Escobedo. Lattice monte carlo simulations of the gyroid phase in monodisperse and bidisperse block copolymer systems. Macromolecules, 38:8522–8531, 2005.

[53] Francisco J.Martinez-Veracoechea and Fernando A.Escobedo. Simulation of the gyroid phase in off-lattice models of pure diblock copolymer melts. The Journal of chemical physics, 125:104907, 2006.

[54] Gyuha Jo, Hyungmin Ahn, and Moon Jeong Park. Simple route for tuning the morphology and conductivity of polymer electrolytes: One end functional group is enough. ACS Macro Letters, 2:990–995, 2013.

[55] Miguel Jorge, Nuno M. Garrido, Antonio J. Queimada, Ioannis G. Economou, and Eugenia A. Macedo. Effect of the integration method on the accuracy of free energy calculations using thermodynamic integration. Journal of Chemical Theory and Computation, 6:1018–1027, 2010.

[56] Myung Im Kim, Tsutomo Wakada, Satoshi Akasaka, Shotaro Nishitsuji, Kenji Saijo, Hirokazi Hasegawa, Kazuki Ito, and Mikihito Takenaka. Determination of Fddd phase boundary in polystyrene-block-polyisoprene diblock copolymer melts. Macromolecules, 42:5266–5271, 2009.

[57] John G. Kirkwood. Statistical mechanics of fluid mixtures. The Journal of Chemical Physics, 3:300–313, 1935.

[58] David A. Kofke and Peter T. Cummings. Quantitative comparison and optimization of methods for evaluating the chemical potential by molecular simulation. Molecular Physics, 92:973–996, 1997.

[59] Li Li, Piotr Szewczykowski, Lydia D. Clausen, Kristian M. Hansen, Gunnar E. Jonsson, and Sokol Ndoni. Ultrafiltration by gyroid nanoporous polymer membranes. Journal of Membrane Science, 384(1-2):126–135, 2011.

[60] P. M. Lipic, F. S. Bates, and M. W. Matsen. Non-equilibrium phase behavior of diblock copolymer melts and binary blends in the intermediate segregation regime. Journal of Polymer Science: Part B: Polymer Physics, 37:2229–2238, 1999.

[61] Feng Liu, Marko Prehm, Xiangbing Zeng, Carsten Tschierske, and Goran Ungar. Skeletal cubic, lamellar, and ribbon phases of bundled thermotropic bolapolyphiles. Journal of the American Chemical Society, 136(19):6846–6849, 2014.

[62] C. P. Lowe. An alternative approach to dissipative particle dynamics. Europhysics Letters, 47:145–151, 1999.

[63] A. P. Lyubartsev, A. A. Martsinovski, S. V. Shevkunov, and P. N. VorontsovVelyaminov. New approach to monte carlo calculation of the free energy: Method of expanded ensembles. The Journal of Chemical Physics, 96:1776–1783, 1992.

[64] Rina Maeda, Michelle Chavis, Nam-Ho You, and Christopher K. Ober. Top-down meets bottom-up: Block copolymers with photoreactive segments. Joural of Photopolymer Science and Technology, 25:17–20, 2012.

[65] F. J. Martinez-Veracoechea and Fernando A. Escobedo. Monte carlo study of the stabilization of complex bicontinuous phases in diblock copolymer systems. Macromolecules, 40:7354–7365, 2007.

[66] Francisco J. Martinez-Veracoechea and F. A. Escobedo. Bicontinuous phases in diblock copolymer/homopolymer blends: simulation and self-consistent field theory. Macromolecules, 42:1775–1784, 2009.

[67] Francisco J. Martinez-Veracoechea and Fernando A. Escobedo. The plumber's nightmare phase in diblock copolymer/homopolymer blends. a self-consistent field theory. Macromolecules, 42:9058–9062.

[68] J. Matoš, A. Živný, and J. Biroš. Thermodynamic mixing functions of the system tetrahydrofuran (1) methanol (2). Collection of Czechoslovak Chemical Communications, 37:3960–3964, 1972. also: http://www.ddbst.com/ddb.html.

[69] M W Matsen. Gyroid versus double-diamond in ABC triblock copolymer melts. Journal of Chemical Physics, 108(2):785–796, 1998.

[70] Mark W. Matsen. Cylinder $\leftrightarrow$ gyroid epitaxial transitions in complex polymeric liquids. Physical Review Letters, 80:4470–4473, 1998.

[71] Mark W. Matsen. Cylinder $\leftrightarrow$ sphere epitaxial transitions in block copolymer melts. The Journal of Chemical Physics, 114:8165–8173, 2001.

[72] Mark W. Matsen. The standard gaussian model for block copolymer melts. Journal of Physics: Condensed Matter, 14:R21=R47, 2002.

[73] Mark W. Matsen. New fast SCFT algorithm applied to binary diblock copolymer/homopolymer blends. Macromolecules, 36, 2003.

[74] Mark W. Matsen and Frank S. Bates. One-component approximation for binary diblock copolymer blends. Macromolecules, 28:7298–7300, 1995.

[75] Mark W. Matsen and Frank S. Bates. Origins of complex self-assembly in block copolymers. Macromolecules, 29:7641–7644, 1996.

[76] Mark W. Matsen and Michael Schick. Stable and unstable phases of diblock copolymer melt. Physical Review Letters, 72:2660–2663, 1994.

[77] Adam J. Meuler, Marc A. Hillmyer, and Frank S. Bates. Ordered network mesostructures in block copolymer materials. Macromolecules, 42:7221–7250, 2009.

[78] Bianca M Mladek, Patrick Charbonneau, Christos N Likos ad Daan Frenkel, and Gerhard Kahl. Multiple occupany crystals formed by purely repulsive soft particles. Journal of Physics: Condensed Matter, 20:494245.

[79] David Morse, Christopher Tyler, Amit Ranjan, Jian Qin, and Raghuram Thiagarajan. http://research.cems.umn.edu/morse/code/pscf/home.php. (revision 11).

[80] Marcus Muller and Kostas Ch. Daoulas. Calculating the free energy of self-assembled structures by thermodynamic integral. The Journal of Chemical Physics, 128:024903, 2008.

[81] Marcus Müller and De-Wen Sun. Directing the Self-Assembly of Block Copolymers into A Metastable Complex Network Phase via A Deep and Rapid Quench. Physical Review Letters, 111(26):267801, 2013.

[82] Umang Nagpal, Marcus Müller, Paul F. Nealey, and Juan J. De Pablo. Free energy of defects in ordered assemblies of block copolymer domains. ACS Macro Letters, 1(3):418–422, 2012.

[83] Umang Nagpal, Marcus Muller, Paul F. Nealey, and Juan J. dePablo. Free energy of defects in ordered assemblies of block copolymer domains. ACS Macro Letters, 1:418–422, 2012.

[84] J. R. Naughton and Mark W. Matsen. Limitations of the dilution approximation for concentrated block copolymer/solvent mixtures. Macromolecules, 35:5688–5696, 2002.

[85] Mihaela Nedelcu, Stefan Guldin, M. Christopher Orilall, Jinwoo Lee, Sven

Hüttner, Edward J. W. Crossland, Scott C. Warren, Caterina Ducati, Pete R. Laity, Dominik Eder, Ulrich Wiesner, Ullrich Steiner, and Henry J. Snaith. Monolithic route to efficient dye-sensitized solar cells employing diblock copolymers for mesoporous TiO2. Journal of Materials Chemistry, 20(7):1261, 2010.

[86] NIST Digital Library of Mathematical Functions.

[87] Poornima Padmanabhan, Michelle Chavis, Christopher Ober, and Fernando A. Escobedo. Phase behaviour of pmma-b-phema with solvents methanol and thf: modeling and comparison to the experiment. Soft Matter, 10:6172–6181, 2014.

[88] Poornima Padmanabhan, Francisco J. Martinez-Veracoechea, and Fernando A. Escobedo. A theoretical and simulation study of the self-assembly of a binary blend of diblock copolymers. The Journal of Chemical Physics, 136:234905, 2012.

[89] Marvin Y. Paik, Joan K. Bosworth, Detlef-M. Smilges, Evan L. Schwartz, Xavier Andre, and Christopher K. Ober. Reversible morphology control in block copolymer films via solvet vapor processing: An in situ GISAXS study, 2010.

[90] Miri Park, Christopher Harrison, Paul M. Chaikin, Richard A. Register, and Douglas H. Adamson. Block copolymer lithography: Periodic arrays of $\sim 10^{11}$ holes in 1 square centimeter. Science, 276:1401–1404, 2007.

[91] Amit Ranjan, Jian Qin, and David C. Morse. Linear response and stability of ordered phases of block copolymer melts. Macromolecules, 41:942–954, 2008.

[92] Shakila B. Rizwan, Ben J. Boyd, Thomas Rades, and Sarah Hook. Bicontinuous cubic liquid crystals as sustained delivery systems for peptides and proteins. Expert Opinions in Drug Delivery, 7:1133–1144, 2010.

[93] Michael Rubinstein and Ralph H. Colby. Polymer physics. Oxford University Press, Oxford, New York, 4 edition, 2003.

[94] R. Ruiz, H. Kang, F. A. Detcheverry, E. Dobisz, D. S. Kercher, T. R. Albrecht, J. J. de Pablo, and P. F. Nealey. Density Multiplication and Improved Lithography by Directed Block Copolymer Assembly. Science, 321(5891):936–939, 2008.

[95] Shinichi Sakurai, Hiroshie Irie, Hideo Umeda, and Shunji Nomura. Gyroid structures and morphological control in binary blends of polystyrene-*block*-polyisoprene diblock copolymers. Macromolecules, 31:336–343, 1998.

[96] Vinodkumar Saranathan, Chinedum O. Osuji, Simon G. J. Mochrie, Heeso Noh, Suresh Narayanan, Alec Sandy, Eric R. Dufresne, and Richard O. Prum. Structure, function, and self-assembly of single network gyroid ($i4_132$) photonic crystals in butterfly wing scales. Proceedings of the National Academy of Sciences of the United States of America, 107:11676–11681, 2010.

[97] a J Schultz, C K Hall, and J Genzer. Box length search algorithm for molecular simulation of systems containing periodic structures. The Journal of chemical physics, 120(4):2049–2055, 2004.

[98] Andrew J. Schultz. Modeling and Computer Simulation of Copolymer/Nanoparticle Composites. PhD thesis, North Carolina State University, 2003.

[99] Andrew J. Schultz, Carol K. Hall, and Jan Genzer. Obtaining concentration profiles from computer simulation structure factors. Macromolecules, 40:2629–2632, 2007.

[100] L E Scriven. Equilibrium bicontinuous structure. Nature, 263(5573):123–125, 1976.

[101] An-Chang Shi and Jaan Noolandi. Effects of short diblocks at interfaces of strongly segregated long diblocks. Macromolecules, 27:2936–2944, 1994.

[102] Conrad Shyu and F. Marty Ytreberg. Reducing the bias and uncertainty of free energy estimates by using regression to fit thermodynamic integration data. Journal of Computational Chemistry, 30:2297–2304, 2009.

[103] Christophe Sinturel, Marylène Vayer, Michael Morris, and Marc A. Hillmyer. Solvent vapor annealing of block polymer thin films, 2013.

[104] E. J. Smith, T. Bryk, and A. D. J. Haymet. Free energy of solvation of simple ions: Molecular-dynamics study of solvation of cl and na+ in the ice/water interface. The Journal of Chemical Physics, 123:034706, 2005.

[105] Richard J. Spontak, Jennifer C. Fung, Michael B. Braunfeld, John W. Sedat, David A. Agard, Lisaleigh Kane, Steven D. Smith, Michael M. Satkowski, Arman Ashraf, Damian A. Hajduk, and Sol M. Gruner. Phase behavior

of ordered diblock copolymer blends: Effect of compositional heterogeneity. Macromolecules, 29:4494–4507, 1996.

[106] M. P. Stoykovich, H. Kang, K. Ch. Daoulas, G. Liu, Ch. Liu, J. J. De Pablo, M. Müller, and P. F. Nealey. Directed Self-Assembly of Block Copolymers for Nanolithography : Essential Integrated Circuit Geometries. Acsnano, 1(3):168–175, 2007.

[107] Mark P Stoykovich, Marcus Müller, Sang Ouk Kim, Harun H Solak, Erik W Edwards, Juan J de Pablo, and Paul F Nealey. Directed assembly of block copolymer blends into nonregular device-oriented structures. Science (New York, N.Y.), 308(5727):1442–1446, 2005.

[108] Pelle Strom and David M. Anderson. The cubic phase region in the system didodecyldimethylammonium bromide-water-styrene. Langmuir, 8(2):691–709, 1992.

[109] Tongchuan Suo, Dadong Yan, Shuang Yang, and An-Chang Shi. A theoretical study of phase behaviors for diblock copolymers in selective solvents. Macromolecules, 42:6791–6798, 2009.

[110] Wiliam C. Swope and Hans C. Andersen. Thermodynamics, statistical thermodynamics, and computer simlation of crystals with vacancies and interstitials. Physical Review A, 46:4539–4548, 1992.

[111] William C. Swope and Hans C. Andersen. Thermodynamics, statistical thermodynamics, and computer simulation of crystals with vacancies and interstitials. Physical Review A, 46:4539–4546, 1992.

[112] Hideaki Takagi, Katsuhiro Yamamoto, and Shigeru Okamoto. Ordered-bicontinuous-double-diamond structure in block copolymer/homopolymer blends. EPL (Europhysics Letters), 110(4):48003, 2015.

[113] Vikram Thapar and Fernando A. Escobedo. Localized Orientational Order Chaperones the Nucleation of Rotator Phases in Hard Polyhedral Particles. Physical Review Letters, 112(4):048301, 2014.

[114] Edwin L. Thomas, David B. Alward, David J. Kinning, David C. Martin, Dale L. Handlin, and Lewis J. Fetters. Ordered bicontinuous double-diamond structure of star block copolymers: a new equilibrium microdomain morphology. Macromolecules, 19(8):2197–2202, 1986.

[115] G. E. S. Toombes, S. M. Gruner, S. Mahajan, A. Jain, P. Du, M. Kamperman, U. Wiesner, M. Weyland, and D. A. Muller. Self-assembly of four-layer woodpile structure from zigzag abc copolymer/aluminosilicate concertinas. Macromolecules, 41:852–859, 2008.

[116] Gilman E S Toombes, Adam C. Finnefrock, Mark W. Tate, Ralph Ulrich, Ulrich Wiesner, and Sol M. Gruner. A re-evaluation of the morphology of a bicontinuous block copolymer-ceramic material. Macromolecules, 40(25):8974–8982, 2007.

[117] Carsten Tschierske. Liquid crystal engineering new complex mesophase structures and their relations to polymer morphologies, nanoscale patterning and crystal engineering. Chemical Society Reviews, 36(12):1930, 2007.

[118] C A Tyler and D C Morse. Orthorhombic Fddd network in triblock and diblock copolymer melts. Physical Review Letters, 94(20):208302, 2005.

[119] Christopher A. Tyler and David C. Morse. Orthorhombic Fddd network in triblock and diblock copolymer melts. Physical Review Letters, 94:208302, 2005.

[120] Vikrant N. Urade, Ta Chen Wei, Michael P. Tate, Jonathan D. Kowalski, and Hugh W. Hillhouse. Nanofabrication of double-gyroid thin films. Chemistry of Materials, 19(4):768–777, 2007.

[121] Augustine M. Urbas, Martin Maldovan, Peter DeRege, and Edwin L. Thomas. Bicontinuous cubic block copolymer photonic crystals. Advanced Materials, 14(24):1850–1853, 2002.

[122] Dirk W. vanKrevelen. Properties of polymers: their correlation with chemical structure, their numerical estimation and prediction from additive group contributions. Elsevier, 3 edition, 1990.

[123] Di Wei, Maik R. J. Scherer, Chris Bower, Piers Andrew, Tapani Ryhnen, and Ullrich Steiner. A nanostructured electrochromic supercapacitor. Nano Letters, 12(4):1857–1862, 2012.

[124] Robert A. Wickham, An-Chang Shi, and Zhen-Gang Wang. Nucleation of stable cylinders from a metastable lamellar phase in a diblock copolymer melts. The Journal of Chemical Physics, 118:10293–10305, 2003.

[125] Nigel B. Wilding and Peter Sollich. A Monte Carlo method for chemical

potential determination in single and multiple occupancy crystals. EPL (Europhysics Letters), 101(1):10004, 2013.

[126] Andrew S. Zalusky, Roberto Olayo-Valles, Johanna H. Wolf, and Marc A. Hillmyer. Ordered nanoporous polymers from polystyrene-polylactide block copolymers. The Journal of American Chemical Society, 124:12761–12773, 2002.